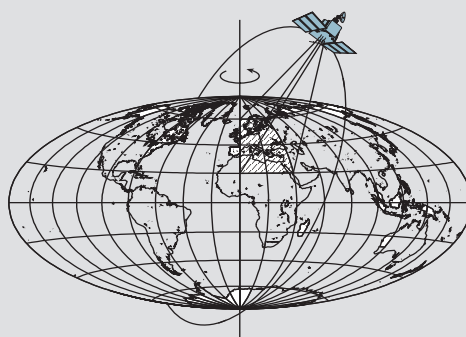


LOCAL AND REGIONAL GEOID DETERMINATION FROM VECTOR AIRBORNE GRAVIMETRY

by

Juan Gilberto Serpas



Report No. 468

Geodetic and GeoInformation Science
Department of Civil and Environmental Engineering and Geodetic Science
The Ohio State University
Columbus, Ohio 43210-1275

October 2003

LOCAL AND REGIONAL GEOID DETERMINATION
FROM VECTOR AIRBORNE GRAVIMETRY

By
Juan Gilberto Serpas

Report No. 468
Geodetic Science and Surveying
Department of Civil and Environmental Engineering and Geodetic Science
The Ohio State University
Columbus, Ohio 43210-1275

October, 2003

ABSTRACT

The local geoid in a test area in the Canadian Rocky Mountains is computed using airborne gravimetry data. The geoid is computed by the use of the vertical and horizontal components (VC and HC) of the gravity disturbance vector. In addition, an attempt to combine the three components by the use of least squares collocation is done. The technique of using crossovers to estimate for biases and trends in the gravity signals and the use of minimal control in the form of constraints in the crossover adjustment are studied. Moreover, the downward continuation as well as the direct and indirect effects due to removal and restoration of the masses are investigated. An expression for the effect of the masses applied directly to disturbing potential is provided.

Comparison of the predicted components of the gravity disturbing vector with control data indicates that the vertical component is better determined than the horizontal component. The estimated accuracy for the vertical components is on the order of 4 mGal, whereas for the horizontal components it is on the order of 8 to 12 mGal.

Both geoid estimates coming from the vertical and horizontal components of the gravity disturbance vector, computed using Hotine's and line integral, show the same level of accuracy when compared to the Canadian geoid. Relative geoid accuracies on the order of 3 to 7 cm for the VC geoid, and on the order of 4 to 12 cm for the HC geoid are achieved.

The VC geoid suffers from edge effects on the results, while the HC geoid is highly dependent on ground control. In order to alleviate the use of full ground control for the HC geoid, the computation of the geoid at two crossing tracks is explored.

Regarding the estimation of the geoid using least squares collocation to combine the three components of the gravity disturbance vector (3C-LSC), we observe differences in the range of 4 to 6 cm, without including edge effects, with respect to the Canadian geoid. Comparing the 3C-LSC results with those from the VC geoid using Hotine's integral, the 3C-LSC are comparable and improved for some lines, in terms of standard deviation. In general the result from the 3C-LSC are better than those from HC, by line integral. On the other hand, the use of only the vertical component by least squares collocation (VC-LSC) provides, in general, better results than those from 3C-LSC, and those from the VC and HC by the use of Hotine's and line integral. We could expect better results for the case of 3C-LSC if we are able to improve the quality of the measured horizontal components of the gravity disturbance vector.

The application of a wave correlation filter to both HC and VC component geoid is also explored, and promising results for the improvement of the accuracy of the combined geoid are observed.

PREFACE

This report was prepared by Juan Gilberto Serpas, a graduate student, Department of Civil and Environmental Engineering and Geodetic Science, under the supervision of Professor Christopher Jekeli.

This research was supported under a contract with the National Imagery and Mapping Agency (NIMA). Contract no. NMA202-98-1-1110.

This report was also submitted to the Graduate School of The Ohio State University as a thesis in partial fulfillment of the requirements for the degree Doctor of Philosophy.

ACKNOWLEDGMENTS

I wish to express my sincere gratitude to my advisor Professor Christopher Jekeli for his intellectual support and guidance throughout the development of this research.

I also want to acknowledge Professor C.K. Shum and Professor Burkhard Schaffrin for reviewing this study and being part of the evaluation committee.

Finally, I want to thank my family for their support and patience. Thank you Maricela, Gilberto Antonio, Juan Marcelo and José Joaquín. Without their support and love this work would have not been possible.

TABLE OF CONTENTS

	<u>PAGE</u>
Abstract.....	ii
Acknowledgments.....	iii
List of tables.....	vii
List of figures.....	ix

Chapters

1. INTRODUCTION	1
1.1 Geoid determination.....	1
1.2 Motivation and background	2
1.3 Chapter descriptions.....	4
 2. LOCAL AND REGIONAL GEOID DETERMINATION FROM AIRBORNE GRAVIMETRY DATA.....	 5
2.1 Introduction.....	5
2.2 The gravity disturbances	5
2.3 Hotine's integral for geoid determination.....	6
2.4 Relative geoid by profile integration	8
2.5 Least Squares Collocation (LSC).....	11
2.5.1 Basic formulas	11
2.5.2 The covariance matrices	12
2.5.2.1 Global covariance function	12
2.5.2.2 Local covariance function.....	13
2.6 Continuation of harmonic functions	15
2.6.1 The upward continuation	15
2.6.2 The downward continuation:	16
2.6.2.1 The gradient method	17
2.6.2.2 Iterative solution of Poisson's integral	17
2.6.2.3 Inversion of Poisson's integral.....	19
2.7 Reduction of observations for geoid determination.....	20
2.7.1 Traditional approach for geoid computation.....	20
2.7.2 Helmert's condensation method	22
2.7.3 Helmert's condensation method as a function of potential.....	23
 3. NUMERICAL ASPECTS OF GEOID COMPUTATION	 26
3.1 Introduction.....	26
3.2 The Fourier Transform and the FFT	26
3.3 Numerical implementation of Hotine's integral	29
3.4 Numerical implementation of the line integral for relative geoid determination ...	31
3.5 Numerical aspect for LSC.....	32
3.6 Numerical treatment for the downward continuation	36
3.6.1 The gradient method	36

3.6.2 The iterative solution of Poisson's integral	38
3.6.3 Test results	39
4. AIRBORNE GRAVIMETRY	41
4.1 Introduction.....	41
4.2 Gravity disturbance determination.....	41
4.2.1 Accelerations in the inertial frame.....	41
4.2.2 Improving the determination of the gravity vector by Kalman filter algorithm	43
4.3 Cross-over adjustment	46
4.4 Data processing to get the gravity vector.....	51
4.4.1 Area of study.....	51
4.4.2 The gravity disturbance vector.....	53
4.4.3 Experiments to remove large oscillation at the 180° turnings of the airplane..	56
4.4.3.1 Using the vertical component orientation error in the Kalman filter.....	57
4.4.3.2 Removal of oscillation prior to computation of Kalman filter residuals ..	59
4.4.4 Removal of the large oscillation at the 180° turnings of the airplane from the resulting Kalman residuals.....	61
4.5 Accuracy of the gravity disturbances with respect to control points	62
4.5.1 End-matching the residuals with NIMA control.....	64
4.5.2 Crossover adjustment of the gravity disturbance vector.....	71
4.5.2.1 Crossover adjustment for the vertical component of the gravity disturbance vector	72
4.5.2.2 Crossover adjustment for the horizontal components of the gravity disturbance vector	74
5. GEOID COMPUTATION/ESTIMATION	79
5.1 Introduction.....	79
5.2 The geoid from the down component of the gravity disturbance vector	79
5.2.1 Geoid estimation using NIMA full control for the vertical component.....	80
5.2.2 Helmert's condensation method applied to the vertical component of the gravity disturbance vector.....	84
5.2.3 Geoid estimation using adjusted crossovers for the vertical component.....	85
5.3 The geoid from the horizontal components of the gravity disturbance vector	87
5.3.1 The geoid from the horizontal components using total control	88
5.3.2 The geoid from the horizontal components using minimal control	90
5.4 The geoid from both the horizontal components and the downward component of the gravity disturbance vector	92
5.4.1 The geoid by the use of least squares collocation (LSC).....	92
5.4.2 The geoid by the use of a wave correlation filter (WCF)	95
6. CONCLUSION AND RECOMMENDATIONS	100
7. Bibliography	102

LIST OF TABLES

<u>Table</u>	<u>PAGE</u>
3.1: Statistics for the original and upward continued gravity disturbances	39
3.2: Statistics for the differences of the gradient and iterative solution for the downward continuation with respect to the original disturbing potential	39
4.1: Differences of north gravity disturbances versus NIMA control	63
4.2: Differences of east gravity disturbances versus NIMA control.....	63
4.3: Differences of vertical gravity disturbances versus NIMA control.....	64
4.4: Differences between end-matched north gravity disturbance and NIMA data	69
4.5: Differences between end-matched east gravity disturbance and NIMA data.....	69
4.6: Differences between end-matched down gravity disturbance and NIMA data	70
4.7: Differences of the original residuals and cross-over adjusted residuals with respect to NIMA control for the vertical component	72
4.8: Differences between simulated crossover-adjusted north gravity disturbances and NIMA control data.....	76
4.9: Differences between simulated crossover-adjusted east gravity disturbances and NIMA control data.....	76
5.1 Results for the VC height anomaly using Hotine's integral in the 22x11 grid of the differences with respect to Canadian geoid. EGM96 up to degree 360 is used.....	80
5.2: Results for the VC T/γ using Hotine's integral in the 22x11 grid of the differences with respect to Canadian geoid. EGM96 up to degree 360 is used. North- south edges have been removed	82
5.3 Results for the VC geoid using Hotine's integral in the 22x11 grid of the differences with respect to Canadian geoid. EGM96 up to degree 360 is used. Downward continuation and Helmert's condensation approach applied to the disturbing potential is included. North-south edges have been removed.	83
5.4: Results for the VC geoid using Hotine's integral in the 22x11 grid of the differences with respect to Canadian geoid. EGM96 up to degree 360 is used. Helmert's condensation approach applied to the gravity disturbances. Results with and without including the indirect effect. North-south edges have been removed.....	85
5.5: Results of the differences (30x11 grid) with respect to Canadian geoid for the full control and crossover VC. EGM96 up to degree 360 is used. Edge effects are still included.....	86

5.6: Results in the 30x11 grid of the differences with respect to Canadian geoid. For the VC with full control, and cross-over VC. EGM96 up to degree 360 is used. Edge effects have been removed.	86
5.7: Results in the 30x11 grid of the differences with respect to Canadian geoid. For the VC with full control, and cross-over VC. EGM96 up to degree 360 is used. Downward continuation and Helmert's condensation approach applied to the disturbing potential is included. Edge effects have been removed.	87
5.8: Differences of HC T/γ with the Canadian geoid at flight altitude. Lines are end-matched with the Canadian geoid.	88
5.9: Differences of HC T/γ with the Canadian geoid at flight altitude. Lines are end-matched with the Canadian geoid. North and south edges have been removed.	89
5.10: Differences of HC T/γ with the Canadian geoid at flight altitude. Lines were end-matched with the Canadian geoid.	91
5.11: Differences of HC T/γ with the Canadian geoid at flight altitude. Lines are end-matched with the Canadian geoid. North and south edges have been removed.	91
5.12: Differences of the LSC 3C T/γ with respect to the Canadian geoid, at flight height. North-south edges have been removed.	94
5.13: Differences of the LSC VC T/γ with respect to the Canadian geoid, at flight height. North-south edges have been removed.	95
5.14: Differences of the 3C WCF correlated T/γ with the Canadian geoid.	97
5.15: Differences of the 3C WCF T/γ with the Canadian geoid. North-south effects removed.	97
5.16: Accuracies of the 3C WCF, VC and HC geoids with respect to the Canadian geoid. North-south effects have been removed.	99

LIST OF FIGURES

<u>Figure</u>	<u>PAGE</u>
2.1: Flowchart for computing geoid undulations applying Hotine's integral.....	7
2.2: Flowchart for computing geoid undulations and application of profile integration .	10
3.1: Original and upward continued field (a), (b), and the downward continuation solution using the gradient method (c) and Poisson's iterative solution (d). Units of the contour lines are $[m^2/s^2]$	40
4.1: Schematic representation of cross-overs.....	47
4.2: Description of the area for the study.....	52
4.3: GPS and INS accelerations for Lines 1 to 3	54
4.4: Differences GPS –INS derived accelerations for lines 1 to 3.....	55
4.5: Residuals for lines 1 to 3 after applying Kalman filter.....	56
4.6: Comparison of the 30 sec smoothed chopped lines and 90 second smoother to the residuals with the original Kalman filter residuals.	60
4.7: Truncated lines excluding large oscillations.....	61
4.8: The components of the gravity vector	62
4.9: End-matched residuals vs Control (Line1)	65
4.10: End-matched residuals vs Control (Line 2)	66
4.11: Residuals vs Control (Line 3)	67
4.12: End-matched residuals vs Control (Line 12)	68
4.13: GPS trajectories for lines 1, 2 and 12	71
4.14: Comparison of down component residuals with respect to control by NIMA for the vertical component.....	73
4.15: Comparison of the crossover adjusted lines with respect to control by NIMA for the vertical component.....	73
4.16: Simulated crossing tracks for the north component of the gravity disturbance vector.....	75
4.17: Simulated crossing tracks for the east component of the gravity disturbance vector	75
4.18: Crossover adjusted lines by using simulated cross tracks versus NIMA control for the North component of the gravity disturbance vector.....	77
4.19: Crossover adjusted lines by using simulated cross tracks versus NIMA control for the East component of the gravity disturbance vector	77
5.1: Vertical component height anomaly versus Canadian geoid and their difference for the 22x11 grid.	81
5.2: Comparison of the VC height anomaly at flight altitude and final VC geoid (corrected by downward continuation and Helmert's condensation) with the Canadian geoid 2000.....	84
5.3: Differences in height anomaly from HC and Canadian geoid with (top) and without (bottom) north and south edges.....	90
5.4: a) Homeogram, and b) fitting curve to the isotropic homeogram	93
5.5: Comparison of the WCF 3C geoid to the Canadian geoid	98

CHAPTER 1

INTRODUCTION

1.1 Geoid determination

The determination of the geoid with high accuracy is a main goal among researchers in the geodetic community. With the generalized use of GPS the convenience of obtaining orthometric heights without doing leveling has been envisioned. Once the geoid is known, the orthometric height is computed easily, with good approximation, by the use of a straightforward relationship between the orthometric height and the ellipsoidal height. Ellipsoidal heights referred to a particular ellipsoid are easily obtained by the use of GPS.

The importance of the geoid is that it serves as a reference surface for orthometric heights. Most of the countries around the world have defined their own reference surface that in most of the cases does not coincide with the geoid. The sea level averaged over a period of time at one or more stations has been chosen as the origin for vertical control. Once this origin is established, geometric leveling circuits along with gravity measurements are carried out for the densification of national vertical networks, and orthometric heights referred to the local vertical datum are obtained. Due to the characteristics of the geometric leveling this is a slow and expensive process. But, if we can have access to the geoid, and with the use of GPS-derived ellipsoidal heights, we could compute orthometric heights in a relatively rapid and low cost manner.

One way to compute a local geoid is by the establishment and densification of gravimetric networks over a particular area. These networks help in providing high frequency information about the gravity field from which the geoid can be computed with fine resolution. The information about the long wavelength components of the geoid is obtained by the use of global geopotential models (e.g. EGM96, see Lemoine et al., 1998). In general, developed countries have already established dense gravimetric networks, and they are focusing on improving the quality of the geoid. Research about the identification and implementation of the most accurate methodologies for computing the geoid has to be carried out. On the other hand, there exist zones around the world where no data or scarcity of data hinders the computation of the geoid. The implementation of gravity networks in these areas is a very involved and expensive task in terms of time and money. In the last years airborne gravimetry has become a valuable tool to densify gravity networks in a fast and relatively economic fashion. This technique can be a viable approach in those countries that have poor or are lacking gravimetric networks. The accuracy of gravity measurements from airborne gravimetry has been improved during the last years, and nowadays it is being used successfully for geoid determination.

1.2 Motivation and background

Traditionally only the vertical component of the gravity disturbance vector has been used when computing the geoid with the use of airborne data (Forsberg et al, 2000; Bayoud and Sideris, 2001; Novák et al., 2003a). Alternatively, Jekeli and Kwon (2001) used the horizontal components reporting good accuracy in the determination of the geoid. As a consequence of the current trends used for geoid determination by airborne gravimetry, and as motivation for this study, we attempted to provide answers to the following questions: How is geoid determination improved if we use the whole information contained in the gravity vector? Can we expect better results in the determination of the geoid due to the fact that we have more information available? And, how should we apply the different reductions to our data in the case of combining observations?

Nowadays we can have access to the gravity disturbance vector by the use of airborne gravity. The resulting gravity disturbance vector contains biases and trends due to inherent errors in the instruments and the algorithms used for its determination. Therefore we need to incorporate some control in order for us to solve for these biases and trends. Since the observations are given along the track of the flight, the use of control at two end points of each line path will correct the slope and displacement of the line (Kwon, 2000). We have to recognize that this method is impractical in areas with poor gravimetric control. However, in the case of crossing lines a cross-over adjustment may be implemented to solve for such unknowns as relative biases and linear slopes to make the observations self-consistent. A minimal set of control points can then be used to solve for absolute biases and linear trends. The planning of the flight has to consider this, and should be aware of some problems arising at the 180° turns of the airplane, which introduce large oscillations in the collected data and may make them useless for future computations.

After correcting the gravity disturbance vector for possible biases and trends, and due to the fact that the observations are given at flight height we need to establish a scheme to reduce them to the geoid. When using airborne gravity data, the reduction of gravity quantities is slightly different from the case of using terrestrial gravity information. The differences are in the procedures used to handle the raw data coming from the sensors, and the computation of downward continuation to the terrain.

The downward continuation is known to be an ill-posed problem and errors in the data are amplified by this procedure. If we consider the fact that both horizontal components of the gravity disturbance are not as well determined as the down component, meaning that the error in the solution of the horizontal components is larger and a bigger concern, a study is necessary in order to determine the effect of the downward continuation in the results. The downward continuation by the use of Poisson's integral is studied.

Inversion and iterative methods for the downward continuation have been implemented and tested, and we find numerous studies for its solution, e.g. Wang (1988), Vaniček et al. (1996), Garcia (2000), Novák and Heck (2002). In general, both methods are based in solving Poisson's integral. The difference is in the approach used for its

solution. In general, when dealing with real noisy data, the downward continuation is an ill condition problem. For the case of the inversion method, a regularization parameter has to be introduced. The solution will strongly depend on the right choice of the regularization parameter, and for large amount of gridded data, the inversion of an even larger system is needed. In the iterative method no regularization parameter is needed explicitly, but sometimes the convergence of the solution is slow, depending on the characteristics of the surface where the original quantities are given (e.g. mountainous terrain). In this case, special attention has to be placed on the convergence criteria for the system. We need the process to provide an acceptable solution close to reality. Another way to compute the downward continuation consists in the use of the gradient method. This provides a direct solution where no regularization or iteration is necessary. One drawback of this method is that the data have to be given at a constant height. For the case of airborne data this method could be used as an alternative. Moreover, when using this method, it is customary to consider only first order terms for its solution while second and higher order terms are neglected.

When the observations or intermediate results are at terrain level we need them to be referred to the geoid. The geoid determination by the use of Stokes' integral from gravity anomalies obtained from airborne gravity data is described by Forsberg et al. (2000). Helmert's second method of condensation has been used to reduce the airborne gravity observations to determine the geoid in Canada by the use of Hotine's integral (Bayoud and Sideris, 2001). Recently, Novák et al. (2003a,b) describe the procedure to reduce airborne gravity disturbances focusing on improving the reductions from Helmert's condensation method. In this research different approaches for this method are investigated. Direct application of this method to the disturbing potential will be useful mainly when we compute the disturbing potential at flight height, but need it at the geoid.

Recently the relative geoid along a profile at flight height has been determined with reasonable accuracy by the use of the horizontal components of gravity by Jekeli and Kwon, (2001). The height anomaly was computed and the geoid was determined with the aid of Bouguer anomalies. In this example of a single profile the downward continuation of the data is problematic since data in areal extent are missing to appropriately model the characteristics of the disturbing potential. With information coming from several profiles over the area the downward continuation could be applied and one may expect, theoretically at least, better results.

This research deals with the identification and implementation of the most appropriate methodologies for the determination of local and regional geoids using airborne vector gravimetry. Helmert's condensation method is studied to reduce airborne gravity measurements. Its application directly to the disturbing potential is investigated. The horizontal and vertical components of the gravity disturbance vector are integrated for computing the geoid by the use of least squares collocation (LSC) or wave correlation filter (WCF). For the computations, data collected in an area of the Canadian Rocky Mountains are used.

1.3 Chapter descriptions

This study is organized as follows: First an introduction to the different methodologies to compute the geoid by the use of airborne gravity data is presented. Basic relationships that allow us to get the geoid by means of Hotine's integral, line integral, and least squares collocation are explained. Also a description of additional procedures for the manipulation and reduction of the data is given. Crossover adjustment, downward continuation, and Helmert's condensation method are explained. An equation to apply Helmert's condensation method directly to the disturbing potential is provided. This is an alternative solution to the traditional computation of the effect of the condensed topography and the condensed layer as well as of its direct and indirect effects on the computation of the geoid. In chapter 3, a description of the numerical methods and problems when dealing with discrete data are presented. The use of FFT techniques is explained. Some tests for assessing the results from downward continuation are also presented. In chapter 4, the basic approach to obtaining the gravity disturbance vector by the use of GPS-INS integration is explained. Data provided by the University of Calgary coming from a flight over the Canadian Rocky Mountains is processed to get the gravity disturbances. In chapter 5, the geoid is computed by the use of the vertical, horizontal and a combination of the three components of the gravity disturbance vector. A statistic assessment of the accuracies with respect to control information for the different methodologies is presented. An alternative solution to LSC based on the use of wave correlation filter (WCF) is also provided. In the final chapter conclusions and recommendations for the computation of an accurate geoid are presented.

CHAPTER 2

LOCAL AND REGIONAL GEOID DETERMINATION FROM AIRBORNE GRAVIMETRY DATA

2.1 Introduction

In this chapter a description of the different methods for local geoid determination from data collected from an airborne system are explained. The determination of the geoid by the use of the different components of the gravity vector is introduced. The application of Hotine's integral using the vertical components of the gravity disturbance vector, line integral methods by the use of the horizontal components, and least squares collocation (LSC) for a combination of the three components are described. The necessary reductions from flight height to the terrain and to the geoid and the related problems in doing so are also explained. Special attention is given to the application of Helmert's second method of condensation for removing and restoration of the visible topography. A new approach to compute this latter correction by applying it directly to the disturbing potential is developed and explained.

2.2 The gravity disturbances

Nowadays, airborne gravimetry allows us to have access to the three components of the gravity disturbance vector. The gravity disturbance vector is defined as the difference between the actual gravity and normal gravity vector, evaluated at the same location. For the gravity disturbance vector in P with respect to a particular frame we can write:

$$\delta \mathbf{g} = \mathbf{g}_P - \boldsymbol{\gamma}_P = \begin{pmatrix} g_1 - \gamma_1 \\ g_2 - \gamma_2 \\ g_3 - \gamma_3 \end{pmatrix}$$

where the sub-indices 1, 2 and 3 stand for the respective components in an arbitrary frame.

On the other hand, if we consider the magnitude of the gravity disturbance vector the following definition applies:

$$\delta g = |\mathbf{g}_P| - |\boldsymbol{\gamma}_P|, \text{ called simply gravity disturbance.}$$

The gravity disturbance vector contains valuable information that can be used for geoid determination. Different methodologies for estimating the geoid are explained in the following sections.

2.3 Hotine's integral for geoid determination

If we have gravity disturbances on a given ellipsoidal boundary, and we are interested in finding the disturbing potential, we are faced with a geodetic boundary value problem of second kind. This is, given the boundary and the normal derivative of T , we are interested in finding T . This situation is represented as:

$$\begin{aligned} \nabla^2 T &= 0 \quad \text{outside the boundary,} \\ \delta g &= g_p - \gamma_p \cong -\frac{\partial W}{\partial n} - \left(-\frac{\partial U}{\partial n} \right) = -\frac{\partial T}{\partial n} \quad \text{on the boundary,} \end{aligned} \quad (2.1)$$

where n denotes the ellipsoidal normal direction, or in spherical approximation:

$$\delta g = -\frac{\partial T}{\partial r} \quad \text{on the boundary.}$$

In the case of airborne gravimetry data, the boundary is giving by the flight level (say h_f).

The solution for the spherical geodetic boundary value problem as specified by equation (2.1) is given by Hotine's integral:

$$T(\theta, \lambda) = \frac{R + h_f}{4\pi} \iint_{\sigma} \delta g(\theta', \lambda') H(\psi) d\sigma \quad (2.2)$$

where $T(\theta, \lambda)$ is the disturbing potential at the point with coordinates (θ, λ) of flight height h_f , $\delta g(\theta', \lambda')$ are the gravity disturbances for each point on the level surface approximated by a sphere of radius $R+h_f$, $d\sigma$ is the element of surface on this boundary, and $H(\psi) = \sum_{n=0}^{\infty} \frac{2n+1}{n+1} P_n(\cos \psi)$ is the Hotine's function for the "opening angle" ψ that it is defined through $\cos \psi = \cos \theta \cos \theta' + \sin \theta \sin \theta' \cos(\lambda' - \lambda)$.

Hotine's function can be written in closed form as (Hotine, 1969, p.311):

$$H(\psi) = \operatorname{cosec}\left(\frac{1}{2}\psi\right) + \ln\left(1 + \operatorname{cosec}\left(\frac{1}{2}\psi\right)\right)$$

Notice that equation (2.2) includes the zero and first-degree harmonics for the disturbing potential. If we would like to consider the center of mass to be at the origin and also consider the mass of the geoid to be equal to the mass of the reference spheroid, we can modify Hotine's kernel as follows:

$$H'(\psi) = \sum_{n=2}^{\infty} \frac{2n+1}{n+1} P_n(\cos \psi) = \operatorname{cosec}\left(\frac{1}{2}\psi\right) + \ln\left(1 + \operatorname{cosec}\left(\frac{1}{2}\psi\right)\right) - 1 - \frac{3}{2}\cos \psi \quad (2.3)$$

since $P_0(\cos\psi)=1$, and $P_1(\cos\psi) = \cos\psi$.

Also, notice that the disturbing potential in equation (2.2) is given on a surface different than the geoid, and since we are interested in the disturbing potential at geoid level, we need to apply a series of reductions to the gravity disturbances before computing the disturbing potential. These reductions include the downward continuation of the gravity disturbances to the terrain, and the removal/restoration of the topography (direct effect). Now we apply Hotine's integral, at geoid level, to the reduced gravity disturbances, and then we correct them for the indirect effect. This procedure and the equations involved are explained in more detail in sections (2.7.1) and (2.7.2). An alternative is to compute the disturbing potential at flight altitude, as indicated by equation (2.2), downward continue it and correct for the effect of the topography. The latter correction can be done by either applying an orthometric correction (see equation (2.7)) or by the use of Helmert's condensation method (see section (2.7.3)). In Figure 2.1 we can observe a diagram for obtaining the geoid undulations by using these approaches.

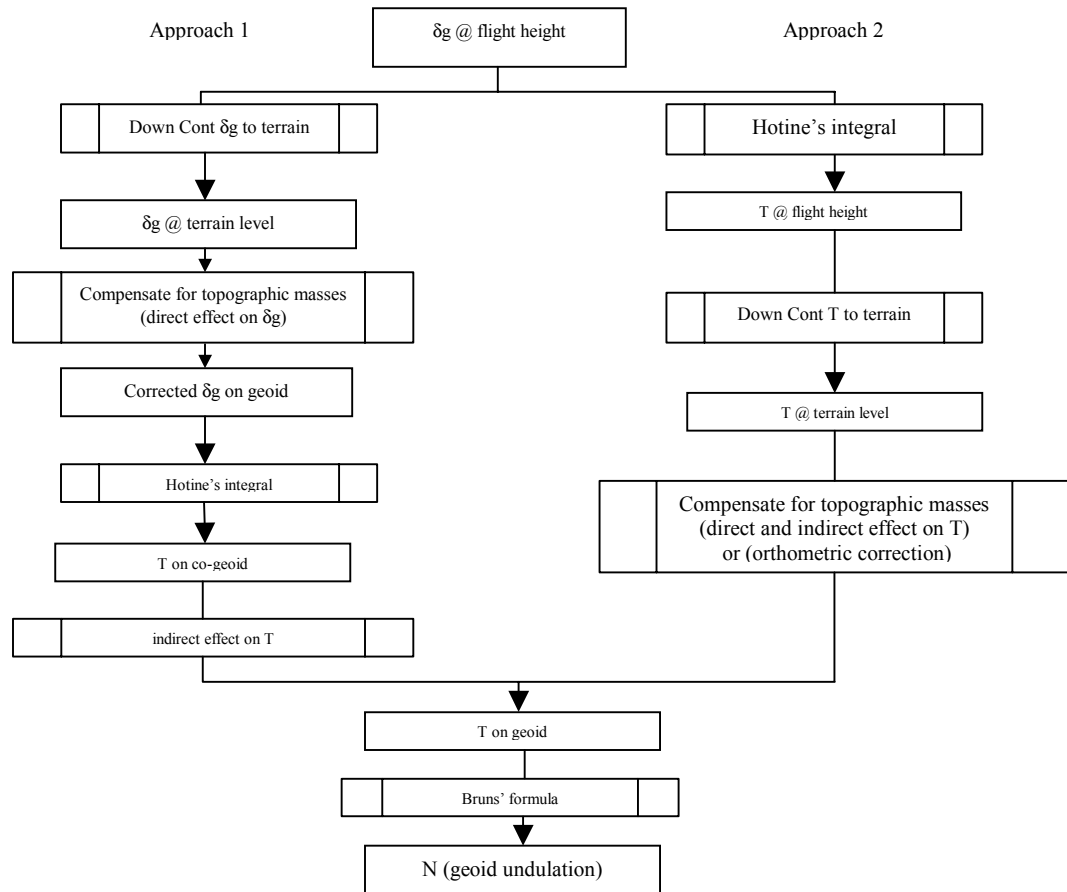


Figure 2.1: Flowchart for computing geoid undulations applying Hotine's integral

2.4 Relative geoid by profile integration

Another way to estimate the geoid is by determining its slope along a profile by the use of the horizontal components of the gravity vector. This method was used in the past when, by means of astronomical observations, the components of the deflections of the vertical were obtained and used for the so-called astrogeodetic geoid determination. The components of the deflection of the vertical were integrated along a profile to obtain the relative geoid. A similar procedure by using the horizontal components of the gravity vector along a profile line can be implemented for the determination of the disturbing potential at flight height. This technique has been applied by Jekeli and Kwon (2001) for relative geoid determination along a profile. One of the problems with this methodology was the fact that the computations had to be done at flight height since only one profile was used, and not enough information was available in order to refer the data to the terrain. On the other hand, if we could have several profiles providing areal information the downward continuation can be applied and we can expect better results.

Let us now concentrate on the determination of the disturbing potential by using the horizontal components of the gravity vector. The gravity disturbance vector is given by:

$$\delta \mathbf{g} = \mathbf{g} - \boldsymbol{\gamma} = \begin{pmatrix} \frac{\partial T}{(\rho_N + h)\partial \varphi} \\ \frac{\partial T}{(\rho_E + h)\cos \varphi \partial \lambda} \\ -\frac{\partial T}{\partial h} \end{pmatrix} = \begin{pmatrix} g_N - \gamma_N \\ g_E \\ g_D - \gamma_D \end{pmatrix}, \gamma_E = 0, \quad (2.4)$$

where, by having the horizontal components of the gravity disturbance vector at a constant ellipsoidal height, we get the basic relationship for the relative disturbing potential determination by means of the horizontal components of the gravity disturbance as (Jekeli and Kwon, 2001):

$$T(h_t, \varphi, \lambda) = T_1 + \int_{P_1}^{p(\varphi, \lambda)} (\delta g_N (\rho_N + h_t) d\varphi' + \delta g_E (\rho_E + h_t) \cos \varphi' d\lambda') \quad (2.5)$$

where $T(h_t, \varphi, \lambda)$ is the disturbing potential at an arbitrary point at flight h_t , here referred to an initial point P_1 with disturbing potential T_1 ; δg_N and δg_E are the corresponding north and east components of the gravity disturbance vector, ρ_N and ρ_E the radii of curvature of the reference ellipsoid, and h_t the flight height. One problem we face is the fact that we may not have access to the disturbing potential at the initial point and only the relative

change in disturbing potential can be known. Therefore, we need to somehow incorporate external information about the disturbing potential for the initial point of the profile line.

If, in some way, the disturbing potential can be downward continued to the topographic surface, then the height anomalies can be obtained by the use of Bruns' equation:

$$\zeta(\varphi_p, \lambda_p) = \frac{T(\varphi_p, \lambda_p, h_p)}{\gamma(H^N, \varphi_p)} \quad (2.6)$$

where h_p is the ellipsoidal height of a point on the topographic surface, γ the normal gravity, and H^N the normal (Molodensky) height of a point on the topographic surface (Jekeli and Kwon, 2001).

If we are now interested in determining the geoid we have to consider another step. One alternative would be to apply an orthometric correction that takes care of the curvature of the plumb line between the topographic surface and the geoid. We could use the following relation (Jekeli and Kwon, 2001; Heiskanen and Moritz, 1967, p.327):

$$N(\varphi_p, \lambda_p) = \zeta(\varphi_p, \lambda_p) + \frac{\Delta g_B(\varphi_p, \lambda_p)}{\bar{\gamma}} h_p \quad (2.7)$$

where $\Delta g_B(\varphi_p, \lambda_p)$ is the Bouguer gravity anomaly, which can be computed by the use of the vertical component of the gravity disturbance vector, and $\bar{\gamma}$ is the mean normal gravity along the normal plumb line between the ellipsoid and telluroid.

Since equation (2.7) yields only an approximation to the curvature effect, we suggest the use of another alternative to deal with this reduction. This is the application of Helmert's condensation method directly to the disturbing potential on the topographic surface. This approach will be described in section 2.7, and a diagram describing the steps to get the geoid can be observed in Figure 2.2:

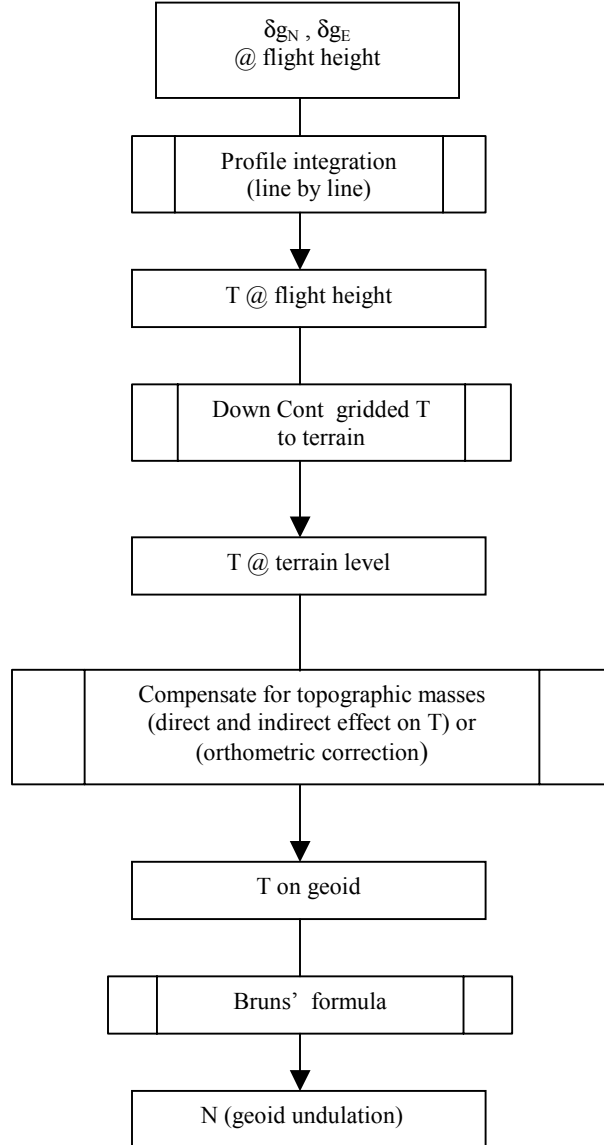


Figure 2.2: Flowchart for computing geoid undulations and application of profile integration

2.5 Least Squares Collocation (LSC)

Least squares collocation (LSC) is widely used when one is interested in the integration of spatially connected observations of different types in order to compute a related quantity of which, in the case of physical geodesy, they are functionals. In this section the basic principles for solving the prediction of such a signal by means of LSC are given. A description of the structure and characteristics of the covariance functions is introduced, focusing on the use of a local covariance function.

2.5.1 Basic formulas

Least Squares collocation is based on the adjustment within a mixed model where random and fixed parameters are treated simultaneously. The basic linearized observation equations for LSC can be written as:

$$y = A\xi + s + e \quad (2.8)$$

with:

- y .. a vector of observations,
- A .. the design matrix relating the fixed parameters to the observations,
- ξ .. a vector of fixed parameters to be estimated,
- s .. a vector of spatially connected random parameters to be predicted ($s = L T$),
- L .. a functional relating the signals to T,
- T .. the disturbing potential,
- e .. the vector of measurement errors.

For the case $A=0$ we can reduce equation (2.8) to the form :

$$y = s + e \quad (2.9)$$

Model (2.9) assumes that the quantities involved in the prediction are centered, therefore we need also to specify that the expectations $E(s)=E(y)=E(e)=0$.

The least squares solution for the predicted signal, assuming no correlation between s and e, $C(s,e)=0$, is given by (Moritz, 1970):

$$\tilde{s} = C_{st} (C_{tt} + D_{ee})^{-1} y \quad (2.10)$$

with C_{st} the signal cross-covariance matrix between estimation and observational sites,

C_{tt} the signal covariance matrix at the observational sites,

D_{ee} the noise covariance matrix of the observations.

And for the covariance of the predicted signal:

$$C_{\tilde{s}\tilde{s}} = C_{ss} - C_{st}(C_{tt} + D_{ee})^{-1} C_{ts} \quad (2.11)$$

with C_{ss} the signal covariance matrix at the estimation sites.

2.5.2 The covariance matrices

Prediction by least squares collocation depends strongly on the right choice of covariance function that forms the covariance matrices. The covariance functions in physical geodesy come from a basic covariance function for the disturbing potential, considered as a spatial stochastic process, from where other related covariance functions are determined by means of the law of covariance propagation. The covariance function is assumed to represent the behavior of a stationary, isotropic and ergodic process. By “stationary” we mean that the probability densities are parallel-shift invariant. This includes all joint density functions. By “isotropic” we mean that the process is invariant with respect to rotations (Moritz, 1989, p.170). And “ergodic” means that the statistics of the process (mean, variance and higher order moments) can be inferred from one realization of the process (Jekeli, 2000, p.176), by identifying its spatial averages with the probabilistic means.

Depending on the spatial distribution of the data, global and local covariance functions are used. Next, a brief description on the determination of the global and local covariance functions is presented.

2.5.2.1 Global covariance function

The basic covariance function, $K(P, Q)$, for the disturbing potential, considered as a spatial process on a sphere, which satisfies the requirements of stationarity is written in spectral form as (Moritz, 1989, p. 83):

$$K(P, Q) = \sum_{n=2}^{\infty} k_n P_n(\cos \psi) = C(T_P, T_Q) \quad (2.12)$$

where $k_n = \sum_{m=0}^n (C_{nm}^2 + S_{nm}^2)$, $S_{n,0} = 0$ for all $n \in \mathbf{N}$,

C_{nm} and S_{nm} : the spherical harmonic coefficients of the potential, and
 $\cos \psi = \cos \theta \cos \theta' + \sin \theta \sin \theta' \cos(\lambda' - \lambda)$.

The vertical extension of the basic covariance function, which is also harmonic outside the R-sphere, can be written according to Moritz (1989, p.169) as:

$$K(P, Q) = \sum_{n=2}^{\infty} k_n \left(\frac{R}{r r'} \right)^{n+1} P_n(\cos \psi) = C(T_P, T_Q). \quad (2.13)$$

From this function other covariance functions of quantities related to the disturbing potential are derived by the use of the law of covariance propagation. For details about the law of covariance propagation the reader is referred to Moritz (1989).

The spherical harmonic coefficients to be used in equation (2.12) are in general taken from an existing geopotential model and the upper limit for the summation for n is set to N_{\max} depending on the resolution of the chosen geopotential model. There also exist empirical models for the determination of this function, e.g. via variance component estimation (Schaffrin, 1981).

2.5.2.2 Local covariance function

For local applications of least squares collocation, the global covariance function does not model appropriately the spatial coherence of the quantities used for the adjustment. We need to define a more suitable local covariance function to be used for local prediction. In this case, a plane replaces the sphere, and the stationary and isotropic covariance function is only a function of the distance (Moritz, 1989, p.170):

$$K(P, Q) = K(d) \quad (2.14)$$

$$\text{with } d = \sqrt{(x_Q - x_P)^2 + (y_Q - y_P)^2}$$

Vertical harmonic extensions of the local covariances are needed mainly when relationships between the disturbing potential and a particular quantity involves the z coordinate, for instance when we want to derive the local covariance function between T and the down component of the gravity disturbance vector. The 3-D local covariance function may have the following form (Moritz, 1989, p.171):

$$K(P, Q) = K(d, z_Q + z_P) \quad (2.15)$$

which is no longer stationary in the vertical.

For the relation between the disturbing potential and the down component of the gravity vector we can write:

$$T_z = \frac{\partial T}{\partial z} = -\delta g_D \quad (2.16)$$

and, by means of the law of covariance propagation, we can determine the covariance between the disturbing potential and the vertical component of the gravity vector as:

$$\text{cov}[T(P), T_z(Q)] = \frac{\partial}{\partial z_Q} [K(d, z_Q + z_P)] \quad (2.17)$$

Similar to equation (2.16) we can establish other relationships related to the gradients of potential as follows:

$$T_x = \frac{\partial T}{\partial x} = \delta g_N, \quad T_y = \frac{\partial T}{\partial y} = \delta g_E.$$

From these equations we are now able to compute the covariances between the quantities involved as follows;

$$\begin{aligned} \text{cov}[T(P), T_x(Q)] &= \frac{\partial}{\partial x_Q} [K(d, z_Q + z_P)] \\ \text{cov}[T(P), T_y(Q)] &= \frac{\partial}{\partial y_Q} [K(d, z_Q + z_P)] \\ \text{cov}[T_x(P), T_x(Q)] &= \frac{\partial^2}{\partial x_P \partial x_Q} [K(d, z_Q + z_P)] \\ \text{cov}[T_y(P), T_y(Q)] &= \frac{\partial^2}{\partial y_P \partial y_Q} [K(d, z_Q + z_P)] \\ \text{cov}[T_z(P), T_z(Q)] &= \frac{\partial^2}{\partial z_P \partial z_Q} [K(d, z_Q + z_P)] \\ \text{cov}[T_x(P), T_y(Q)] &= \frac{\partial^2}{\partial x_P \partial y_Q} [K(d, z_Q + z_P)] \\ \text{cov}[T_x(P), T_z(Q)] &= \frac{\partial^2}{\partial x_P \partial z_Q} [K(d, z_Q + z_P)] \\ \text{cov}[T_y(P), T_z(Q)] &= \frac{\partial^2}{\partial y_P \partial z_Q} [K(d, z_Q + z_P)] \end{aligned}$$

Some models of spatial local covariance functions K can be found in Moritz (1989), Chapter 23. A particular model is introduced below in Chapter 3.

2.5.3 Spectral characteristics of the covariance function

The covariance function of two functions $h(x,y)$ and $g(x,y)$ for stationary data in 2-D is defined as (Schwarz et al., 1990) :

$$\begin{aligned} c_{hg}(x, y) &= E[(h(x_o, y_o) - \mu_h)(g(x_o + x, y_o + y) - \mu_g)] \\ &= R_{hg}(x, y) - \mu_g \mu_h \end{aligned} \quad (2.18)$$

where μ_h and μ_g are the mean values of the functions h and g , and R_{hg} is the homeogram given under ergodicity by:

$$R_{hg}(x, y) = E[h(x_0, y_0)g(x_0 + x, y_0 + y)]$$

$$= \lim_{\substack{X \rightarrow \infty \\ Y \rightarrow \infty}} \frac{1}{XY} \int_{-\frac{X}{2}}^{\frac{X}{2}} \int_{-\frac{Y}{2}}^{\frac{Y}{2}} h(x_0, y_0)g(x_0 + x, y_0 + y) dx_0 dy_0. \quad (2.19)$$

The spectrum of the covariance function is the power spectral density function (PSD) and it is given by the Fourier transform of the covariance function. The PSD function is given by (Jekeli, 2001):

$$S_{hg}(u, v) = F[c_{hg}(x, y)] = \lim_{\substack{X \rightarrow \infty \\ Y \rightarrow \infty}} E \left\{ \frac{1}{XY} H^*(u, v) G(u, v) \right\} \quad (2.20)$$

where $H^*(u, v)$ is the complex conjugate of the Fourier transform of $h(x, y)$, $G(u, v)$ the Fourier transform of $g(x, y)$, u and v the frequencies in the spectral domain, and X and Y the data interval in x and y directions.

The covariance function and the PSD are Fourier pairs and the covariance function can be written as:

$$c_{gh}(x, y) = F^{-1}[S_{hg}(u, v)] \quad (2.21)$$

2.6 Continuation of harmonic functions

When we need to know the values of a harmonic function above or below the surface where the actual values are given on, we have to continue (upward or downward) such a function through space. A harmonic function can be continued by the use of Poisson's integral. Depending on the desired continuation some problems have to be considered. Contrary to the upward continuation, the downward continuation of a noise set of data, representing a harmonic function, is problematic since it represents an ill-posed and ill-conditioned problem. When dealing with airborne data the downward continuation deserves special attention since we need to have our observations reduced to the terrain and then to the geoid. In this part the upward and downward continuation are studied and some basic formulas are given.

2.6.1 The upward continuation

If we need to know the values of a harmonic function above a reference surface we could use Poisson's integral. Poisson's integral is the solution of Dirichlet's problem for an exterior space, for a spherical boundary and it is written as (Heiskanen and Moritz, 1967, p. 35):

$$V(r, \theta, \lambda) = \frac{R(r^2 - R^2)}{4\pi} \int_{\lambda'=0}^{2\pi} \int_{\theta'=0}^{\pi} \frac{V(R, \theta', \lambda')}{l^3} \sin\theta' d\theta' d\lambda' \quad (2.22)$$

where $l = \sqrt{r^2 + R^2 - 2Rr\cos\psi}$; V is a harmonic function, and
 $\psi = \arccos[\cos\theta\cos\theta' + \sin\theta\sin\theta'\cos(\lambda' - \lambda)]$

We could also continue a harmonic function if we know the value of the gradients of such function on the surface. The function can be expanded as a Taylor series as follows:

$$V(R + h, \theta, \lambda) = V(R, \theta, \lambda) + \left. \frac{\partial V}{\partial r} \right|_{r=R} h + \frac{1}{2} \left. \frac{\partial^2 V}{\partial r^2} \right|_{r=R} h^2 + \dots$$

by neglecting second and higher order terms, this equation can be written in linear approximation as:

$$V(R + h, \theta, \lambda) \approx V(R, \theta, \lambda) + \left. \frac{\partial V}{\partial r} \right|_{r=R} h. \quad (2.23)$$

The radial derivative of the function V in a point $P(R, \theta, \lambda)$ taking values on a sphere of radius R , is given by (Heiskanen and Moritz, 1967, p.38):

$$\left. \frac{\partial V}{\partial r} \right|_{r=R} = -\frac{V_p}{R} + \frac{R^2}{2\pi} \int_{\lambda'=0}^{2\pi} \int_{\theta'=0}^{\pi} \frac{V(R, \theta', \lambda') - V_p}{l_o^3} \sin\theta' d\theta' d\lambda' \quad (2.24)$$

with $l_o = R\sqrt{2(1 - \cos\psi)} = 2R\sin\left(\frac{\psi}{2}\right)$

Note that this equation can be used as a gradient operator for either upward or downward continuation of a harmonic function. This formula can be used provided that the values of the function are given on a surface with constant radius.

2.6.2 The downward continuation:

Several ways to compute the downward continuation can be identified. The ones mostly used include the gradient method according to equation (2.23), the iterative solution, and the direct inversion of Poisson's integral. The latter method usually introduces a regularization parameter, which for real data is not easy to determine, as it is done by trial and error with simulated data (e.g., see Garcia, 2000). An optimal determination of the regularization parameter is introduced by Schaffrin et al., 2003; see also Koch and Kusche (2002). A brief introduction to the above methods is given next.

2.6.2.1 The gradient method

As already mentioned we could downward continue a harmonic function by the use of the radial derivative of such function. For the case of the disturbing potential we can write the Taylor series expansion as:

$$T(R, \theta, \lambda) = T(R + h, \theta, \lambda) - \frac{\partial T}{\partial r} \Big|_{r=R+h} h + \frac{1}{2} \frac{\partial^2 T}{\partial r^2} \Big|_{r=R+h} h^2 - \dots$$

Neglecting second and higher order terms we can write:

$$T(R, \theta, \lambda) \approx T(R + h, \theta, \lambda) - \frac{\partial T}{\partial r} \Big|_{r=R+h} h. \quad (2.25)$$

Now, under the assumption that the data are given on a surface of constant radius r we can make use of equation (2.24) yielding:

$$T(R, \theta, \lambda) \approx T(R + h, \theta, \lambda) - h \left[\frac{r^2}{2\pi} \int_{\lambda=0}^{2\pi} \int_{\theta'=0}^{\pi} \frac{T(R + h, \theta', \lambda') - T(R + h, \theta, \lambda)}{l_o^3} \sin \theta' d\theta' d\lambda' - \frac{T(R + h, \theta, \lambda)}{R + h} \right]$$

2.6.2.2 Iterative solution of Poisson's integral

Another way to downward continue the disturbing potential is by the use of equation (2.22) in an iterative way. In order to do so let us write this equation as:

$$T_p = \frac{R(r^2 - R^2)}{4\pi} \iint_{\sigma} \frac{T^*}{l^3} d\sigma \quad (2.26)$$

with $T^* = T(R, \varphi', \lambda')$ the disturbing potential on σ that generates the disturbing potential $T_p = T(r, \varphi, \lambda)$ at a height h_p , and $r = R + h_p$.

We can now multiply both sides by R/r giving:

$$\frac{R}{r} T_p = \frac{R^2(r^2 - R^2)}{r4\pi} \iint_{\sigma} \frac{T^*}{l^3} d\sigma, \quad (2.27)$$

and using the substitution (Heiskanen and Moritz, 1967, p.317)

$$D = \frac{l}{R + h_p} \quad t = \frac{R}{r}$$

now write equation (2.27) as:

$$tT_p = \frac{t^2(1-t^2)}{4\pi} \iint_{\sigma} \frac{T^*}{D^3} d\sigma \quad (2.28)$$

Using the identity (Heiskanen and Moritz, 1967; equation (8-86))

$$t^2 = \frac{t^2(1-t^2)}{4\pi} \iint_{\sigma} \frac{d\sigma}{D^3} \quad (2.29)$$

and multiplying (2.29) by T_p^* and subtracting it from (2.28) gives:

$$tT_p - t^2T_p^* = \frac{t^2(1-t^2)}{4\pi} \iint_{\sigma} \frac{T^* - T_p^*}{D^3} d\sigma \quad (2.30)$$

which can be written as:

$$T_p^* = \frac{T_p}{t} - \frac{1-t^2}{4\pi} \iint_{\sigma} \frac{T^* - T_p^*}{D^3} d\sigma. \quad (2.31)$$

This equation can be evaluated iteratively where we solve for T_p^* . For its solution we begin by taking:

$$(T_o^*)_p = T_p$$

and for the first iteration we compute

$$(T_1^*)_p = \frac{T_p}{t} - \frac{1-t^2}{4\pi} \iint_{\sigma} \frac{T_o^* - (T_o^*)_p}{D^3} d\sigma$$

with this result we compute the next iteration as:

$$(T_2^*)_p = \frac{T_p}{t} - \frac{1-t^2}{4\pi} \iint_{\sigma} \frac{T_1^* - (T_1^*)_p}{D^3} d\sigma$$

and so

on for the rest of points.

For values of T_p given at a constant altitude h , we can now write equation (2.31) is planar approximation as:

$$T_p^* \approx T_p - \frac{h}{2\pi} \iint_E \frac{T^* - T_p}{l_p^3} dx dy \quad (2.32)$$

with :

$$l_p = \sqrt{(x - x_p)^2 + (y - y_p)^2 + h^2},$$

where we consider the following approximations:

$$r^2 - R^2 \cong 2RH, \quad r R d\sigma \cong R^2 d\sigma \cong dx dy \quad \text{and} \quad \frac{R}{r} \approx 1.$$

2.6.2.3 Inversion of Poisson's integral

By means of inverting equation (2.22) we can downward continue a harmonic function. This equation can be written as:

$$\mathbf{V}_r = \mathbf{A} \mathbf{V}_R \quad (2.33)$$

$$\text{with } \mathbf{A}_{n \times m} = \left[\frac{R(r_i^2 - R^2)}{4\pi} \sum_{\lambda'} \sum_{\theta'} \frac{1}{l_{ij}^3} \sin \theta'_j \delta \theta'_j \delta \lambda'_i \right]$$

$$\mathbf{V}_R = \begin{bmatrix} V(R, \theta'_1, \lambda'_1) \\ V(R, \theta'_2, \lambda'_2) \\ V(R, \theta'_3, \lambda'_3) \\ \vdots \\ V(R, \theta'_m, \lambda'_m) \end{bmatrix}_{m \times 1} \quad \text{and} \quad \mathbf{V}_r = \begin{bmatrix} V(r_1, \theta_1, \lambda_1) \\ V(r_2, \theta_2, \lambda_2) \\ V(r_3, \theta_3, \lambda_3) \\ \vdots \\ V(r_n, \theta_n, \lambda_n) \end{bmatrix}_{n \times 1}$$

The least squares solution is given by:

$$\hat{\mathbf{V}}_R = (\mathbf{A}^T \mathbf{A})^{-1} \mathbf{A}^T \mathbf{V}_r \quad (2.34)$$

The inversion of the matrix in parenthesis in equation (2.34) is problematic since this matrix represents an ill-conditioned system. A regularization scheme might be adopted. The solution is found by adding a regularization parameter α to the diagonal elements and to invert as follows:

$$\hat{\mathbf{V}}_R = (\mathbf{A}^T \mathbf{A} + \alpha \mathbf{I})^{-1} \mathbf{A}^T \mathbf{V}_r \quad (2.35)$$

An extensive study of how to determine the regularization parameter can be found in Garcia, R (2000), and an “optimal” choice is provided by Schaffrin et al. (2003).

2.7 Reduction of observations for geoid determination

The solution for the disturbing potential by the use of Hotine's formula assumes that there are no masses above the boundary surface. In reality, airborne measurements are taken at a certain height above the terrain. For the case of the down component of the gravity disturbance vector, it can first be reduced to the topography by downward continuation or by simply applying a free-air reduction. Then we have to remove the effect of the visible topography and refer our measurements to the geoid. For the horizontal components, on the other hand, we could first compute the disturbing potential at altitude and downward continue it to the terrain, and then remove the effect of the terrain on the potential. Some methodologies for the reduction of our observations to the boundary surface are introduced next.

2.7.1 Traditional approach for geoid computation

Let assume that we have our measurement referred to the terrain. The traditional process for reducing gravity observations to the geoid can be summarized as (Heiskanen and Moritz, 1967, p.138):

- 1) Removal of visible topography
- 2) Removal of the compensation
- 3) Projection of the point into the geoid

The first step is carried out by the so-called topographic correction (Heiskanen and Moritz, 1967); it consists of the removal of the gravitational effect caused by an infinite slab of height equal to h_p (the height of the point where measurements are taken); this is called the Bouguer correction. For the remaining topography not corrected by the Bouguer correction, a refined correction has to be applied. The latter is called the terrain correction. Then the gravity disturbance due to the full topography can be written as:

$$\delta g_T = \delta g_p - 2\pi G \rho h_p + A_t \quad (2.36)$$

with $\delta g_p = g_p - \gamma_p$ the gravity disturbance for a point P on the topography, $2\pi G \rho h_p$ the Bouguer correction, h_p the orthometric height of P, and A_t the terrain correction in P. G and ρ denote the Newton's gravitational constant and terrain density respectively.

The terrain correction in planar approximation can be written as (Wang and Rapp, 1990):

$$A_t = \frac{1}{2} G \rho \iint \frac{(h - h_p)^2}{d^3} dx dy \quad (2.37)$$

with $d = \sqrt{(x - x_p)^2 + (y - y_p)^2 + (h - h_p)^2}$.

In the second step, the intention is to regularize the earth crust according to an isostatic model, which can be done by shifting masses associated with the previous reduction under the boundary surface. There exist two models for isostatic compensation that are used, the Pratt-Hayford and the Airy-Heiskanen model (Heiskanen and Moritz, 1967, section 3-4). Now, we could write for the gravity anomalies:

$$\delta g_I = \delta g_T + A_I \quad (2.38)$$

with A_I the isostatic correction, obtained by the application of one particular model . Formulas for this correction can be found in Heiskanen and Moritz (1967), in section 3-4.

The third step is to lower the point of computation to the boundary surface level. This is taken into account by the Free-air reduction, which can be approximated using the gradient of normal gravity and can be written as (Heiskanen and Moritz, 1967, p.131):

$$F \cong -(\partial\gamma/\partial h) \big|_p h = 0.3086 h_p \quad (2.39)$$

Notice, however, that we are dealing with gravity disturbances, meaning that both g_p and γ_p are referred to the topography and our goal is to reduce both quantities to the geoid. We can approximate the gradient of gravity by the gradient of normal gravity. This means that in applying the free-air reduction to both gravity values, the free-air correction will cancel out. Therefore we can omit this correction and the gravity disturbance on the boundary surface can now be written exactly as equation (2.38), which we repeat here:

$$\delta g = \delta g_T + A_I \quad (2.40)$$

We can now compute the geoid by the procedure explained in section 2.3. Actually, we are on a surface different than the geoid since we have changed the potential by removing the topographic masses; this change is referred to as the “indirect effect”. Applying Bruns’ formula will therefore lead to a surface called “co-geoid”. Different gravity reductions generate different co-geoids (Heiskanen and Moritz, 1967, p.141). This means that in order to obtain the geoid, a correction term has to be added:

$$N = \frac{R}{4\pi\gamma} \iint_{\sigma} \delta g H(\psi) d\sigma + \delta N \quad (2.41)$$

where δN is given by the change of potential on the boundary surface divided by normal gravity (γ) (Heiskanen and Moritz, 1967, eq.(3-67)). For the case of isostatic gravity anomalies the value of δN is in the order of 10 m (Heiskanen and Moritz, 1969, p.142).

2.7.2 Helmert's condensation method

An alternative way, and the one mostly used today, for reducing gravity observations is Helmert's second condensation method. It consists of the radial condensation of the topography above the boundary surface into a thin surface layer on this surface (Heiskanen and Moritz, 1967, p.145). These masses are condensed along the local vertical with density (Heiskanen and Moritz, 1967, p.145; Vaniček and Martinec, 1994):

$$k = \bar{\rho} h_p \quad (2.42)$$

where $\bar{\rho}$ is the average density of the terrain along the normal plumb line up to the height h_p , and k represents the "layer density".

The gravity disturbance, needed for Hotine's integral on the boundary surface, can now be computed as:

$$\delta g = g_p - \gamma_P - A_T + A_H \quad (2.43)$$

where A_H is the attraction due to the condensed layer with density k , and A_T is the attraction due to the topography.

There have been some discussions about the right way to apply this technique. Several algorithms and solutions have been developed in the last years. The discussion has been about where the effect of the attraction of the condensed layer must be evaluated. The classical approach (Moritz, 1968; Pellinen, 1962; Wang and Rapp, 1990) argues that the attraction of the layer has to be evaluated at the corresponding point on the boundary surface and not at terrain level as stated by Vaniček and Kleusberg, 1987, and Vaniček and Martinec, 1994. The difference between these two approaches is in the order of the application of the downward continuation, and according to Jekeli and Serpas, 2003 both solutions are theoretically equivalent. The classical method shows to provide better results, with actual data, mainly in mountain areas.

For the gravity disturbances to be used to compute the geoid in the classical approach we can write a relation similar to (Jekeli and Serpas, 2003):

$$\delta g_{MP} = g_p - A_T(P) + A_H(P_0) + D(g_B) - \gamma_{P'} \quad (2.44)$$

where $g_B = g_p - A_T(P)$ are the Bouguer gravities, $D(g_B)$ the downward continuation of the refined Bouguer gravity, and $\gamma_{P'}$ the normal gravity evaluated at the corresponding geoid point P' . The subscript MP is used to identify equation (2.44) with the traditional approach due to Moritz (1968) and Pellinen (1962).

On the assumption that the Bouguer gravity field is rather smooth the downward continuation term in equation (2.44) can be neglected, and considering only the effects of the topography and the layer, we can write for the computation of the geoid:

$$N = \frac{R}{4\pi\gamma} \iint_{\sigma} (\delta g + C) H(\psi) d\sigma + \delta N_I \quad (2.45)$$

where $\delta g = g_p - \gamma_p$, and C being the same as $(-A_T + A_H)$. The correction term C happens to be in planar approximation identical to the terrain correction (Wang and Rapp, 1990):

$$C = \frac{1}{2} G \rho \iint \frac{(h - h_p)^2}{d^3} dx dy = A_t \quad (2.46)$$

The term δN_I in (2.45) that compensates for the change in potential (“indirect effect”) is often neglected, but in this context should be considered since it can reach up to 5 cm for an elevation of 1000 m (Moritz, 1989, p. 418). This term can be computed as (Heiskanen and Moritz, 1967, p.142; Wang and Rapp, 1990):

$$\delta N_I = \delta W_I / \gamma \quad (2.47)$$

where δW_I is the difference in potential between the mass of the actual topography and the mass of the condensed layer $W_T - W_H$. δW_I has to be evaluated at geoid level, and it can be written in planar approximation for the potential of both masses as (Wang and Rapp, 1990):

$$W_T = G \rho \int_{\alpha}^{2\pi} \int_{l=0}^{\infty} \int_{z=0}^{h_0} \frac{1}{l} dl d\alpha dz \quad (2.48)$$

$$W_H = G \rho \int_0^{2\pi} \int_{l=0}^{\infty} h dl d\alpha \quad (2.49)$$

By solving these integrals we can write for δN_I (Wang and Rapp, 1990; Wichiencharoen, 1982):

$$\delta N_I = \frac{-\pi G \rho h^2}{\gamma} - \frac{1}{6} \frac{G \rho}{\gamma} \iint \frac{h^3 - h_p^3}{d^3} dx dy \quad (2.50)$$

which provides the equation for computing the indirect effect.

2.7.3 Helmert’s condensation method applied directly to the potential

We will now describe how to apply Helmert’s condensation method directly to the disturbing potential. This would be useful for the case of computing the disturbing potential directly by line integral from the horizontal components of the gravity vector and accounting for the effects of the topography and the condensed layer.

Similar to the gravity reductions, once the disturbing potential has been computed at terrain level we can write the disturbing potential at the geoid according to the Moritz and Pellinen approach (MP) as:

$$\begin{aligned} T(P_0) &= T_p - \delta V_{\text{Topo}}(P) + \delta V_{\text{layer}}(P_0) + D(T_{\text{MP}}) + \gamma \delta N_I \\ \text{or } T &= T_p + \delta V_{\text{MP}} + D(T_{\text{MP}}) + \gamma \delta N_I \end{aligned} \quad (2.51)$$

where $\delta V_{MP} = \delta V_{layer}(P_0) - \delta V_{Topo}(P)$,
 $D(T_{MP})$: the downward continuation of the MP disturbing potential,
 T_{MP} : the argument for the downward continuation = $T_P - \delta V_{Topo}(P)$,
 $\delta V_{Topo}(P)$: the potential due to the topography at point P on the terrain,
 $\delta V_{layer}(P_0)$: the potential due to the layer evaluated at the corresponding point P_0 on the boundary surface, and
 $\gamma \delta N_I = [\delta V_{Topo}(P_0) - \delta V_{layer}(P_0)]$ the indirect effect.

If we now consider the net effect of the removal and restoration of the masses and group together the expressions for the direct and indirect effect, we can rewrite equation (2.51) as:

$$T = T_p + D(T_{MP}) + \delta T_N \quad (2.52)$$

with

$$\delta T_N = \delta V_{layer}(P_0) - \delta V_{Topo}(P) + \delta V_{Topo}(P_0) - \delta V_{layer}(P_0) = \delta V_{Topo}(P_0) - \delta V_{Topo}(P)$$

We now need to write the expressions for the potential effects due to the topography evaluated at P and P_0 . For the potential effect due to the topography evaluated at P we have:

$$\delta V_{Topo}(P) = G\rho \iint_{\sigma} \int_{r=R}^{R+h_p} \frac{r^2}{l} dr d\sigma + G\rho \iint_{\sigma} \int_{r=R+h_p}^{R+h} \frac{r^2}{l} dr d\sigma \quad (2.53)$$

if we use planar approximation, i.e. neglect terms of the order of h/R in l , which for local computation is possible. We can rewrite equation (2.53) as (Moritz, 1968):

$$\delta V_{Topo}(P) = 4\pi G\rho h_p R + G\rho R^2 \iint_{\sigma} \int_{z=h_p}^h \frac{dz d\sigma}{l} \quad (2.54)$$

$$\text{with } l^2 = l_o^2 \left(1 + \frac{(z-h_p)^2}{l_o^2} \right).$$

If we expand in series the reciprocal of the distance and under the assumption that $\frac{(z-h_p)^2}{l_o^2} < 1$, equation (2.51) is written as:

$$\begin{aligned} \delta V_{Topo}(P) = 4\pi G\rho h_p R + G\rho R^2 \iint_{\sigma} \frac{h-h_p}{l_o} d\sigma - \\ - \frac{1}{6} G\rho R^2 \iint_{\sigma} \frac{(h-h_p)^3}{l_o^3} d\sigma + \frac{3}{40} G\rho R^2 \iint_{\sigma} \frac{(h-h_p)^5}{l_o^5} d\sigma - \dots \end{aligned} \quad (2.55)$$

Similarly, for the effect of the potential due to the topography evaluated at P_0 we have:

$$\delta V_{\text{Topo}}(P_0) = 4\pi G \rho h_p R + G \rho R^2 \iint_{\sigma} \int_{z=h_p}^h \frac{dz d\sigma}{l} \quad (2.56)$$

$$\text{with } l^2 = l_o^2 \left(1 + \frac{z^2}{l_o^2} \right).$$

Again expanding the reciprocal of the distance into a series and under the assumption that $\frac{z^2}{l_o^2} < 1$, we finally arrive at:

$$\begin{aligned} \delta V_{\text{Topo}}(P_0) = & 4\pi G \rho h_p R + G \rho R^2 \iint_{\sigma} \frac{h - h_p}{l_o} d\sigma - \\ & - \frac{1}{6} G \rho R^2 \iint_{\sigma} \frac{h^3 - h_p^3}{l_o^3} d\sigma + \frac{3}{40} G \rho R^2 \iint_{\sigma} \frac{h^5 - h_p^5}{l_o^5} d\sigma - \dots \end{aligned} \quad (2.57)$$

From equations (2.55) and (2.57) we can see that the net effect on the potential can be neglected if the linear approximation is assumed (i.e. neglect quadratic and higher order terms in h). If we only consider the planar approximation, which includes cubic terms in h , the expression for the net effect is given by:

$$\delta T_N = \delta V_{\text{Topo}}(P_0) - \delta V_{\text{Topo}}(P) = -\frac{1}{2} G \rho R^2 h_p^2 \iint_{\sigma} \frac{h}{l_o^3} d\sigma + \frac{1}{2} G \rho R^2 h_p \iint_{\sigma} \frac{h^2}{l_o^3} d\sigma \quad (2.58)$$

CHAPTER 3

NUMERICAL ASPECTS OF GEOID COMPUTATION

3.1 Introduction

Most of the relationships described in chapter 2, are valid for data that are globally distributed, and for continuous data coverage. None of these characteristics is true for local or regional geoid determination. Our observations are discrete and limited to certain regions of the Earth. Moreover, truncation errors for the models used and edge effects due to limited data are present in our results. The way to deal with these situations from the numerical point of view is addressed in this chapter. Also computational techniques such as the FFT (Fast Fourier Transform) are presented.

3.2 The Fourier Transform and the FFT

The Fast Fourier Transform (FFT) is an algorithm that allows us to compute the Fourier transform of discretely gridded data. Due to the convenience to manage data in the spectral domain, by the use of some of the properties of the Fourier transform, its application is widely appreciated for numerical solutions in physical geodesy, mostly in planar approximation.

A brief description of the definitions and some properties associated with the Fourier transform are introduced in the following. The 2-D continuous Fourier transform (CFT) is defined as (Schwarz et al., 1990) as:

$$G(u, v) = \int_{-\infty}^{\infty} \int_{-\infty}^{\infty} g(x, y) e^{-i2\pi(ux+vy)} dx dy = \mathbf{F}[g(x, y)] \quad (3.1)$$

where G is called the “spectrum” of the function $g(x, y)$; u and v are the spatial frequencies corresponding to the x and y directions respectively, \mathbf{F} the 2D Fourier operator, and i the imaginary number defined as: $i = \sqrt{-1}$.

The function $g(x, y)$ in the space domain can be related by an inverse operation to its Fourier transform by:

$$g(x, y) = \int_{-\infty}^{\infty} \int_{-\infty}^{\infty} G(u, v) e^{i2\pi(ux+vy)} du dv = \mathbf{F}^{-1}[G(u, v)] \quad (3.2)$$

where \mathbf{F}^{-1} is called the 2-D Fourier inverse operator.

As already mentioned, in practice our data are only given at discrete points and are of limited extent. Therefore we need to find a formulation for the discrete case. Let us begin with an estimate of the spectrum for a function defined on a finite interval. This is given by (Schwarz et al., 1990):

$$G_F(u, v) = \int_{-\frac{X}{2}}^{\frac{X}{2}} \int_{-\frac{Y}{2}}^{\frac{Y}{2}} g_F(x, y) e^{-i2\pi(ux+vy)} dx dy \quad (3.3)$$

with the data given in the interval $-\frac{X}{2} \leq x \leq \frac{X}{2}$, $-\frac{Y}{2} \leq y \leq \frac{Y}{2}$.

If we now consider our data to represent a periodic process, the spectrum becomes discrete and the corresponding discrete Fourier transform (DFT) for discrete gridded data, in the directions x and y , can be approximated by transforming the integrals in equations (3.1) and (3.2) into the respective summations as follows:

$$G(m\Delta u, n\Delta v) = \Delta x \Delta y \sum_{k=0}^{M-1} \sum_{l=0}^{N-1} g(k\Delta x, l\Delta y) e^{-i2\pi\left(\frac{mk}{M} + \frac{nl}{N}\right)} = \mathbf{DFT}[g] \quad (3.4)$$

with $m = 0, 1, \dots, M-1$; and $n = 0, 1, \dots, N-1$;

$$g(k\Delta x, l\Delta y) = \Delta u \Delta v \sum_{k=0}^{M-1} \sum_{l=0}^{N-1} G(m\Delta u, n\Delta v) e^{i2\pi\left(\frac{mk}{M} + \frac{nl}{N}\right)} = \mathbf{DFT}^{-1}[G] \quad (3.5)$$

with $k = 0, 1, \dots, M-1$; and $l = 0, 1, \dots, N-1$;

where $\Delta u = \frac{1}{M\Delta x}$, $\Delta v = \frac{1}{N\Delta y}$, and M and N are the number of data points in both x and y directions respectively.

Due to the discrete characteristics of (3.4) and (3.5), it can be shown that the maximum frequencies that can be recovered from a given discrete data set are:

$$u_n = \frac{1}{2\Delta x}, \text{ and } v_n = \frac{1}{2\Delta y}$$

the so-called ‘‘Nyquist frequencies’’.

The set of equations (3.4) and (3.5) are the basis for the FFT algorithm used to evaluate the DFT. The FFT is an algorithm that uses prime factorizations of M and N , and is fastest when M and N are powers of 2 (Schwarz et al., 1990).

In general, the relation of the spatial and spectral domains by the Fourier transform are symbolically represented by the so called Fourier transform pairs as:

$$h(x, y) \leftrightarrow H(u, v) . \quad (3.6)$$

As we mentioned before, the Fourier transform has some properties that are convenient in certain applications in Physical Geodesy. One of these applications is the convolution defined as follows:

$$[h * g](x, y) = \int_{-\infty}^{\infty} \int_{-\infty}^{\infty} h(x_0, y_0) g(x_0 - x, y_0 - y) dx_0 dy_0 = [g * h](x, y) \quad (3.7)$$

where the symbol $*$ represents the convolution.

The convolution has the important characteristic that in the spectral domain the convolution becomes just a simple multiplication:

$$[h * g](x, y) \leftrightarrow H(u, v) G(u, v) . \quad (3.8)$$

Another important function, which has been introduced in formula (2.19) already, is the homeogram (under ergodicity):

$$[g \boxtimes h](x, y) = \int_{-\infty}^{\infty} \int_{-\infty}^{\infty} h(x_0, y_0) g(x_0 + x, y_0 + y) dx_0 dy_0 \quad (3.9)$$

where the symbol \boxtimes represents the homeogram between the functions h and g , evaluated at a shift (x, y) .

The homeogram has the following characteristic in the spectral domain:

$$[g \boxtimes h](x, y) \leftrightarrow G(u, v)^* H(u, v) \quad (3.10)$$

with $G(u, v)^*$ the complex conjugate of $G(u, v)$.

In the discrete case we can write both (3.8) and (3.10) as:

$$\begin{aligned} [h * g](k\Delta x, l\Delta y) &\leftrightarrow H(m\Delta u, n\Delta v) G(m\Delta u, n\Delta v) \\ [g \boxtimes h](k\Delta x, l\Delta y) &\leftrightarrow G(m\Delta u, n\Delta v)^* H(m\Delta u, n\Delta v) \end{aligned}$$

In most convolutions used in physical geodesy one of the functions acts as a weighting function and is called the “kernel function”. In general, this function involves inverses of the distance to some power. The function being weighted by the kernel function is called the “signal”.

As mentioned before, we can take advantage of these and other important properties of the Fourier transform and the use of the FFT algorithm, but in doing so we have also to be careful about some problems inherent to their numerical application with discrete and limited data. The DFT is defined only for periodic functions, and by its use our data are to be considered periodic. The finite Fourier transform represented by equation (3.3) assumes that any particular function is multiplied with a “box” function assigning a weight of 1 to the signal in the interval where data for the signal are available, and 0 outside the interval of the signal. This multiplication in the space domain implies a convolution in the frequency domain. The Fourier transform of the “box” function is

given by the sinc function ($\text{sinc}(f)=[\sin(\pi f)/(\pi f)]$), which causes a “leakage” effect to the representation of the spectrum of the signal. Moreover, a convolution of discrete functions is represented as a cyclic convolution and the fact that our data have limited extent will cause errors coming from the edges where the two functions are convolved with the wrong data, due to the “wrap-around” effect in the space domain. The effect of leakage is always present whenever we use the finite Fourier transform and it can be diminished by the use of windowing schemes different from a rectangular one. On the other hand, errors due to cyclic convolutions are eliminated by the use of zero padding for the signal and symmetric padding for the kernel (Jekeli, 1998a).

3.3 Numerical implementation of Hotine’s integral

Hotine’s integral provides geoid undulations from gravity disturbance data distributed all over the boundary surface. Our measurements of gravity, however, are not available at every point on the boundary surface. We only have access to gravity information at specific limited areas of the Earth, which may be gridded at regular intervals in terms of latitude and longitude. This means that only information about high frequencies of the gravity field can be retrieved from our data, limited by the grid interval. The general method to include lower frequency information is the application of a remove–restore technique. First we subtract the low frequency gravity disturbances from the data. These gravity disturbances can be obtained from an existing geopotential model (e.g. EGM96). After the contributions to the geoid undulations have been computed from the residual gravity disturbances, the removed field has to be restored, but now as long-wavelength geoid undulations, again, coming from the same existing model. Let us now focus on the computation of geoid undulations by the use of Hotine’s integral. Suppose we have gravity disturbances reduced to the geoid, the solution in spherical approximation is written as:

$$N = \frac{R}{4\pi\gamma} \iint_{\text{cap}} (\delta g_D - \delta g_{2,360}) H'(\psi) d\sigma + N_{2,360} \quad (3.11)$$

where δg_D is the observed down component of the gravity disturbance vector, reduced to the geoid. Strictly speaking, we should use the gravity disturbance. In this case, the down component of the gravity disturbance vector provides, to first order in deflection of the vertical, a good approximation to the gravity disturbance.

In equation (3.11) we also identify the following quantities:

$$N_{2,360}(r, \theta, \lambda) = \frac{GM}{r\gamma} \sum_{n=2}^{360} \left(\frac{R}{r}\right)^n \sum_{m=-n}^n \bar{C}_{nm} \bar{Y}_{nm}(\theta, \lambda)$$

$$\delta g_{2,360}(r, \theta, \lambda) = \frac{GM}{r^2} \sum_{n=2}^{360} (n+1) \left(\frac{R}{r}\right)^n \sum_{m=-n}^n \bar{C}_{nm} \bar{Y}_{nm}(\theta, \lambda)$$

\bar{C}_{nm} being the fully normalized coefficients for the disturbing potential ,

$$\bar{Y}_{nm} = \bar{P}_{nm}(\cos\theta) \begin{cases} \cos(m\lambda), & m \geq 0 \\ \sin(|m|\lambda), & m < 0 \end{cases},$$

\bar{P}_{nm} the fully normalized Legendre polynomials, and
 $r=R+h$, the distance from the geocenter at which, for this case, the geoid
undulation and gravity disturbances are evaluated.

The modeled gravity disturbances and geoid undulations (δg_{2-360} , N_{2-360}) are given under the assumption that the normal potential on the reference ellipsoid is equal to the gravity potential on the geoid, and that the center of such ellipsoid coincides with the center of mass of the Earth. It is also assumed that the mass of the ellipsoid coincides with the mass of the geoid.

The computation of Hotine's integral can be achieved by the use of the FFT. In this case, 1-D FFT along parallels and numerical summation along meridian will be used. For discrete data, Hotine's formula can be approximated as (Haagmans et al., 1993):

$$N_{\varphi_p}(\lambda_p) = \frac{R\Delta\varphi\Delta\lambda}{4\pi\gamma} \sum_{\varphi_q=\varphi_1}^{\varphi_n} \left[\sum_{\lambda_q=\lambda_1}^{\lambda_m} H'_{\varphi}(\Delta\lambda_{pq}) \delta g_{\varphi_q}(\lambda_q) \cos\varphi_q \right] \quad (3.12)$$

where $N_{\varphi_p}(\lambda_p)$ is the geoid undulation at all points located on the parallel of φ_p ; H' is Hotine's kernel given by equation (2.3); $\Delta\varphi$ and $\Delta\lambda$ are the spacings on meridian and parallel circles. Notice that $H'_{\varphi}(\Delta\lambda_{pq}) = H'_{\varphi_p\varphi_q}(\lambda_p - \lambda_q) = H'(\psi_{pq})$.

Now Hotine's integral can be evaluated via the 1D-FFT for each parallel, and by numerical integration along the meridians. We can then write equation (3.12) as (Haagmans et al, 1993):

$$N_{\varphi_p}(\lambda_p) = \frac{R\Delta\varphi\Delta\lambda}{4\pi\gamma} \mathbf{DFT}^{-1} \left\{ \sum_{\varphi_q=\varphi_1}^{\varphi_n} \mathbf{DFT}\{H'_{\varphi}\}_{\lambda} \mathbf{DFT}\{\delta g_{\varphi_q} \cos\varphi_q\}_{\lambda} \right\} \quad (3.13)$$

Hotine's kernel presents singularities at the origin. In order to deal with this problem, a value of zero is forced at the origin when evaluating equation (3.13), and after the computations are done, the value for the origin has to be restored. For doing so, we proceed in analogy to the case of Stokes' kernel. In the neighborhood of the origin for Hotine's kernel, the case when $\psi \rightarrow 0$, we see that the first term is dominant, and the following approximations can be done:

$$H'(\psi) \approx \frac{1}{\sin\left(\frac{\psi}{2}\right)} \approx \frac{1}{\left[\frac{\psi}{2}\right]} = \frac{2}{\psi} \approx \frac{2R}{d}$$

and, similar to Heiskanen and Moritz (1967, p.122), and Schwarz et al (1990) equation (101b) we can write for the computation of N at the origin:

$$N(\varphi_p, \lambda_p) \approx \frac{\sqrt{\Delta x \Delta y}}{\gamma \sqrt{\pi}} \delta g(\varphi_p, \lambda_p) \quad (3.14)$$

with $\Delta x = R \Delta \varphi$, and $\Delta y = R \Delta \lambda \cos(\varphi_p)$.

The fact that Hotine's integral is evaluated with data over a limited area will introduce errors in the results near the edges. In addition, the use of discrete gridded data assumes periodicity in the application of the FFT. As mentioned before, this induces a wrap-around effect in the results due to cyclic convolutions that can be avoided by the use of an appropriate padding scheme. Zero-padding the signal over a domain doubled in both dimensions, and using a symmetric padding for the kernel, will eliminate the problem associated with the cyclic convolutions. In order to reduce the edge effects in our results we should have to consider a larger area for the computations and restrict the results to a reduced central area. On the other hand, considering a larger area for the computation to avoid edge effects is problematic when limited data are available, and the use of modeled quantities, in addition to taking care of long-wavelength components in the data, will help to diminish this effect. Any errors coming from the model used for the long wavelength components of the signal will be present in the results.

3.4 Numerical implementation of the line integral for relative geoid determination

The line integral for computing the geoid from the horizontal components as described in section 2.4 can be written as a summation along the line of flight. The initial value, T_1 in equation (2.5), represents the initial value for the disturbing potential. Generally we do not know this value and we need external information about the disturbing potential at the initial point. The use of minimal external information is addressed in Section 5.3. This value could be set to zero, in which case only the relative geoid would be computed (i.e. undulation differences). Then the disturbing potential referred to the initial point can be approximated as follows:

$$T(h_m, \varphi_i, \lambda_i) = T_1 + \sum_{i=2}^n [\delta g_N(\rho_N + h_m)]_i \Delta \varphi_i + [\delta g_E(\rho_E + h_m) \cos \varphi_m]_i \Delta \lambda_i \quad (3.15)$$

where

n is the number of points along the profile of interest, and

$\varphi_m = \frac{\varphi_{i-1} + \varphi_i}{2}$ is the mean latitude between consecutive points in the profile;

$h_m = \frac{h_{i-1} + h_i}{2}$ is the mean ellipsoidal height between two consecutive points in the profile,

$\rho_N = \frac{a(1-e^2)}{[1-e^2 \sin^2(\varphi_m)]^{\frac{3}{2}}}$ is the radius of curvature of the meridian plane,

$\rho_E = \frac{a}{[1-e^2 \sin^2(\varphi_m)]^{\frac{1}{2}}}$ is the radius of curvature of the prime vertical,

with a and e being the semi-major axis and eccentricity of the reference ellipsoid,

$\Delta\varphi_i = \varphi_i - \varphi_{i-1}$ is the change in latitude between two consecutive points in the profile,

$\Delta\lambda_i = \lambda_i - \lambda_{i-1}$ is the change in longitude between two consecutive points in the profile,

$\delta g_N = \frac{\delta g_{N,i-1} + \delta g_{N,i}}{2}$ is the mean north gravity disturbance between two consecutive points in the profile, and

$\delta g_E = \frac{\delta g_{E,i-1} + \delta g_{E,i}}{2}$ is the mean east gravity disturbance between two consecutive points in the profile.

Once the disturbing potential is computed we make use of the downward continuation from the flight height to the terrain, and then apply the corrections for the determination of the geoid by either using Helmert's condensation method or by the application of the orthometric correction as described in sections 2.4, equation (2.7); see also Figure 2.2.

3.5 Numerical aspect for LSC

Let us focus first on the way the matrices in equation (2.10), resp. (2.11) are formed. For the case of predicting the disturbing potential from the components of the gravity disturbance vector, we can write explicitly the elements involved in the computation of the disturbing potential as follows:

$$s_{(n,1)} = \begin{bmatrix} T_1 \\ T_2 \\ T_3 \\ \vdots \\ T_n \end{bmatrix}, \text{ Vector of disturbing potential values (to be predicted),}$$

$$y_{(3n,1)} = \begin{bmatrix} T_{x_1} \\ T_{y_1} \\ -T_{z_1} \\ T_{x_2} \\ T_{y_2} \\ -T_{z_2} \\ \vdots \\ -T_{z_n} \end{bmatrix}, \text{ Vector of observations where } T_x = \delta g_N, T_y = \delta g_E, -T_z = \delta g_D,$$

$$C_{st(n,3n)} = \begin{bmatrix} C(T_1, T_{x_1}) & C(T_1, T_{y_1}) & C(T_1, -T_{z_1}) & C(T_1, T_{x_2}) & C(T_1, T_{y_2}) & C(T_1, -T_{z_2}) & \cdots & C(T_1, -T_{z_n}) \\ C(T_2, T_{x_1}) & C(T_2, T_{y_1}) & C(T_2, -T_{z_1}) & C(T_2, T_{x_2}) & C(T_2, T_{y_2}) & C(T_2, -T_{z_2}) & \cdots & C(T_2, -T_{z_n}) \\ C(T_3, T_{x_1}) & C(T_3, T_{y_1}) & C(T_3, -T_{z_1}) & C(T_3, T_{x_2}) & C(T_3, T_{y_2}) & C(T_3, -T_{z_2}) & \cdots & C(T_3, -T_{z_n}) \\ \vdots & \vdots & \vdots & \vdots & \vdots & \vdots & \ddots & \vdots \\ C(T_n, T_{x_1}) & C(T_n, T_{y_1}) & C(T_n, -T_{z_1}) & C(T_n, T_{x_2}) & C(T_n, T_{y_2}) & C(T_n, -T_{z_2}) & \cdots & C(T_n, -T_{z_n}) \end{bmatrix}$$

$$C_{tt(3n,3n)} = \begin{bmatrix} C(T_{x_1}, T_{x_1}) & C(T_{x_1}, T_{y_1}) & C(T_{x_1}, -T_{z_1}) & C(T_{x_1}, T_{x_2}) & C(T_{x_1}, T_{y_2}) & C(T_{x_1}, -T_{z_2}) & \cdots & C(T_{x_1}, -T_{z_n}) \\ C(T_{y_1}, T_{x_1}) & C(T_{y_1}, T_{y_1}) & C(T_{y_1}, -T_{z_1}) & C(T_{y_1}, T_{x_2}) & C(T_{y_1}, T_{y_2}) & C(T_{y_1}, -T_{z_2}) & \cdots & C(T_{y_1}, -T_{z_n}) \\ C(-T_{z_1}, T_{x_1}) & C(-T_{z_1}, T_{y_1}) & C(-T_{z_1}, -T_{z_1}) & C(-T_{z_1}, T_{x_2}) & C(-T_{z_1}, T_{y_2}) & C(-T_{z_1}, -T_{z_2}) & \cdots & C(-T_{z_1}, -T_{z_n}) \\ C(T_{x_2}, T_{x_1}) & C(T_{x_2}, T_{y_1}) & C(T_{x_2}, -T_{z_1}) & C(T_{x_2}, T_{x_2}) & C(T_{x_2}, T_{y_2}) & C(T_{x_2}, -T_{z_2}) & \cdots & C(T_{x_2}, -T_{z_n}) \\ C(T_{y_2}, T_{x_1}) & C(T_{y_2}, T_{y_1}) & C(T_{y_2}, -T_{z_1}) & C(T_{y_2}, T_{x_2}) & C(T_{y_2}, T_{y_2}) & C(T_{y_2}, -T_{z_2}) & \cdots & C(T_{y_2}, -T_{z_n}) \\ C(-T_{z_2}, T_{x_1}) & C(-T_{z_2}, T_{y_1}) & C(-T_{z_2}, -T_{z_1}) & C(-T_{z_2}, T_{x_2}) & C(-T_{z_2}, T_{y_2}) & C(-T_{z_2}, -T_{z_2}) & \cdots & C(-T_{z_2}, -T_{z_n}) \\ \vdots & \vdots & \vdots & \vdots & \vdots & \vdots & \ddots & \vdots \\ C(-T_{z_n}, T_{x_1}) & C(-T_{z_n}, T_{y_1}) & C(-T_{z_n}, -T_{z_1}) & C(-T_{z_n}, T_{x_2}) & C(-T_{z_n}, T_{y_2}) & C(-T_{z_n}, -T_{z_2}) & \cdots & C(-T_{z_n}, -T_{z_n}) \end{bmatrix}$$

$$D_{ee(3n,3n)} = \text{diag}[\sigma_{T_{x_1}}^2 \quad \sigma_{T_{y_1}}^2 \quad \sigma_{T_{z_1}}^2 \quad \sigma_{T_{x_2}}^2 \quad \sigma_{T_{y_2}}^2 \quad \sigma_{T_{z_2}}^2 \quad \cdots \quad \sigma_{T_{z_n}}^2].$$

For the covariance of the noise (D_{ee}) we assume no correlation. We do not know the correlations because of the way the different components of the gravity disturbance vector are computed (see Section 4.2.2).

As it has already been mentioned the results of LSC are highly dependent on the right choice of the covariance function. Since our data are only given in local areas, local

covariance functions are used. A particular reciprocal distance model of a local covariance function, being stationary and positive definite, is given by (Jekeli, 2003):

$$K(d_1, d_2, z_P + z_Q) = \sum_{j=1}^M \frac{\sigma_j^2}{[(1 + \alpha_j(z_P + z_Q))^2 + \alpha_j^2(d_1^2 + d_2^2)]^{\frac{1}{2}}} \quad (3.16)$$

with $d_1 = x_P - x_Q$, and $d_2 = y_P - y_Q$

The parameters σ_j^2 , M and α_j have to be determined empirically based on the local behavior of the disturbing potential. Notice that this is an isotropic model, since it depends only on the distance between two points and not on the direction of points with respect to each other.

In order to compute the parameters we will use some of the spectral relationships for the covariance function. A special characteristic of the covariance function as in (3.16) is that it has a known power spectral density (PSD), from where by comparison with the PSD computed with data of the disturbing potential in the area of interest, the value of the parameters can be determined. These data can be obtained from a previous local model, or from any another available source. The spectral representation of equation (3.16), i.e. its Fourier transform, is given by (Jekeli, 2003):

$$\Phi(u, v; z_P + z_Q) = \sum_{j=1}^M \frac{\sigma_j^2 e^{-2\pi\sqrt{u^2+v^2}(1/\alpha_j+(z_P+z_Q))}}{\alpha_j\sqrt{u^2+v^2}} \quad (3.17)$$

with u and v the cyclical frequencies in the spectral domain.

Another way to get the parameters for the covariance function is to first compute empirical covariance values in the data domain; and in our case, according to equation (3.16), determine an isotropic model by varying the parameters until a good fit to this model is achieved. We can take advantage of the properties of the Fourier transform and compute first the PSD of our data and then its inverse to obtain the respective covariance function. For the case of discrete and limited data, an estimate for the PSD is given by (Jekeli, 2001):

$$\hat{\Phi}_{gh}(u, v) = \frac{1}{n\Delta x m\Delta y} G^*(u, v) H(u, v) \quad (3.18)$$

with $G^*(u, v)$ the complex conjugate of the **DFT** $[g(x, y)]$, $H(u, v)$ the **DFT** $[h(x, y)]$, $g(x, y)$ and $h(x, y)$ the functions in the space domain for whose covariance functions we are interested in computing the PSD, m and n are the number of points in the x and y directions respectively, Δx and Δy the respective grid spacing of the data, and u and v the respective cyclic frequencies in the spectral domain. For the case of the auto-covariance function we have $g(x, y) = h(x, y)$.

Once we have estimated the PSD of the data, we need to get an estimation of the covariance function of the data by computing the inverse DFT of the estimated PSD as:

$$\hat{c}_{gh}(x, y) = \mathbf{DFT}^{-1}[\hat{\Phi}_{gh}(u, v)] . \quad (3.19)$$

Now, we need to compute an isotropic function to be fitted to our covariance model as given by equation (3.16). This new function can be computed as the average over circles of constant radius from the estimated covariance as (Jekeli, 2001):

$$\hat{c}_{gh}(m \Delta r) = \frac{1}{M_m} \sum_{\substack{m_1, m_2 \\ m = \sqrt{m_1^2 + m_2^2}}} \hat{c}_{gh}(m_1 \Delta x, m_2 \Delta y) \quad (3.20)$$

with $\hat{c}_{gh}(m \Delta r)$ the estimated isotropic covariance derived from the data, and M_m the total number of averaged covariance estimates per radial lag, $m \Delta r$.

The analytical covariance function is found by fitting it to the empirical values, expressed by equation (3.20), by varying the parameters α_j and σ_j^2 .

Since, in general we do not know the true mean of the data we cannot compute the covariance function for the least squares collocation adjustment. Instead we can use the homeogram function and compute the predicted potential as (Schaffrin, 2001):

$$\tilde{\mathbf{s}} = \tilde{\chi}^T \mathbf{y} , \quad (3.21)$$

and for the mean square error of the predicted signal (Schaffrin, 2001):

$$\text{diag}[C_{\tilde{s}\tilde{s}}] = \text{diag}[R_{ss}] - \text{diag}[\tilde{\chi}^T R_{ts}] + \tilde{\mathbf{v}} , \quad (3.22)$$

where R_{ss} the homeogram for signal (compare to C_{ss} in equation (2.11)),

R_{ts} the cross-homeogram for the signal (compare to C_{st} in equation (2.11)), and $\tilde{\chi}$ and $\tilde{\mathbf{v}}$ are computed by solving the following system of equations (Schaffrin, 2001):

$$\begin{bmatrix} R_{yy} & -\boldsymbol{\tau} \\ -\boldsymbol{\tau}^T & 0 \end{bmatrix} \begin{bmatrix} \tilde{\chi} \\ \tilde{\mathbf{v}} \end{bmatrix} = \begin{bmatrix} R_{ts} \\ -\boldsymbol{\tau}^T \end{bmatrix} , \quad (3.23)$$

where $R_{yy} = R_{tt} + D_{ee}$, and

$$\boldsymbol{\tau} = [1 \ 1 \ 1 \ \dots \ 1]^T .$$

Notice that equation (3.22) does not provide an estimate for the off-diagonal elements of the estimated covariance (based on the homeogram) for the predicted signal.

3.6 Numerical treatment for the downward continuation

In this part, the numerical implementation of the downward continuation of a harmonic function is explained. Also a test is performed to examine the accuracy of the gradient and the iterative methods. The inversion method is not included since it would require that a suitable regularization parameter be determined. The solution would depend strongly on the estimated regularization parameter, and this parameter depends on the characteristics of a particular problem, and the data collected. Recently, Schaffrin et al., 2003 introduce an “optimal” estimation of the regularization parameter. The use of this optimal estimation should be examined in future studies.

3.6.1 The gradient method

The gradient formula for continuation of harmonic functions for discrete data can be written according to equation (2.24) as:

$$\left. \frac{\partial T}{\partial r} \right|_{r=R} = -\frac{T_p}{R} + \frac{R^2 \Delta \varphi \Delta \lambda}{2\pi} \sum_{\varphi_i = \varphi_1}^{\varphi_n} \sum_{\lambda_j = \lambda_1}^{\lambda_m} \frac{T - T_p}{l_o^3} \cos \varphi_i \quad (3.24)$$

with n the number of parallels, and m the number of meridians in the grid.

Equation (3.24) presents singularities at the origin for the kernel function $\frac{1}{l_o^3}$. By means of the discretization of equation (3.24) we can avoid the singularity since this equation can be written as (See Jekeli, 2001):

$$\left. \frac{\partial T}{\partial r} \right|_{r=R} = -\frac{T_p}{R} + \frac{R^2 \Delta \varphi \Delta \lambda}{2\pi} \left[\sum_{\substack{\varphi_i = \varphi_2 \\ \varphi_i \neq \varphi_1}}^{\varphi_n} \sum_{\substack{\lambda_j = \lambda_2 \\ \lambda_j \neq \lambda_1}}^{\lambda_m} \frac{T - T_p}{l_o^3} \cos \varphi_i + \frac{[T]_{\varphi_1, \lambda_1}}{(l_o^3)_0} \cos \varphi_i - \frac{[T_p]_{\varphi_1, \lambda_1}}{(l_o^3)_0} \cos \varphi_i \right],$$

where $\left(\frac{1}{l_o^3} \right)_0$ is the kernel at the origin, theoretically $\rightarrow \infty$.

However, we can see that this equation does not depend on the kernel at the origin since $[T]_{\varphi_1, \lambda_1} = [T_p]_{\varphi_1, \lambda_1}$.

For a more rigorous, but rarely applied correction for the contribution of the innermost zone the reader is referred to Jekeli (2001, pp.4.10), and Heiskanen and Moritz (1967, pp.121-122).

Equation (3.24) can be written as:

$$\left. \frac{\partial T}{\partial r} \right|_{r=R} = -\frac{T_p}{R} + \frac{R^2 \Delta \phi \Delta \lambda}{2\pi} [T * f - T_p g] \quad (3.25)$$

$$\text{with: } f = \frac{\cos \phi_i}{l_o^3}, \text{ and } g = \sum_{\phi_i=\phi_1}^{\phi_n} \sum_{\lambda_j=\lambda_1}^{\lambda_m} \frac{\cos \phi_i}{l_o^3}$$

$$\text{where } l_o = 2R \sin\left(\frac{\psi}{2}\right).$$

The second term of equation (3.24) is an approximate convolution in T and f, and could be evaluated, via 1D-FFT, similar to the evaluation for Hotine's integral in section 3.3.

The downward continued disturbing potential is written as:

$$T^* = T - \frac{\partial T}{\partial r} H$$

where T^* is the downward continued field,

T is the original field,

H is the height at which T is given and at which $\frac{\partial T}{\partial r}$ is evaluated.

We can also write equation (3.24) in planar approximation as:

$$\frac{\partial T}{\partial h} = \frac{\Delta x \Delta y}{2\pi} \sum_{i=1}^N \sum_{j=1}^M \frac{T - T_p}{d_{ij}^3} \quad (3.26)$$

with M and N the number of points in x and y directions

$$\Delta x \cong R \Delta \phi,$$

$$\Delta y \cong R \Delta \lambda \cos \phi_m,$$

ϕ_m the mean latitude in the area of computation, and

$$d_{ij} = \sqrt{(x_j - x_p)^2 + (y_i - y_p)^2}.$$

Now equation (3.26) can be written as:

$$\frac{\partial T}{\partial h} = \frac{\Delta x \Delta y}{2\pi} [T * f - T_p g] \quad (3.27)$$

$$\text{with: } f = \frac{1}{d_{ij}^3}, \text{ and } g = \sum_{i=1}^N \sum_{j=1}^M \frac{1}{d_{ij}^3}.$$

The convolution can be computed via a 2D-FFT as:

$$\frac{\partial T}{\partial h} = \frac{\Delta x \Delta y}{2\pi} \{ \mathbf{DFT}^{-1} [\mathbf{DFT}(T) \mathbf{DFT}(f)] - T_p g \} \quad (3.28)$$

The values for the downward continued disturbance potential are now computed as:

$$T^* = T - \frac{\partial T}{\partial h} H .$$

3.6.2 The iterative solution of Poisson's integral

For the case of the iterative Poisson's solution we write equation (2.31) in discrete form as:

$$T_p^* = \frac{T_p}{t} - \frac{(1-t^2)\Delta\varphi\Delta\lambda}{4\pi} \sum_{\varphi_p=\varphi_1}^{\varphi_n} \sum_{\lambda_p=\lambda_1}^{\lambda_m} \frac{T^* - T_p^*}{D^3} \cos\varphi_p . \quad (3.29)$$

Notice that the second term in equation (3.29) is an approximate convolution. It depends on φ , λ and h_p , and cannot be evaluated via FFT, unless we consider a constant height. For the case of airborne data we can consider the height almost constant and evaluate equation (3.29) as convolution by using a similar procedure to the numerical implementation of Hotine's integral where 1D-FFT is used along the parallels and summation along the meridians. Equation (3.29) has to be iterated until the maximum difference in the area of computation between two consecutive solutions is not larger than a chosen threshold.

For the case of the planar approximation and assuming constant height, the downward continuation can be computed by the use of 2D-FFT. We can write the planar approximation for the iterative formula (equation (2.32)) for the discrete case as:

$$T_p^* \approx T_p - \frac{H\Delta x\Delta y}{2\pi} \sum_{i=1}^N \sum_{j=1}^M \frac{T^* - T_p^*}{l_{ij}^3} \quad (3.30)$$

with M and N the number of points in x and y directions,

$$\Delta x \cong R \Delta\varphi,$$

$$\Delta y \cong R \Delta\lambda \cos \varphi_m,$$

φ_m the mean latitude in the area of computation,

$$l_{ij} = \sqrt{(x_i - x_p)^2 + (y_i - y_p)^2 + H^2} ,$$

H the height where the original field is located .

Now equation (3.30) can be written as:

$$T_p^* = T_p - \frac{H\Delta x\Delta y}{2\pi} [T^* * f - T_p^* g] \quad (3.31)$$

with: $f = \frac{1}{l^3}$, and $g = \sum_{i=1}^N \sum_{j=1}^M \frac{1}{l^3}$

Each iteration of equation (3.31) can now be computed by the use of the 2D-FFT as:

$$T_p^* = T_p - \frac{H\Delta x\Delta y}{2\pi} \{ \mathbf{DFT}^{-1}[\mathbf{DFT}(T^*)\mathbf{DFT}(f)] - T_p^*g \} . \quad (3.32)$$

Again the iterations are stopped when a given threshold for the maximum difference between two consecutive solutions is reached.

3.6.3 Test results

For the evaluation of the gradient and the iterative solutions of Poisson's integral for the downward continuation, a test area in the Canadian Rocky Mountains is chosen. The test area and the height used are consistent with the area and flight height of the collected data that will be used later on. The data for the test are located in an area between latitudes 50° 09' and 51° 26', and longitudes from 243° 09' to 245° 08' on a 1' by 1' grid. The disturbing potential at geoid level is computed from the Geoid99 (GSSS99) model obtained from NGS (Smith and Roman, (2001)). Then the disturbing potential is computed at a height of 4630 m by using the upward continuation equation (2.22) in planar approximation. Finally the disturbing potential at this altitude is downward continued by the use of the iterative and gradient formulas in planar approximation and it is compared to the original field. Before the comparison, a strip of 20' around the area of computation is removed from the results to diminish edge effects. In Figure 3.1 the original and the upward continued fields are presented. Both solutions for the downward continuation can also be observed. Statistics for the original and upward continued disturbing potential are presented in Table 3.1, and statistics for the differences of the downward continuation with respect to the original field in Table 3.2.

	Mean [m ² /s ²]	Std dev ±[m ² /s ²]	Min [m ² /s ²]	Max [m ² /s ²]
(a) Original field	-136.270	9.389	-151.262	-123.033
(b) Upward continued field	-136.831	7.686	-148.586	-125.938
(a)-(b)	0.561	1.773	-2.914	3.437

Table 3.1: Statistics for the original and upward continued gravity disturbances

Differences of original field with respect to	Mean [m ² /s ²]	Std dev ±[m ² /s ²]	Min [m ² /s ²]	Max [m ² /s ²]
Down cont (gradient method)	0.603	0.476	-0.740	2.162
Down cont (iterative method)	-0.093	0.238	-0.881	0.572

Table 3.2: Statistics for the differences of the gradient and iterative solution for the downward continuation with respect to the original disturbing potential

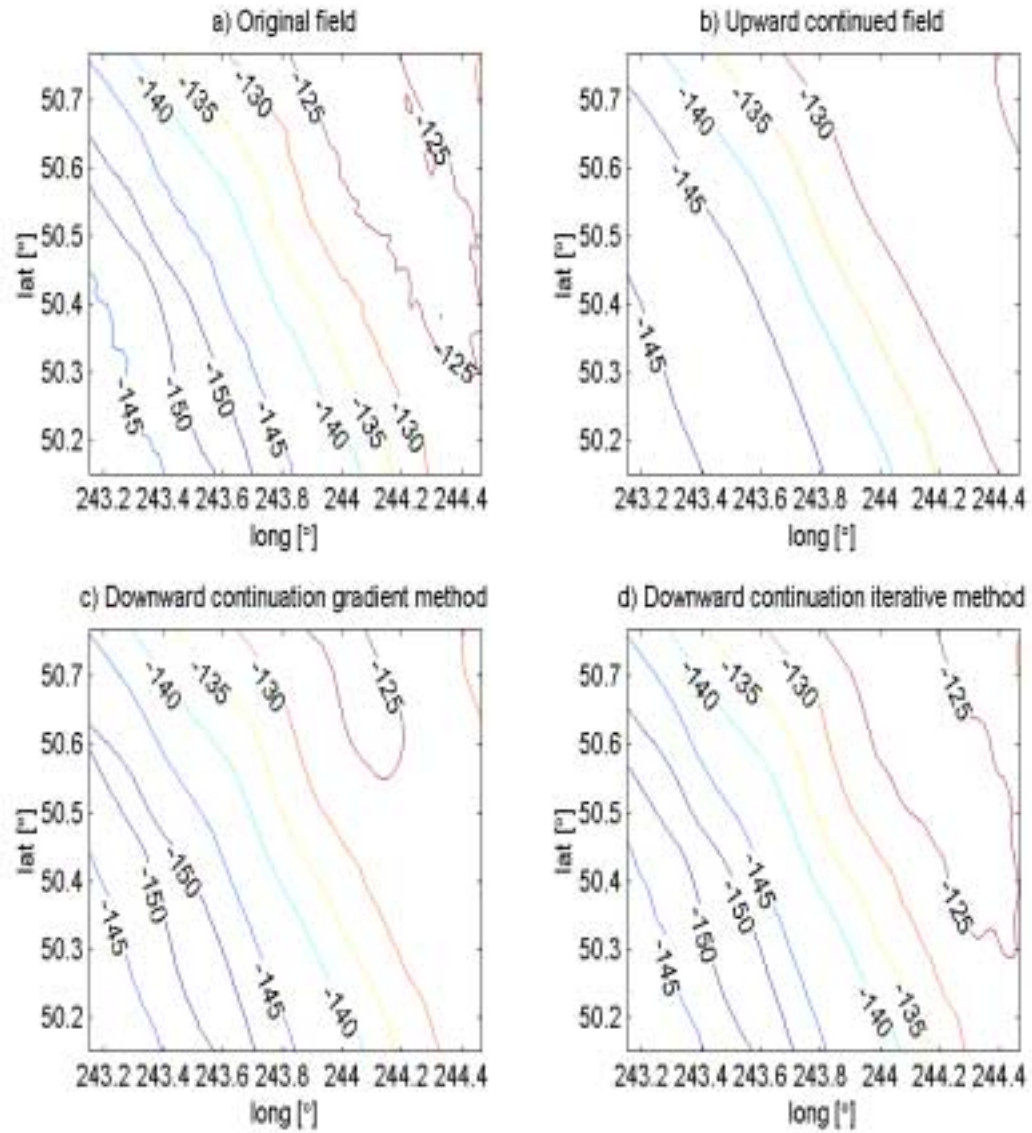


Figure 3.1: Original and upward continued field (a), (b), and the downward continuation solution using the gradient method (c) and Poisson's iterative solution (d). Units of the contour lines are $[m^2/s^2]$.

We can observe that the iterative solution for the downward continuation of the disturbing potential provides better results than the application of the gradient method. This can be observed not only from the statistics of the differences but also by visually inspecting the results. We can observe how Figure 3.1 (d) better describes the original field, as opposed to Figure 3.2 (c).

CHAPTER 4

AIRBORNE GRAVIMETRY

4.1 Introduction

As mentioned in Chapter 1, there are areas in the world where data of gravity do not exist or are insufficient for a reliable computation of the geoid. The densification of terrestrial gravity networks is a very expensive task. One option is the use of airborne gravimetry in order to minimize the time and resources in the establishment of gravimetric networks. Many studies have been done in the past regarding the processing of this kind of data. Here we will focus on the computations of the gravity vector as proposed by Jekeli and Kwon (1999) where the vector of gravity disturbances is computed in the inertial frame and then transformed to the local frame for the respective use in the computation of the geoid. This method is chosen since, opposed to the traditional approach, the three components of the gravity disturbance vector can be determined at once. In the traditional approach the gravity disturbance components are obtained via the errors associated with inertial positioning (Jekeli, 2000, p.323), and the vertical component of the gravity disturbance vector cannot be obtained, since the integration of inertial accelerations is not stable when done in the vertical (Jekeli, 1998b).

In this chapter also the cross-over adjustment of the computed gravity disturbance vector is examined. An introduction to the basic model for cross-over computations is described. Also, the computation of the gravity disturbance vector in a test area in the Canadian Rocky Mountains is done. These results will be used for the determination of the geoid in the next chapter.

4.2 Gravity disturbance determination

The basic relationship in an inertial frame for airborne gravimetry comes from Newton's second law of motion:

$$\ddot{\mathbf{x}}^i = \mathbf{a}^i + \mathbf{g}^i \quad (4.1)$$

where \mathbf{a}^i is the specific force sensed by the accelerometers in the inertial frame, and $\ddot{\mathbf{x}}^i$ is the kinematic acceleration in inertial space, computed and transformed from precise positions, generally obtained by GPS receivers on board the plane. Kwon (2000) proposes to determine the components of the gravity disturbance directly in the inertial frame and then rotate the vector to the local frame.

4.2.1 Accelerations in the inertial frame

GPS receivers provide position coordinates of latitude, longitude and ellipsoidal heights or their equivalent X, Y and Z in an earth fixed system. In order to get the

kinematic accelerations in an inertial frame the Cartesian coordinates X, Y and Z are transformed into an inertial frame. This inertial frame can be chosen arbitrarily by fixing a particular epoch:

$$\mathbf{x}^i = \mathbf{C}_e^i \mathbf{x}^e \quad (4.2)$$

with:

$$\mathbf{C}_e^i = \begin{bmatrix} \cos\omega_e(t-t_0) & -\sin\omega_e(t-t_0) & 0 \\ \sin\omega_e(t-t_0) & \cos\omega_e(t-t_0) & 0 \\ 0 & 0 & 1 \end{bmatrix}, \quad \mathbf{x}^i = \begin{bmatrix} X^i \\ Y^i \\ Z^i \end{bmatrix}, \text{ and } \mathbf{x}^e = \begin{bmatrix} X^e \\ Y^e \\ Z^e \end{bmatrix}$$

ω_e represents the Earth's rate of rotation, t the epoch of observation, and t_0 the arbitrary epoch to which the inertial frame is referred.

Once the Cartesian coordinates are in the inertial frame the acceleration can be obtained by differentiation of the coordinates twice with respect to time.

$$\ddot{\mathbf{x}}^i = \frac{\partial^2 \mathbf{x}^i}{\partial t^2} \quad (4.3)$$

which can be done by numerical integration techniques.

For the case of the specific force the procedure is more elaborate. We need the information provided by a set of gyros and accelerometers (IMU's, inertial measurement units) of an inertial navigation system (INS). The gyros provide information in the form of angular increments in the body frame as a function of time ($\delta\theta$), and the accelerometers the rate of change in velocity (δv).

By using the information provided by the accelerometers (delta-velocity) we have access to the respective acceleration according to the following relation (Jekeli, 2000, p.135):

$$\delta \mathbf{v}_l = \int_{\delta t} \mathbf{a}^s(t) dt \quad (4.4)$$

with \mathbf{a}^s the accelerations in the sensor frame

For the case of the angular increments provided by the gyros we can write:

$$\delta \boldsymbol{\theta}_l = \int_{\delta t} \boldsymbol{\omega}_{ib}^b(t) dt \quad (4.5)$$

where $\boldsymbol{\omega}_{ib}^b$ represents the vector of angular rates of the body frame with respect to inertial frame, described in the body frame.

The transformation from sensor to inertial frame can be obtained by integrating the differential equation:

$$\dot{C}_s^i = C_s^i \Omega_{is}^s \quad (4.6)$$

where: $\Omega_{is}^s = [\omega_{is}^s] \times = \begin{bmatrix} 0 & -\omega_3 & \omega_2 \\ \omega_3 & 0 & -\omega_1 \\ -\omega_2 & \omega_1 & 0 \end{bmatrix}$.

Equation (4.6) is generally solved by an equivalent expression in the form of quaternions as:

$$\dot{\mathbf{q}} = \frac{1}{2} \mathbf{A} \mathbf{q} \quad (4.5)$$

where $\mathbf{A} = \begin{bmatrix} 0 & \omega_1 & \omega_2 & \omega_3 \\ -\omega_1 & 0 & \omega_3 & -\omega_2 \\ -\omega_2 & -\omega_3 & 0 & \omega_1 \\ -\omega_3 & \omega_2 & -\omega_1 & 0 \end{bmatrix}$, and $\mathbf{q} = \begin{bmatrix} a \\ b \\ c \\ d \end{bmatrix}$.

This expression can be solved by numerical integration. The elements for the transformation matrix can now be formed from the quaternion vector as:

$$C_i^s = \begin{bmatrix} a^2 + b^2 - c^2 - d^2 & 2(bc + da) & 2(bd - ca) \\ 2(bc - da) & a^2 + c^2 - b^2 - d^2 & 2(cd + ab) \\ 2(bd + ca) & 2(cd - ab) & a^2 + d^2 - b^2 - c^2 \end{bmatrix} \quad (4.7)$$

For a detailed development of the numerical solutions for the described equations the reader is referred to Jekeli (2000), and Kwon (2000).

4.2.2 Improving the determination of the gravity vector by Kalman filter algorithm

Now we want to set up a linear dynamic system to obtain the gravity disturbance vector. As mentioned in the introduction the approach followed by Kwon (2000) will be used. An introduction to the basic relations is given next. We can first write equation (4.1) in terms of the observed quantities as:

$$\ddot{\tilde{\mathbf{x}}}^i - \delta \ddot{\mathbf{x}}^i = \ddot{\tilde{\mathbf{a}}}^i - \delta \mathbf{a}^i + \mathbf{g}^i \quad (4.8)$$

where $\ddot{\tilde{\mathbf{x}}}^i, \ddot{\tilde{\mathbf{a}}}^i$ are the observed accelerations in the inertial frame and $\delta \ddot{\mathbf{x}}^i, \delta \mathbf{a}^i$ their respective observational errors.

For the error in the accelerations we can write:

$$\delta \mathbf{a}^i = C_b^i \delta \mathbf{a}^b + \tilde{\mathbf{a}}^i \times \boldsymbol{\psi}^i \quad (4.9)$$

$$\delta \ddot{\mathbf{x}}^i = \boldsymbol{\varepsilon}_G \quad (4.10)$$

with $\delta \mathbf{a}^b$ the corresponding sensor error in the body frame,

$$\boldsymbol{\psi}^i = \begin{bmatrix} \psi_1^i \\ \psi_2^i \\ \psi_3^i \end{bmatrix}, \text{ the vector of orientation errors,}$$

C_b^i the transformation matrix from body to inertial frame , and

$\boldsymbol{\varepsilon}_G$ the error in the kinematic acceleration considered as random white noise.

Also for the accelerometer and gyro errors in the body frame we can write:

$$\delta \mathbf{b}_a = \mathbf{b}_a + \mathbf{k}_a \mathbf{a}^b + \boldsymbol{\varepsilon}_a \quad (4.11)$$

$$\delta \boldsymbol{\omega}_{ib}^b = \mathbf{b}_g + \mathbf{k}_g \boldsymbol{\omega}_{ib}^b + \boldsymbol{\varepsilon}_g \quad (4.12)$$

where \mathbf{b} stands for the respective biases, \mathbf{k} for the scale factor errors, and $\boldsymbol{\varepsilon}$ for random white noise. \mathbf{b} and \mathbf{k} are assumed to be random constants.

We also need the dynamic equations for the orientation error. In the inertial frame these are given by (Jekeli, 2000, p.151):

$$\dot{\boldsymbol{\psi}}^i = -C_b^i \delta \boldsymbol{\omega}_{ib}^b. \quad (4.13)$$

With equation (4.13) and (4.12) we can write the dynamic equation for the orientation errors as:

$$\dot{\boldsymbol{\psi}}^i = -C_b^i \mathbf{b}_g - C_b^i [\boldsymbol{\omega}_{ib}^b] \mathbf{k}_g - C_b^i \boldsymbol{\varepsilon}_g \quad (4.14)$$

With equations (4.11), (4.12) and (4.14) we arrive at the dynamic equation for the error parameters associated to the INS:

$$\dot{\mathbf{x}} = \mathbf{F}\mathbf{x} + \mathbf{G}\mathbf{w} = \quad (4.15)$$

$$= \begin{bmatrix} \dot{\mathbf{b}}_a \\ \dot{\mathbf{b}}_g \\ \dot{\mathbf{k}}_a \\ \dot{\mathbf{k}}_g \\ \dot{\boldsymbol{\psi}} \end{bmatrix} = \begin{bmatrix} 0 & 0 & 0 & 0 & 0 \\ 0 & 0 & 0 & 0 & 0 \\ 0 & 0 & 0 & 0 & 0 \\ 0 & 0 & 0 & 0 & 0 \\ 0 & -C_b^i & 0 & -C_b^i [\boldsymbol{\omega}_{ib}^b] & 0 \end{bmatrix} \begin{bmatrix} \mathbf{b}_a \\ \mathbf{b}_g \\ \mathbf{k}_a \\ \mathbf{k}_g \\ \boldsymbol{\psi} \end{bmatrix} + \begin{bmatrix} 0 & 0 & 0 & 0 & 0 \\ 0 & 0 & 0 & 0 & 0 \\ 0 & 0 & 0 & 0 & 0 \\ 0 & 0 & 0 & 0 & 0 \\ 0 & 0 & 0 & 0 & -C_b^i \end{bmatrix} \begin{bmatrix} 0 \\ 0 \\ 0 \\ 0 \\ \boldsymbol{\varepsilon}_g \end{bmatrix}$$

After decomposing the gravity vector as the sum of normal gravity vector plus the gravity disturbance vector ($\mathbf{g}^i = \boldsymbol{\gamma}^i + \boldsymbol{\delta g}^i$) we can finally write equation (4.8) as (Kwon, 2000):

$$\tilde{\mathbf{x}}^i - \tilde{\mathbf{a}}^i - \boldsymbol{\gamma}^i = -\mathbf{C}_b^i \mathbf{b}_a - \mathbf{C}_b^i [\tilde{\mathbf{a}}^b] \mathbf{k}_a - \tilde{\mathbf{a}}^i \times \boldsymbol{\psi}^i - \mathbf{C}_b^i \boldsymbol{\varepsilon}_a + \boldsymbol{\delta \ddot{x}}^i + \boldsymbol{\delta g}^i \quad (4.16)$$

where $[\tilde{\mathbf{a}}^b]$ is a diagonal matrix containing the elements of the observed accelerations in the body frame.

If we would like to estimate the gravity disturbance vector we need to provide a model for doing so. The appropriate modeling of the disturbing gravity field is nowadays controversial, and Kwon (2000) suggests the exclusion of the gravity disturbance vector in the observation model, thus committing a model error. This implies that the gravity disturbance vector will be reflected in the residual vector after the update in the Kalman filter adjustment. Schaffrin and Kwon (2002) introduced an alternative procedure where the disturbing potential is modeled as random system biases, and they claim to have improved results. Based on the procedure developed by Kwon (2000) we proceed to set up the Kalman filter observation equations:

$$\begin{aligned} \mathbf{y}_k - \boldsymbol{\delta g}^i &= \mathbf{H} \mathbf{x}_k + \mathbf{e}_k, \quad \mathbf{e}_k \sim (0, \mathbf{R}_k) \\ \mathbf{x}_k &= \Phi_{k-1} \mathbf{x}_{k-1} + \mathbf{G}_k \mathbf{w}_k, \quad \mathbf{w}_k \sim (0, \mathbf{Q}_k), \quad \mathbf{C}\{\mathbf{w}_k, \mathbf{e}_k\} = 0, \end{aligned}$$

with :

$$\begin{aligned} \mathbf{y} &= \tilde{\mathbf{x}}^i - \tilde{\mathbf{a}}^i - \boldsymbol{\gamma}^i, \\ \mathbf{H} &= \begin{pmatrix} -\mathbf{C}_b^i & \mathbf{0}_{3 \times 3} & -[\tilde{\mathbf{a}}^i] \mathbf{C}_b^i & \mathbf{0}_{3 \times 3} & -[\tilde{\mathbf{a}}^i \times] \end{pmatrix}, \end{aligned}$$

Φ is the state transition matrix; under the assumption that \mathbf{F} is constant during the transition time it is computed as:

$$\Phi = e^{\mathbf{F}(t_k - t_{k-1})} = \mathbf{I} + \mathbf{F} \Delta t + \frac{1}{2!} (\mathbf{F} \Delta t)^2 + \frac{1}{3!} (\mathbf{F} \Delta t)^3 + \dots$$

\mathbf{G} , for this case, as in equation (4.15),

$$\mathbf{w}_k = \int_{t_{k-1}}^{t_k} \Phi(t, t') \mathbf{w}(t') dt' \quad (\text{see Jekeli, 2000, p.222}),$$

$$\mathbf{e} = (\mathbf{C}_b^i \boldsymbol{\varepsilon}_a + \boldsymbol{\delta \ddot{x}}^i).$$

For the adjusted observations as a function of the estimated parameters we can write according to Jekeli, (2000, p.332):

$$\hat{\mathbf{y}} = \mathbf{y} - \tilde{\mathbf{e}} = \mathbf{H} \hat{\mathbf{x}}$$

where $\hat{\mathbf{x}} = \mathbf{x} + \boldsymbol{\delta x}$, and $\boldsymbol{\delta x} = [\boldsymbol{\delta b}_a^T, \boldsymbol{\delta b}_g^T, \boldsymbol{\delta k}_a^T, \boldsymbol{\delta k}_g^T, \boldsymbol{\delta \psi}^T]^T$ are the true errors in the estimates.

Now for the residual vector of the adjusted observation with respect to the observed values we can write (Kwon and Jekeli, 2001):

$$\tilde{\mathbf{e}} = \mathbf{y} - \hat{\mathbf{y}}$$

$$= \delta \mathbf{g}^i + C_b^i \delta \mathbf{b}_a + C_b^i [\tilde{\mathbf{a}}^b] \delta \mathbf{k}_a + \tilde{\mathbf{a}}^i \times \delta \boldsymbol{\psi}^i + C_b^i \boldsymbol{\varepsilon}_a - \boldsymbol{\varepsilon}_G$$

under the assumption that the true errors in the estimates of the system and the noise of the inertial sensors and observed kinematic acceleration are small with respect to $\delta \mathbf{g}^i$, and random in character, the vector of the adjusted residuals ($\tilde{\boldsymbol{\varepsilon}}$) can be identified with the components of the sought gravity disturbance vector (Kwon, 2000; Jekeli, 2000), since it is not a state in the error dynamics system. One drawback of this method is that we do not have access to a direct estimate of the precision in the determination of the gravity vector.

Once an uncorrelated initial condition is introduced, the solution for this system is found by applying the Kalman filter algorithm. When an observation becomes available the system is updated and the states and covariance matrices are computed as:

$$\hat{\mathbf{x}}_k = \hat{\mathbf{x}}_k^- + \mathbf{K}_k (\mathbf{y}_k - \mathbf{H}_k \hat{\mathbf{x}}_k^-), \quad (4.17)$$

$$\mathbf{P}_k = (\mathbf{I} - \mathbf{K}_k \mathbf{H}_k) \mathbf{P}_k^- (\mathbf{I} - \mathbf{K}_k \mathbf{H}_k)^T + \mathbf{K}_k \mathbf{R}_k \mathbf{K}_k^T, \quad (4.18)$$

with \mathbf{K}_k the Kalman gain matrix, determined by:

$$\mathbf{K}_k = \mathbf{P}_k^- \mathbf{H}_k^T (\mathbf{H}_k \mathbf{P}_k^- \mathbf{H}_k^T + \mathbf{R}_k)^{-1}, \quad (4.19)$$

and

$$\hat{\mathbf{x}}_k^- = \Phi_{k-1} \hat{\mathbf{x}}_{k-1} \quad (4.20)$$

$$\mathbf{P}_k^- = \Phi_{k-1} \mathbf{P}_{k-1} \Phi_{k-1}^T + \mathbf{G}_k \mathbf{Q}_k \mathbf{G}_k^T \quad (4.21)$$

where the \mathbf{P} matrix represents the covariance matrix for the errors of the estimated states. The negative superscript is used to indicate that no observation has been added yet.

The implementation of equations (4.20) and (4.21) depends only on the transition matrix and the previous estimate at time t_{k-1} , as well as on the “system error” covariance matrix.

4.3 Cross-over adjustment

The estimates provided by the along track processing of the GPS-INS data need to be adjusted internally to make them self-consistent in the case that tracks cross each other. To do this we adjust the components of the gravity vector by a cross-over adjustment that minimizes the discrepancies at the crossing points. Another important consideration is to refer the adjusted self-consistent estimates to a particular datum. This means that we need control points with information about the gravity vector in the area of computations. A basic approach for the cross-over adjustment and the way to tie the lines to control points is presented next. In this part the procedure to make the set of lines self-

consistent within the area of interest is addressed in a least squares sense. The geometry of the flight lines is presented and a solution is introduced from basic relationships.

Suppose we have a set of lines in the N-S directions that are intersected by 2 lines in the E-W directions. As an example, let us call the two lines in the E-W directions line C1 and line C2, and the lines in the N-S direction line 1 to line n, as in Figure 4.1.

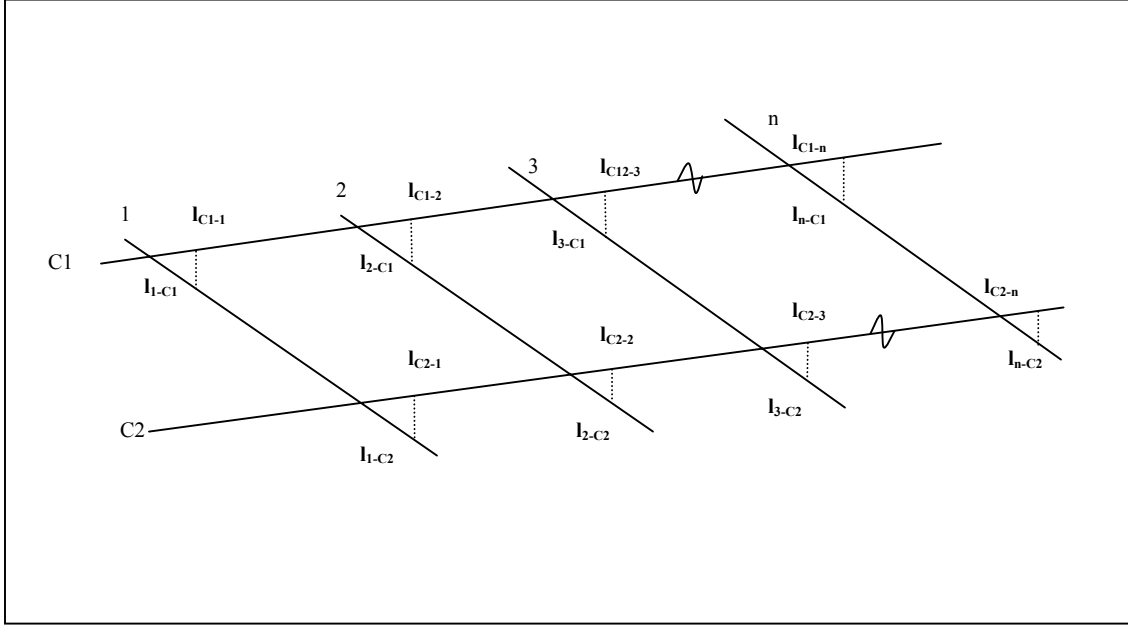


Figure 4.1: Schematic representation of cross-overs

At the intersections of those lines denote the true value of the particular gravity disturbance component by the capital letters, i.e. L_{C1-i} or L_{C2-i} , and the observed value by the small letters, i.e. l_{C1-i} or l_{C2-i} , with $i=1 \dots n$ in this case. At each intersection we will assume our observation biased from the true value in quantity b_i and with an additional slope m_i . The sub-indices $i-C1$ refer to quantities on the line i as it intercepts the line C1 and the sub-indices $C1-i$ refer to quantities on the line C1 as it intercepts the line i . Now for line C1 we can write a set of equations of the form:

$$\begin{aligned} l_{i-C1} &= L_{i-C1} + b_i + m_i(y_{i-C1} - y_{0i}) + e_{i-C1} \\ l_{C1-i} &= L_{C1-i} + b_{C1} + m_{C1}(x_{C1-i} - x_{0i}) + e_{C1-i} \end{aligned} \quad (4.22)$$

for the intersections of line i with line C1, and vice-versa. In this system of equations e_{i-C1} and e_{C1-i} represent the associated random errors with the observations at each crossing point. The variable x_i corresponds to the x coordinates and, y_i corresponds to the y coordinates (or east and north coordinates). The x_{0i} and y_{0i} represent the coordinates of the origin for each line. We could also use instead of the position coordinates time coordinates that can be taken from the epoch at which the observation is taken. If epochs

are used, the argument of the slopes will not change for lines in the north-south and east-west directions, and only an initial epoch needs to be used. In this study position coordinates will be used for convenience, since they will fit well for the case when a simulation is needed.

The units of the observations and the biases are units of the gravity disturbance vector, either m/s^2 or mGal . The units for the slopes will depend on the type of argument we use. For example if a time argument is used the units of the slopes will be mGal/sec , or if coordinates of latitude and longitude are used the units will be mGal/degree .

For the case of line C2 we have the same situation:

$$\begin{aligned} l_{i-C2} &= L_{i-C2} + b_i + m_i (y_{i-C2} - y_0) + e_{i-C2} \\ l_{C2-i} &= L_{C2-i} + b_{C2} + m_{C2} (x_{C2-i} - x_0) + e_{C2-i} \end{aligned} \quad (4.23)$$

Subtracting both equations in each set we have:

$$\begin{aligned} l_{1-C1} - l_{C1-1} &= b_1 + m_1(y_{1-C1} - y_0) - b_{C1} - m_{C1}(x_{C1-1} - x_0) + e_{1-C1, C1-1} \\ l_{2-C1} - l_{C1-2} &= b_2 + m_2(y_{2-C1} - y_0) - b_{C1} - m_{C1}(x_{C1-2} - x_0) + e_{2-C1, C1-2} \\ &\vdots \\ l_{n-C1} - l_{C1-n} &= b_n + m_n(y_{n-C1} - y_0) - b_{C1} - m_{C1}(x_{C1-n} - x_0) + e_{n-C1, C1-n} \\ \\ l_{1-C2} - l_{C2-1} &= b_1 + m_1(y_{1-C2} - y_0) - b_{C2} - m_{C2}(x_{C2-1} - x_0) + e_{1-C2, C2-1} \\ l_{2-C2} - l_{C2-2} &= b_2 + m_2(y_{2-C2} - y_0) - b_{C2} - m_{C2}(x_{C2-2} - x_0) + e_{2-C2, C2-2} \\ &\vdots \\ l_{n-C2} - l_{C2-n} &= b_n + m_n(y_{n-C2} - y_0) - b_{C2} - m_{C2}(x_{C2-n} - x_0) + e_{n-C2, C2-n} \end{aligned}$$

This system can now be written in matrix form as:

$$\boldsymbol{\omega} = \mathbf{B}\mathbf{y} = \mathbf{A}\boldsymbol{\xi} + \mathbf{B}\mathbf{e}$$

with:

$$\boldsymbol{\omega} = \begin{bmatrix} l_{1-C1} - l_{C1-2} \\ l_{2-C1} - l_{C1-2} \\ l_{3-C1} - l_{C1-3} \\ \vdots \\ l_{n-C2} - l_{C2-n} \end{bmatrix}_{(2n) \times 1} \quad \text{being the vector of observational differences,}$$

$$\mathbf{B} = [\mathbf{I}_{2n}, -\mathbf{I}_{2n}],$$

$$\mathbf{y} = \begin{bmatrix} l_{1-C1} \\ \dots \\ l_{n-C2} \\ l_{C1-1} \\ \dots \\ l_{C2-n} \end{bmatrix}_{(4n) \times 1},$$

$$\mathbf{e} = \begin{bmatrix} e_{1-C1} \\ \dots \\ e_{n-C2} \\ e_{C1-1} \\ \dots \\ e_{C2-n} \end{bmatrix}_{(4n) \times 1},$$

$$\mathbf{A} = \begin{bmatrix} 1 & 0 & \dots & 0 & -1 & 0 & y_{1-C1}-y_0 & 0 & \dots & 0 & -(x_{C11}-x_0) & 0 \\ 0 & 1 & \dots & 0 & -1 & 0 & 0 & y_{2-C1}-y_0 & \dots & 0 & -(x_{C12}-x_0) & 0 \\ \vdots & \vdots & & \vdots & \vdots & \vdots & \vdots & \vdots & & \vdots & \vdots & \vdots \\ 0 & 0 & \dots & 1 & -1 & 0 & 0 & 0 & \dots & y_{n-C1}-y_0 & -(x_{C1n}-x_0) & 0 \\ 1 & 0 & \dots & 0 & 0 & -1 & y_{1-C2}-y_0 & 0 & \dots & 0 & 0 & -(x_{C21}-x_0) \\ 0 & 1 & \dots & 0 & 0 & -1 & 0 & y_{2-C2}-y_0 & \dots & 0 & 0 & -(x_{C22}-x_0) \\ \vdots & \vdots & & \vdots & \vdots & \vdots & \vdots & \vdots & & \vdots & \vdots & \vdots \\ 0 & 0 & \dots & 1 & 0 & -1 & 0 & 0 & \dots & y_{n-C2}-y_0 & 0 & -(x_{C2n}-x_0) \end{bmatrix}_{(2n) \times (2n+4)}$$

being the design matrix relating the observations to the unknowns, and

$$\boldsymbol{\xi} = \begin{bmatrix} b_1 \\ b_2 \\ \vdots \\ b_n \\ b_{C1} \\ b_{C2} \\ m_1 \\ m_2 \\ \vdots \\ m_n \\ m_{C1} \\ m_{C2} \end{bmatrix}_{(2n+4) \times 1}$$

the vector of unknowns containing the desired parameters.

Notice that this system has rank deficiency. We could add another transversal line, say C3, but this would not provide the external information needed to overcome the datum defect. There will always be 2 biases and 2 trends that cannot be solved for. One option is to perform a free-adjustment that will provide a set of parameters that are consistent internally, which can later be referred to a particular “datum” by the use of external information coming from control points. The other solution is to introduce constraints to the system. This is not that different from the first approach but in this case the system is referred to a particular datum at once.

For the former case we can write the system as:

$$\boldsymbol{\omega} = \mathbf{B}\mathbf{y} = \mathbf{A}\boldsymbol{\xi} + \mathbf{B}\mathbf{e}, \quad \boldsymbol{\omega} \sim (\mathbf{A}\boldsymbol{\xi}, 2\sigma_0^2\mathbf{I}),$$

with dimension of the range space of A, $\Re(\mathbf{A}) = 2n < 2n+4$, and σ_0^2 the variance of the unit weight.

The free solution is given by MINOLESS (Minimal Norm LEast Squares Solution) as:

$$\begin{aligned} \hat{\boldsymbol{\xi}} &= (\mathbf{N} + \mathbf{E}^T \mathbf{E})^{-1} \mathbf{c} \\ D\{\hat{\boldsymbol{\xi}}\} &= \sigma_0^2 (\mathbf{N} + \mathbf{E}^T \mathbf{E})^{-1} \mathbf{N} (\mathbf{N} + \mathbf{E}^T \mathbf{E})^{-1} \\ \hat{\sigma}_0^2 &= \frac{\tilde{\mathbf{e}}^T \tilde{\mathbf{e}}}{2n} \end{aligned} \tag{4.24}$$

where $\mathbf{N} = \mathbf{A}^T \mathbf{A}$ and $\mathbf{c} = \mathbf{A}^T \boldsymbol{\omega}$; E satisfies the two conditions $\mathbf{A}\mathbf{E}^T = 0$, and $\text{rk}(\mathbf{A}) + \text{rk}(\mathbf{E}) = m$, meaning that \mathbf{E}^T spans the null-space of A, $\Re(\mathbf{E}^T) = \mathcal{N}(\mathbf{A})$. Thus, the matrix E can be found by generating a basis for the null space of A. The computation of the null space of a matrix for large systems is not problematic since most of the mathematical software nowadays include subroutines for doing so, e.g. the function Null in Matlab.

Once a solution is found, this can be referred to a particular set of control points that will bring the adjusted gravity values to the desired datum.

For the latter case we can augment the system as:

$$\begin{aligned} \boldsymbol{\omega} = \mathbf{B}\mathbf{y} &= \mathbf{A}\boldsymbol{\xi} + \mathbf{B}\mathbf{e}, \quad \boldsymbol{\omega} \sim (\mathbf{A}\boldsymbol{\xi}, 2\sigma_0^2\mathbf{I}), \\ \boldsymbol{\kappa}_0 &= \mathbf{K}\boldsymbol{\xi}, \quad \text{rk} \begin{pmatrix} \mathbf{A} \\ \mathbf{K} \end{pmatrix} = 2n + 4, \end{aligned}$$

where K is the design matrix for the constraints and $\boldsymbol{\kappa}_0$ the vector containing values for those constraints. The vector $\boldsymbol{\kappa}_0$ contains the values for the biases and trends of at least two lines in order to overcome the datum defect. This means that we need to have access

to the gravity information of at least two identical points (of control, and of Kalman residuals) in two different lines respectively. The solution by least squares is given by:

$$\begin{aligned}\hat{\xi} &= (N + K^T K)^{-1} \mathbf{c} + (N + K^T K)^{-1} K^T (K(N + K^T K)^{-1} K^T)^{-1} (\mathbf{\kappa}_0 - K(N + K^T K)^{-1} \mathbf{c}) \\ D\{\hat{\xi}\} &= \sigma_0^2 [(N + K^T K)^{-1} - (N + K^T K)^{-1} K [K(N + K^T K)^{-1} K^T]^{-1} K (N + K^T K)^{-1}] \quad (4.25) \\ \hat{\sigma}_0^2 &= \frac{\tilde{\mathbf{e}}^T \tilde{\mathbf{e}}}{2n}\end{aligned}$$

Once the unknown constrained vector $\hat{\xi}$ is estimated, the biases and trends for all the lines in the area are available and can be corrected by relating those lines to the particular datum (control information).

4.4 Data processing to get the gravity vector

In this part, the computation of the gravity disturbance vector from data collected on flights over the Canadian Rocky Mountains by the University of Calgary is explained. For the processing of the data the method described in section 4.2 is used. A description of the area of study along with the collected data is presented. Some preliminary manipulations of the data, such as matching to control points and crossover adjustment, are described.

4.4.1 Area of study

Data for the experiment come from an area in the Canadian Rocky Mountains from a flight in September 1996 (Bruton, 2000). The flight was done with several lines arranged in the north-south direction and with two lines in the east-west direction. The lines in the east-west direction were planned for use in a crossover adjustment. The lines in the area were numbered from 1 to 14 in the direction of the flight for future identification and reference. The area of study and the flight lines are shown in Figure 4.2.

calgary ins-gps

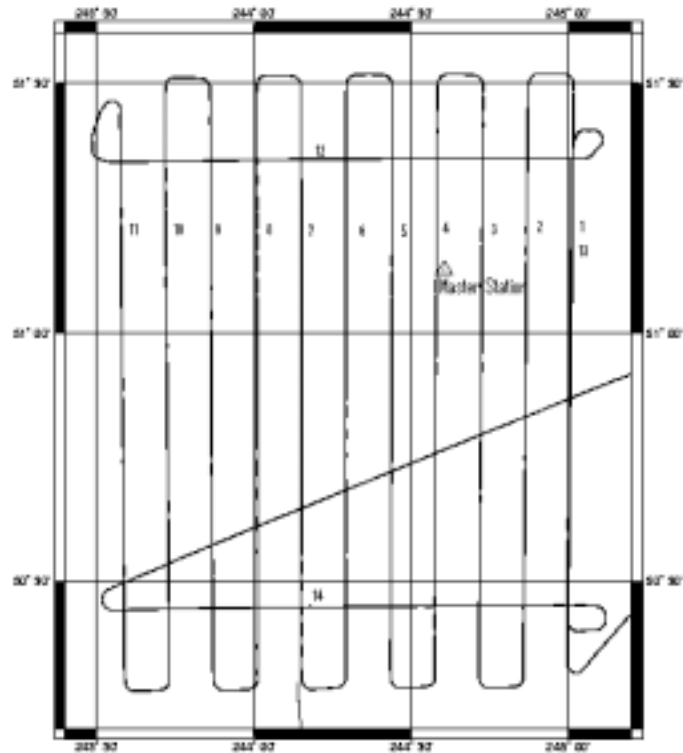


Figure 4.2: Description of the area for the study

The following parameters were used to obtain the kinematic solution:

Position of the Master Station:

$$\varphi = 51^{\circ}07'39.8705'' ; \lambda = -115^{\circ}23'42.5107'' ; h = 1323.2594 \text{ m}$$

Initial epoch for GPS data: 278753.0 s

End of Static period : 279653.0 s

Final epoch : 302000.0 s

Initial attitude angles:

$$\text{Roll} = -0.066^{\circ} ; \text{Pitch} = +2.454^{\circ} ; \text{Yaw} = -65.466^{\circ}$$

Initial INS position:

$$\varphi = 51^{\circ}06'07.392'' ; \lambda = -114^{\circ}02'07.667'' ; h = 1059.720 \text{ m}$$

Initial velocities: 0.0, 0.0, 0.0

Alignment time: 900 sec

Time delay (GPS-INS): -1.996 sec

Data Rate: 50 Hz

GPS_INS_offsets (GPS-INS) for lever arm correction [m]: -0.462, -1.203, 1.078, given in the b frame.

Gyro biases [deg/sec]: 2.258729×10^{-6} ; 2.695203×10^{-6} ; 1.005562×10^{-6}

Accelerometer biases [m/s²] : 0.00005 ; -0.000120 ; 0.00050

LRF3 gyro conversion scale factor: $(0.000000003725290298461914 \times 180/\pi)/0.02$

LRF3 accelerometer conversion scale factor: $(0.00000047683718503937 \times 0.3048)/0.02$

For the processing of the data the software developed by Kwon, 2000 was used. For the computation of the total accelerations, the GPS positions from the kinematic solution provided by the University of Calgary was numerically differentiated twice for later use in determining the gravity vector.

4.4.2 The gravity disturbance vector

The procedure explained in section 4.1 was followed to obtain the gravity disturbance vector. Consecutive smoothing filters of 2 seconds and 90 seconds smoothing windows were applied to both INS and GPS signals in order to remove high frequency noise in the GPS accelerations coming from the numerical differentiation. The lever arm effect correction computed from the parameters used for the kinematic solution (see previous page) was applied to the INS accelerations. This correction is computed by (Jekeli, 2000, p.329):

$$\ddot{\mathbf{x}}_{\text{antenna}}^i - \ddot{\mathbf{x}}_{\text{IMU}}^i = \frac{d}{dt} (C_b^i \boldsymbol{\omega}_{ib}^b \times \mathbf{b}^b) \quad (4.26)$$

with \mathbf{b}^b the vector containing the differences in coordinates between the GPS antenna and the IMU in the b frame. The differentiation is done numerically with a 2 second smoothing. A 90 second smoothing window is also applied to the lever arm effect before correcting the INS accelerations.

In Figure 4.3 the smoothed accelerations for the first three lines, as described in Figure 4.2, coming from GPS and INS are presented for each one of the components in the north, east, and down direction. We can observe similar characteristics in both accelerations, which is an indication that both sets represent the general acceleration profile of the aircraft.

The difference between GPS and INS accelerations for lines 1 to 3 are shown in Figure 4.4, Lines 1 to 3 are shown as a sample since all the lines in the flight present the same characteristics.

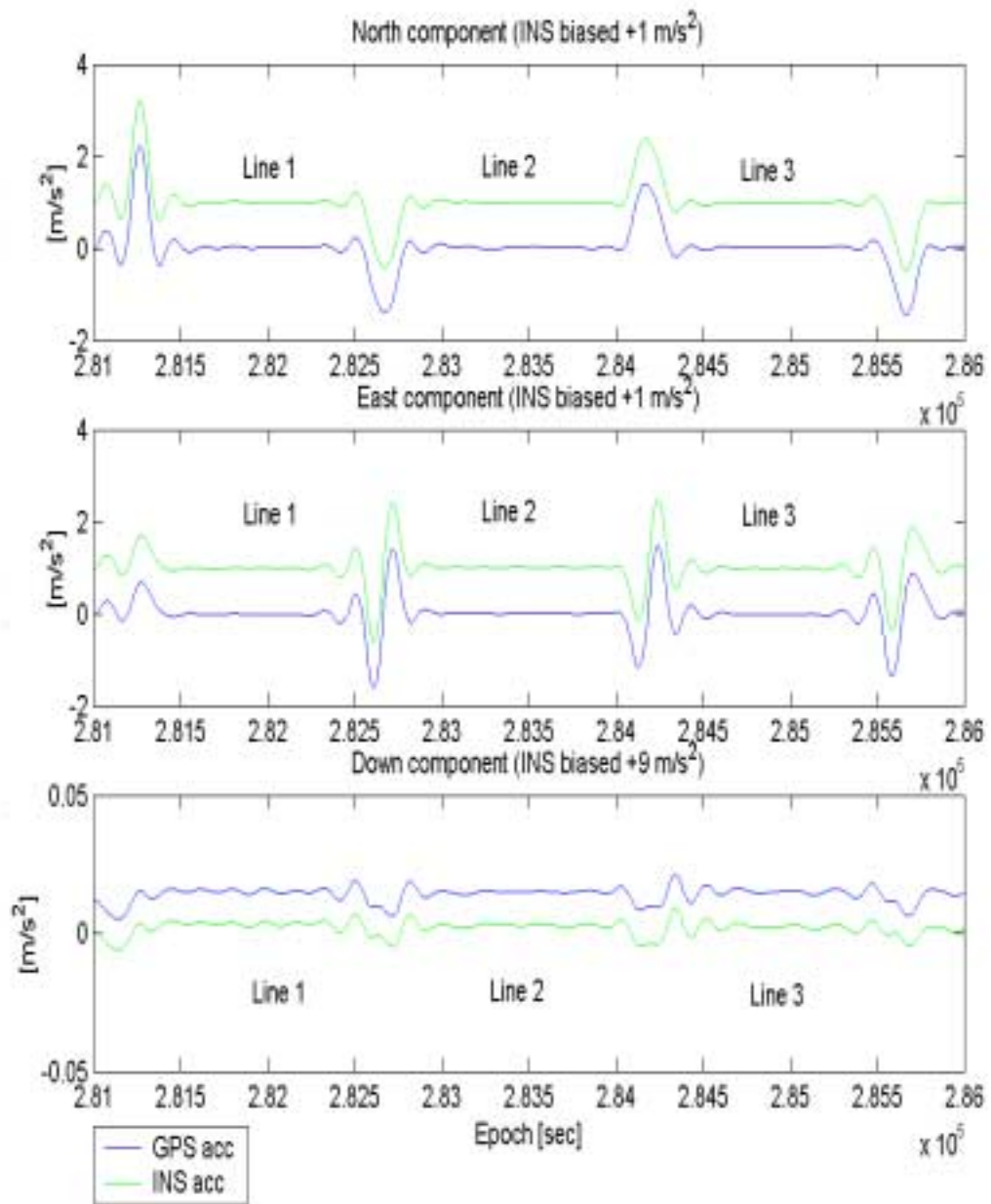


Figure 4.3: GPS and INS accelerations for Lines 1 to 3

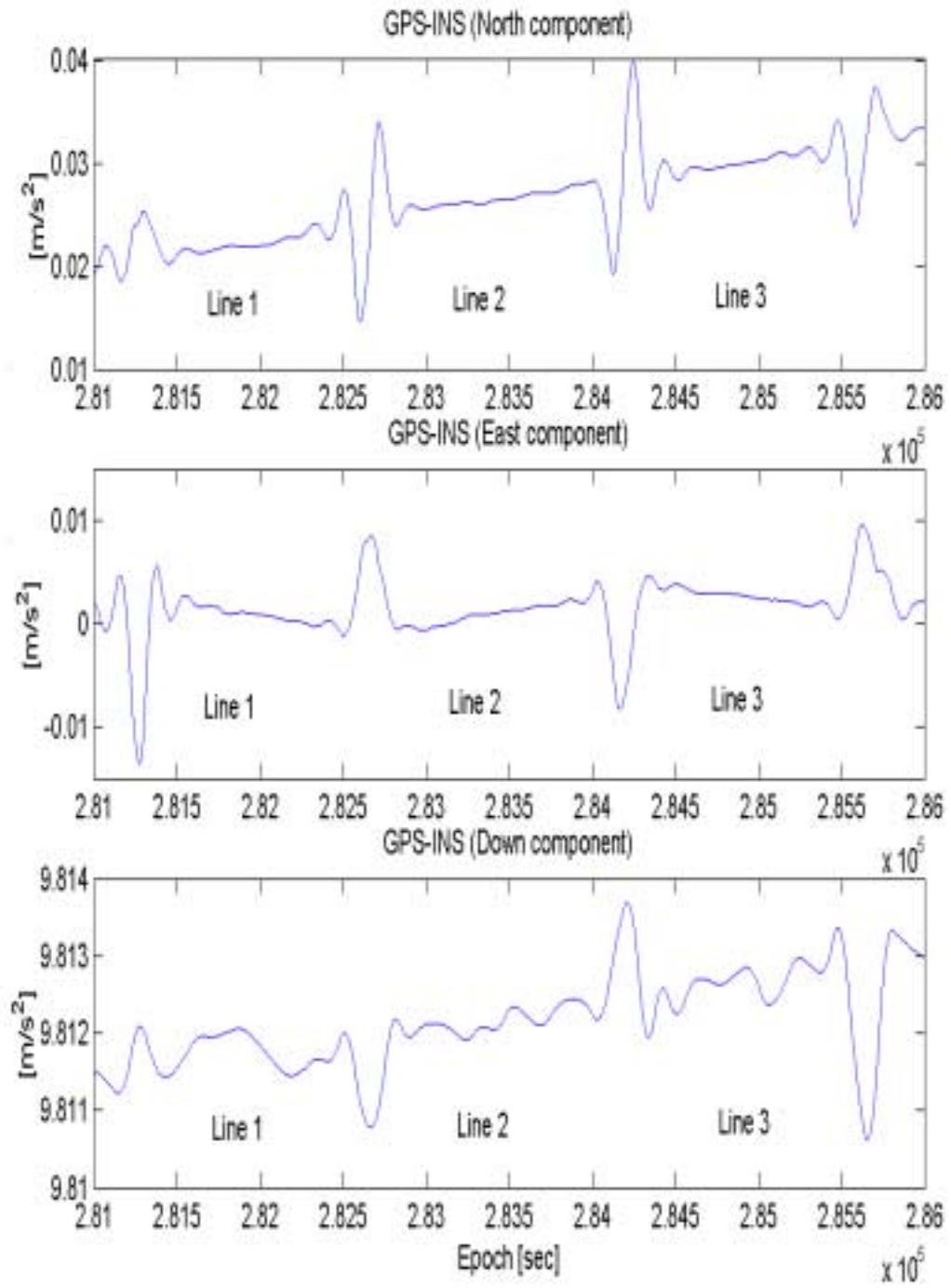


Figure 4.4: Differences GPS –INS derived accelerations for lines 1 to 3

The Kalman filter algorithm as described in section 4.2.2 was applied to the GPS and INS accelerations, and the residuals representing the components of the gravity disturbance vector can be seen for lines 1 to 3 in Figure 4.5:

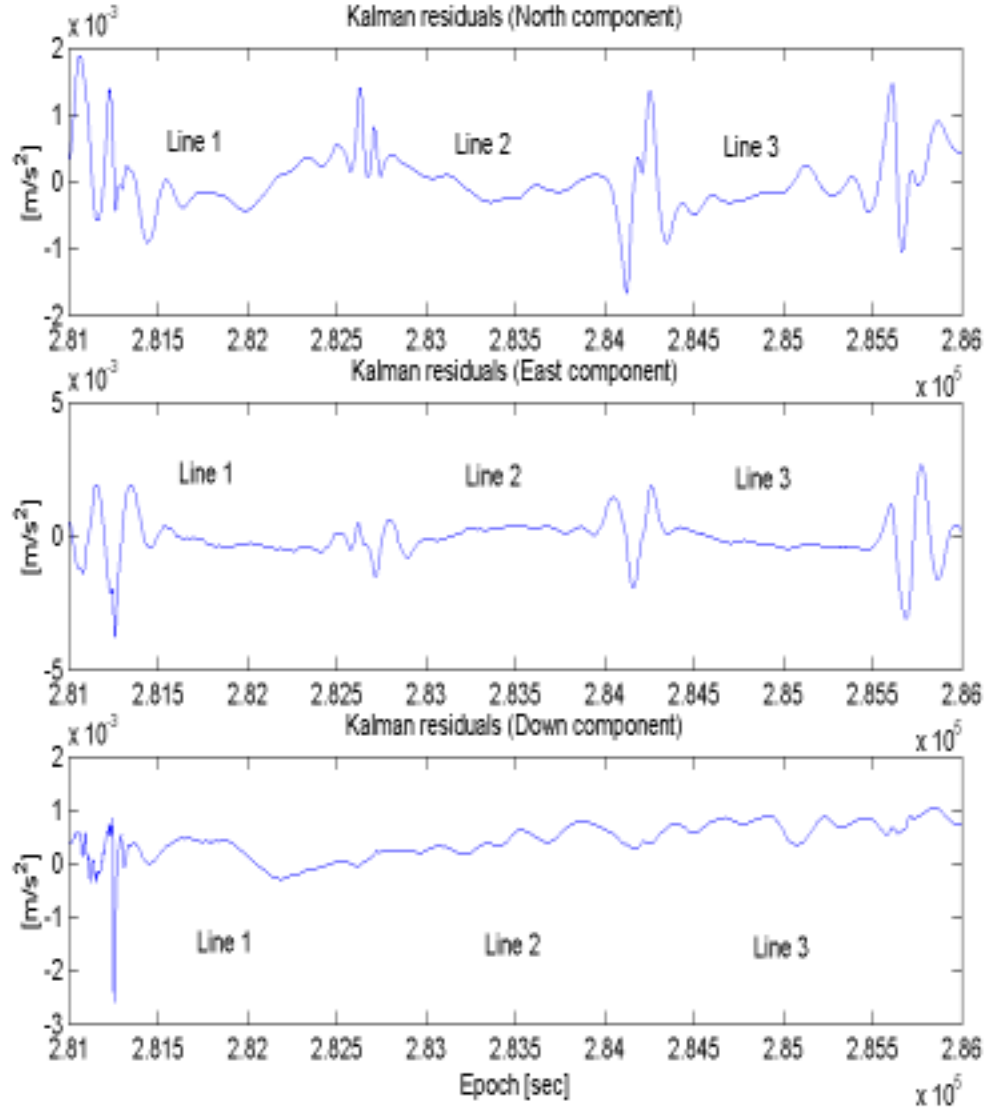


Figure 4.5: Residuals for lines 1 to 3 after applying Kalman filter

4.4.3 Experiments to remove large oscillation at the 180° turnings of the airplane

From Figures 4.3 to 4.5 we can notice large oscillations present in the residuals and in the original accelerations, at every 180° turn of the airplane. These oscillations are more noticeable in the north and east components than in the vertical component. In order

to try to remove these oscillations in the residuals some experiments were carried out, and some results are presented in the following.

4.4.3.1 Using the vertical component orientation error in the Kalman filter

We think that the fact that the oscillations are more noticeable in the north and east components is because of the dynamics of the airplane at the turns, mainly affecting the north and east components directly as explained in the following:

Acceleration errors in the navigation frame are caused by errors in the sensed acceleration and by orientation errors coming from the gyros. The acceleration error for the navigation frame can be written as (Jekeli, 2000, p.155):

$$\delta \mathbf{a}^n = \mathbf{C}_s^n \delta \mathbf{a}^s + \mathbf{a}^n \times \boldsymbol{\psi}^n \quad (4.27)$$

$$\text{with } [\mathbf{a}^n \times] = \begin{bmatrix} 0 & -a_D & a_E \\ a_D & 0 & -a_N \\ -a_E & a_N & 0 \end{bmatrix}, \text{ and } \boldsymbol{\psi}^n = \begin{bmatrix} \psi_N \\ \psi_E \\ \psi_D \end{bmatrix}.$$

Considering only the errors in the orientation we can write:

$$\delta \mathbf{a}^n = \mathbf{a}^n \times \boldsymbol{\psi}^n = \begin{bmatrix} -a_D \psi_E + a_E \psi_D \\ a_D \psi_N - a_N \psi_D \\ -a_E \psi_N + a_N \psi_E \end{bmatrix} \quad (4.27)$$

A look at equation (4.27) suggests that the vertical component of the orientation errors contributes directly to the errors in the north and east accelerations. The vertical component orientation error is associated with an error in azimuth. At the 180° turns of the aircraft, the azimuth is changing at a faster rate than when the plane is flying in a north-south direction, and it may be possible that this causes instabilities in the vertical gyro, not reflected in the horizontal gyros. This instability may be causing errors in the north and east components of the INS acceleration as indicated by equation (4.27). We may try to isolate the vertical component orientation error by comparing the computed GPS and INS azimuths as explained later in this section. Equation (4.27) also shows effects on the acceleration error coming from the east and north components of the orientation error. It is difficult, if not impossible, to compute the effect due to the horizontal components of the orientation error, but we could have access to the effect of the horizontal component orientation error from the Kalman filter results. On the other hand, we could assume that their effect is small due to the reasons explained above; however, we have to keep in mind that the errors coming from these components are multiplied by the vertical component of the acceleration, which is larger in magnitude than the horizontal acceleration components.

In an attempt to correct the large oscillations in the INS-GPS acceleration differences the following approach was developed. We assumed that the GPS azimuths are better determined than the azimuth provided by the INS, and that the latter can be

corrected by computing the azimuth error as the difference between the GPS and the INS azimuth. With the GPS and INS azimuths we can compute the vertical component of the orientation error:

$$\Psi_D = \alpha_{INS} - \alpha_{GPS} \quad (4.28)$$

The GPS azimuth can be computed with good approximation, considering that the changes in latitude and longitude during the GPS data interval of 1 second are small:

$$\alpha_{GPS} = \arctan \left[\frac{\Delta \lambda \cos(\varphi_{med})}{\Delta \varphi} \right]$$

The INS azimuth is derived by applying the transformation matrix from the sensor to the navigation frame given by information in the quaternion file. This transformation can be written as:

$$C_s^n = C_i^n C_s^i$$

with C_s^i transformation matrix from the sensor to inertial frame (from the gyros),

C_n^i transformation matrix from the navigation to the inertial frame (function of the latitude, longitude and Earth rate rotation),

C_s^n transformation matrix from the sensor to the navigation frame (function of η, χ, α),

η, χ, α the roll, pitch and yaw angles relating the body frame to the navigation frame.

The INS azimuth can now be computed from the C_s^n matrix as:

$$\alpha_{INS} = \arctan \left[\frac{-C_s^n(2,1)}{C_s^n(1,1)} \right]$$

Now we try to correct the INS acceleration, neglecting errors coming from the horizontal components of the orientation errors, and only considering the vertical component orientation error as computed by equation (4.28) as follows:

$$\delta \mathbf{a}^i = C_n^i \delta \mathbf{a}^n$$

$$\text{with } \delta \mathbf{a}^n = \begin{bmatrix} a_E \Psi_D \\ -a_N \Psi_D \\ 0 \end{bmatrix}.$$

With this we can now correct the observed inertial acceleration to be used in the Kalman filter update as:

$$\mathbf{a}_c^i = \mathbf{a}^i + \delta \mathbf{a}^i,$$

where \mathbf{a}_c^i stands for corrected acceleration in the inertial frame, and substitutes the original INS observed inertial acceleration.

The Kalman filter residuals with the accelerations corrected by the procedure explained above was implemented, but the results did not show any improvement when compared to the original results. Actually the results were out of the bounds of what one would expect. A look at the differences between the GPS and INS azimuths showed that we had large differences not only at the turns of the airplane, where we found peaks for these differences, but also along all the lines. This may indicate that we might have errors coming from other sources, like the other two components of the orientation errors, or from errors in the accelerometers (see equation (4.15)). We found large differences between the GPS and INS azimuths ranging from -3° to 3° . This is probably too large to provide a good estimate of ψ_D .

Next we considered including the computed orientation error (equation (4.28)) as an observation in the Kalman filter update and not as a correction as done above. For this we modified the original observation equation as follows:

$$\mathbf{y}_k = \mathbf{H}\mathbf{x}_k + \mathbf{e}_k, \quad \mathbf{e}_k \sim (0, \mathbf{R}_k)$$

with:

$$\mathbf{y}_k = \begin{pmatrix} \tilde{\mathbf{x}}^i - \tilde{\mathbf{a}}^i - \boldsymbol{\gamma}^i \\ \psi_D \end{pmatrix}$$

and $\mathbf{H}_k = \begin{pmatrix} -\mathbf{C}_b^i & \mathbf{0}_{3 \times 3} & -[\tilde{\mathbf{a}}^i]\mathbf{C}_b^i & \mathbf{0}_{3 \times 3} & [\tilde{\mathbf{a}} \times] \\ 0 & 0 & 0 & 0 & [\mathbf{C}_i^n]_3 \end{pmatrix},$

where $[\mathbf{C}_i^n]_3$, represents the 3rd row of the transformation matrix from the inertial to the navigation frame.

The Kalman filter was computed again by using this procedure, but again we did not improve the determination of the horizontal components of the gravity disturbance vector. The large oscillations still remained, being larger than the original computed Kalman residuals. The vertical component appeared to be less sensitive to the correction showing practically only a bias.

We also implemented the same approach but using the three components of the orientation error coming from a first iteration in the Kalman filter; but again the results did not show any improvement with respect to the original Kalman filter estimates.

4.4.3.2 Removal of oscillation prior to computation of Kalman filter residuals

Another attempt aiming at the removal of the large oscillations at the turns of the airplane was implemented and consisted in the application of a 30 second smoother (after the 2 seconds smoother) to both GPS and INS accelerations. This was followed by the “chopping” of the GPS accelerations from the lines at the turns trying to recover as much of the line as possible. The motivation is to guarantee the intersection of the north-south direction lines with the east-west crossing lines to allow for a posteriori crossover adjustment of the resulting Kalman residuals (a Kalman filter with condition equations to determine simultaneously the crossovers and the estimates of the gravity disturbance

vector could be explored in the future). A filter of 30 seconds is applied since the use of larger filters like the 90 or the 120 seconds smoothers spread the effect of the oscillations to the neighboring points on the lines near the turns of the plane. The Kalman filter residuals were computed as before and subjected to a filter of 90 seconds to reduce the high frequencies present in those residuals. A comparison of these new results, for some lines (lines 1 to 6), with respect to the original residuals is presented in Figure 4.6. Here, we can observe better results than in the previous experiments, but we still see traces of the oscillation at the ends of the lines affecting the residuals. This is most noticeable for the north component, where traces of the oscillations are evident at the end of each line. We notice some improvement for the east component, but in general some remaining effects of the oscillations are still present. Regarding the vertical component, this suffers no major effect and the comparison with the original residuals shows no significant discrepancies.

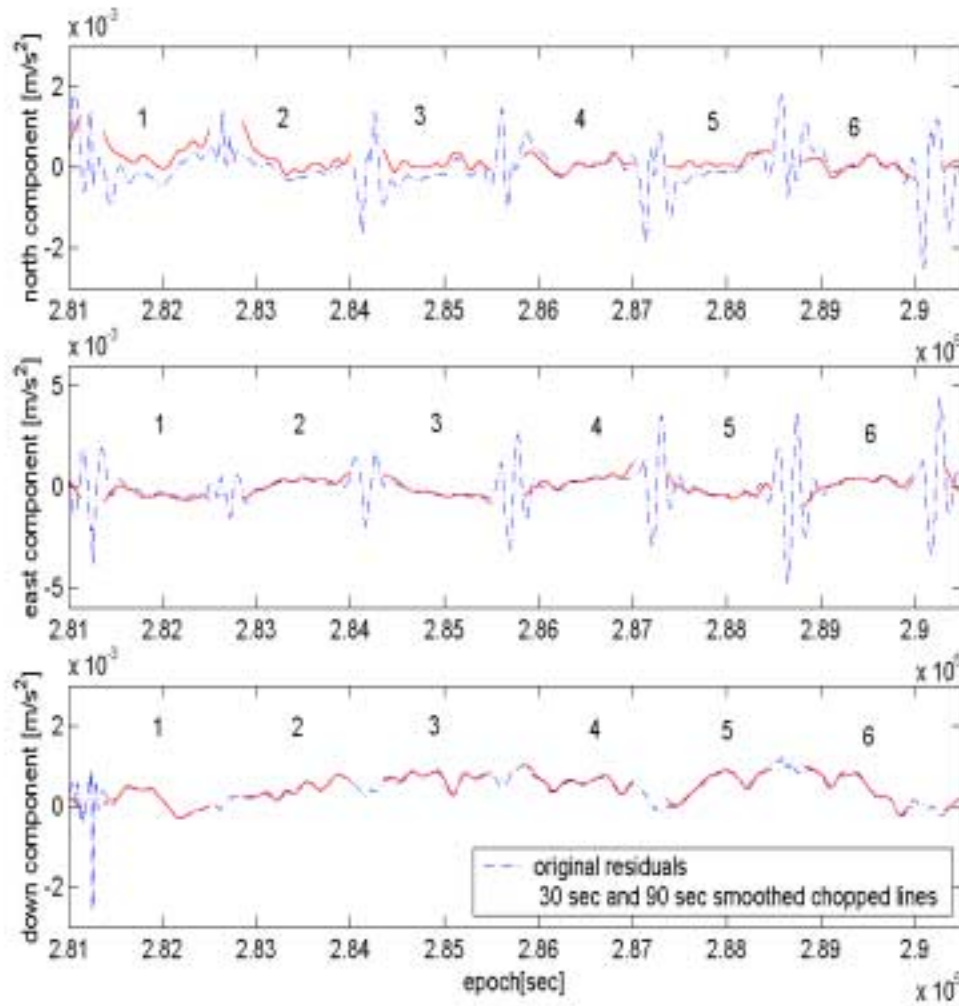


Figure 4.6: Comparison of the 30 sec smoothed chopped lines and 90 second smoother to the residuals with the original Kalman filter residuals.

We also tried to remove the oscillations by the use of different combinations of smoothers, but we did not succeed in doing so. We feel that more specific research in this direction is necessary and that other techniques can be investigated like the use of wavelets or the implementation of iterative procedures for the Kalman filter computation.

4.4.4 Removal of the large oscillation at the 180° turnings of the airplane from the resulting Kalman residuals

In order to remove these oscillations the lines were truncated consistently at both ends in order to recover as much of the signal as possible for subsequent computations. In doing so, information over 50% of each line is lost for the north and east components, and a cross-over adjustment with lines 12 and 14 was not possible. The final set of lines to be used in the computations are shown in Figure 4.7.

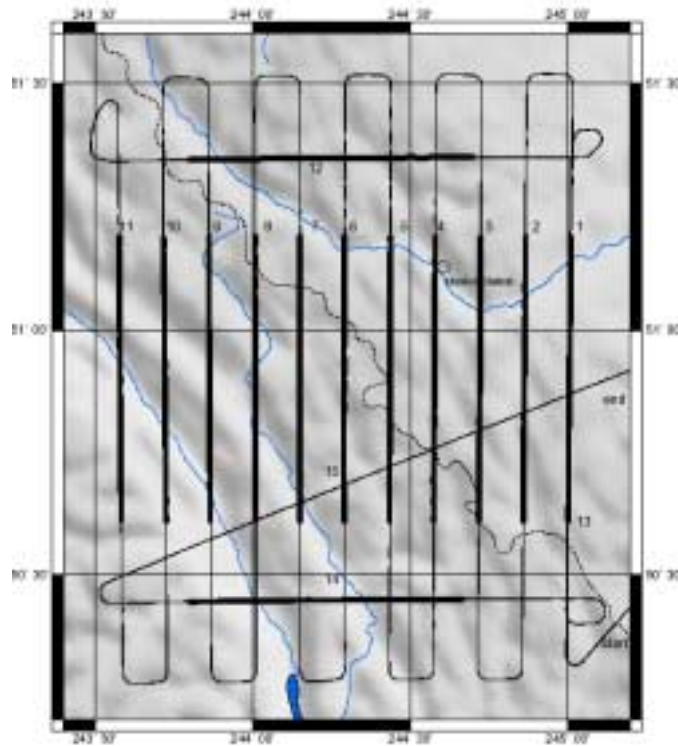


Figure 4.7: Truncated lines excluding large oscillations

Notice how the east-west lines 12 and 14 do not intersect the truncated north-south lines, not allowing for a cross-over adjustment. All three components were truncated for later comparison, even though it was not necessary for the vertical. An individual cross-over analysis for the vertical components is presented in section 4.5.2.1, and the application of Hotine's integral solution makes use of the longer lines of data as well.

4.5 Accuracy of the gravity disturbances with respect to control points

In order to assess the quality of the results, the Kalman filter residuals, which represent the components of the gravity disturbance vector, were compared to control information provided by NIMA for the different lines of interest.

NIMA provided information about the deflections of the vertical in arc-seconds, and the gravity disturbances in mGal for a height of 4360 m (an average of the height for the actual flight). In order to obtain the horizontal gravity disturbance components from NIMA, and according to Figure 4.8, the following approximations for obtaining the gravity disturbances were applied:

$$\delta g_N [\text{mGal}] \cong -4.75 \xi ["]$$

$$\delta g_E [\text{mGal}] \cong -4.75 \eta ["]$$

- with δg_N North component of the gravity disturbance vector,
- δg_E East component of the gravity disturbance vector,
- ξ deflection of the vertical in North direction,
- η deflection of the vertical in East direction,
- 4.75 transformation factor from arc-seconds to mgal
 $\sim 981000 \text{mgal} * (\pi/180^\circ) * (1^\circ/3600'')$.

For the case of the gravity disturbances, which were already given in mGal, no transformation was applied.

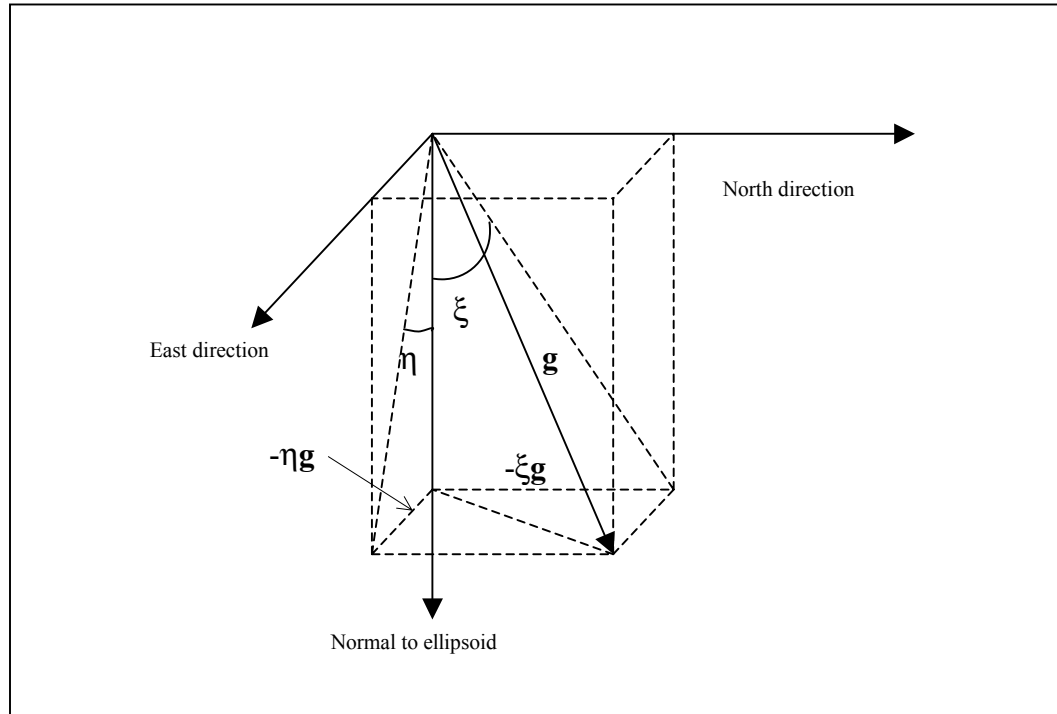


Figure 4.8: The components of the gravity vector

The data provided by NIMA correspond to an area in latitude from 50° to 52° north, and in longitude from 243 ° to 246.5° east, with a resolution of 2'. The accuracy of the control data is estimated to be better than 5 mGal for the horizontal components, and better than 1.5 mGal for the vertical component. The reference normal field is that of WGS84.

Values for control data were interpolated at each corresponding point of the truncated flight lines and were compared to the Kalman filter residuals. Statistics for the comparison are presented in Table 4.1 to 4.3.

	Mean [mGal]	Std. Dev ±[mGal]	Min [mGal]	Max [mGal]
Line 1	2.5	20.1	-41.5	33.0
Line 2	-0.1	10.1	-16.0	18.4
Line 3	-8.3	19.9	-37.6	22.1
Line 4	-1.4	7.2	-9.9	15.5
Line 5	-21.8	19.8	-66.4	5.1
Line 6	-9.2	8.7	-33.6	5.5
Line 7	-33.7	4.9	-48.3	-26.5
Line 8	-18.4	10.5	-41.3	-1.2
Line 9	-19.0	11.1	-46.0	6.9
Line 10	-2.3	16.0	-23.9	45.8
Line 11	-19.2	14.2	-52.9	6.5

Table 4.1: Differences of north gravity disturbances versus NIMA control

	Mean [mGal]	Std. Dev ±[mGal]	Min [mGal]	Max [mGal]
Line 1	3.8	5.0	-8.1	13.9
Line 2	54.0	12.5	25.3	73.1
Line 3	-18.1	7.0	-28.4	2.1
Line 4	19.9	8.5	3.0	35.2
Line 5	-51.3	17.2	-87.1	-11.4
Line 6	-2.3	9.6	-25.1	18.9
Line 7	-52.0	10.7	-67.3	-29.9
Line 8	-38.6	8.6	-58.2	-17.7
Line 9	-21.4	30.2	-70.0	32.1
Line 10	-32.4	12.8	-71.3	-14.3
Line 11	-0.7	19.3	-45.8	21.6

Table 4.2: Differences of east gravity disturbances versus NIMA control

	Mean [mGal]	Std. Dev ± [mGal]	Min [mGal]	Max [mGal]
Line 1	-40.7	3.2	-47.0	-33.0
Line 2	-11.4	3.7	-18.3	-4.4
Line 3	1.6	5.3	-8.0	14.4
Line 4	-2.0	5.3	-14.3	5.2
Line 5	8.5	5.2	-0.1	19.0
Line 6	10.0	4.9	-1.4	18.2
Line 7	21.1	6.3	9.0	34.1
Line 8	19.2	5.4	9.2	29.4
Line 9	30.8	5.6	22.8	41.9
Line 10	30.9	5.4	19.5	42.0
Line 11	40.6	6.5	30.9	56.8

Table 4.3: Differences of vertical gravity disturbances versus NIMA control

4.5.1 End-matching the residuals with NIMA control

In order to correct trends and biases present in the Kalman filter residuals these were adjusted to the NIMA data (assumed errorless) at the ends of each line. Results of the end-matching for some lines are presented in Figures 4.9 to 4.12, and statistics for the differences can be observed in Tables 4.4 to 4.6. The end-matching computations were done via a simple fitting procedure with the following equation:

$$\text{NIMA} = \text{RESIDUAL} + b_0 + m(t - t_0)$$

where NIMA is the control value for the component of interest, RESIDUAL the Kalman filter residual for the component of interest, b_0 the bias, and m the trend as a function of the epoch (position can also be used). The values for trend and bias can be found by:

$$x = A^{-1}y$$

where: $y = \begin{bmatrix} \text{NIMA}_1 - \text{RESIDUAL}_1 \\ \text{NIMA}_{\text{end}} - \text{RESIDUAL}_{\text{end}} \end{bmatrix}_{2 \times 1}$, $A = \begin{bmatrix} 1 & t_1 - t_0 \\ 1 & t_{\text{end}} - t_0 \end{bmatrix}_{2 \times 2}$, $x = \begin{bmatrix} b_0 \\ m \end{bmatrix}_{2 \times 1}$, and t_0 the initial epoch for each line. Note that in our case $t_1 = t_0$.

The end-matched lines will be used later to assess the quality of the geoid assuming that appropriate control is present in the area. We have to keep in mind that this

is not always possible in real situations and that poor control can be expected in some areas or countries around the world. Then the cross-over solution becomes important.

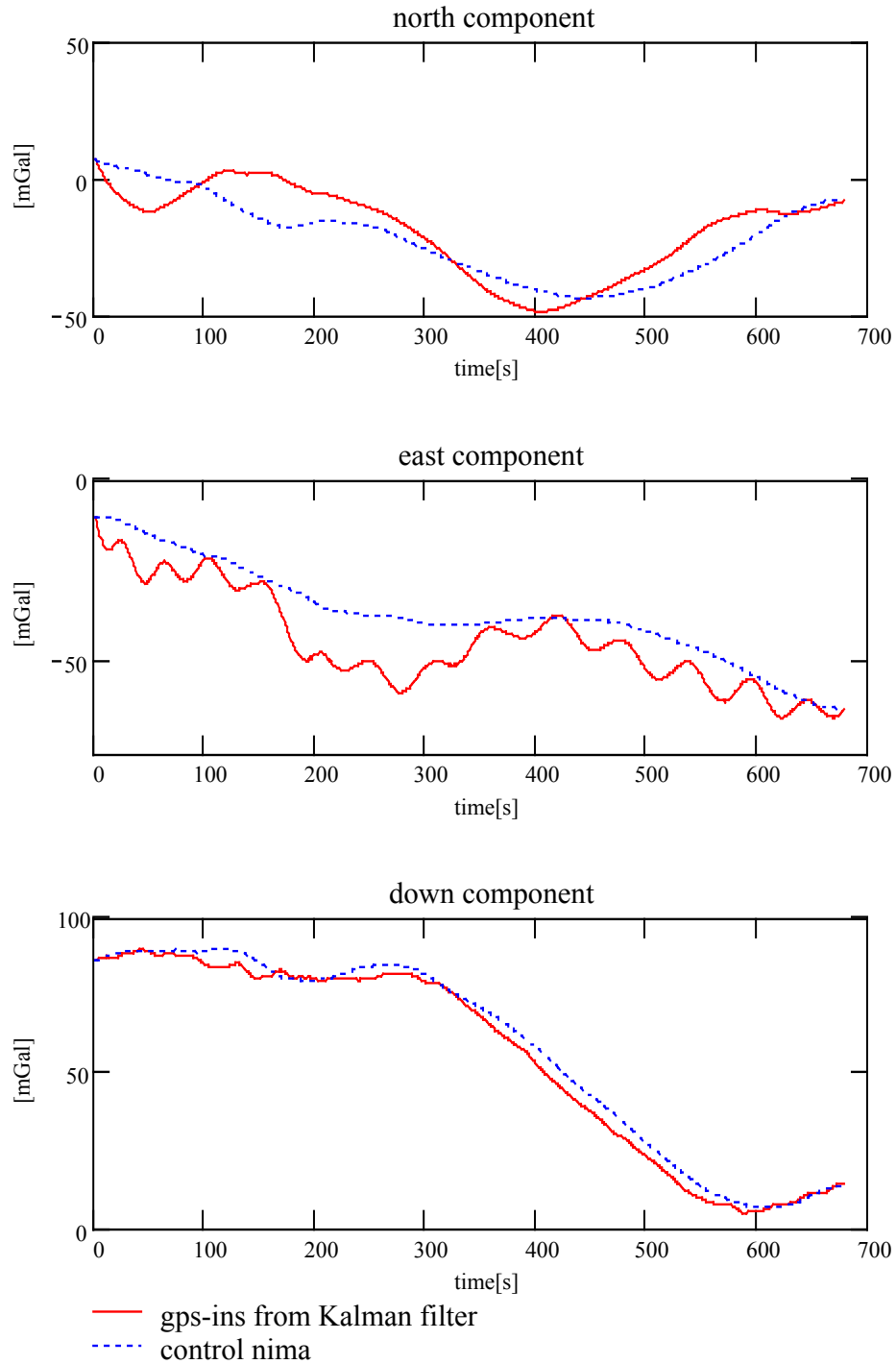


Figure 4.9: End-matched residuals vs Control (Line1)

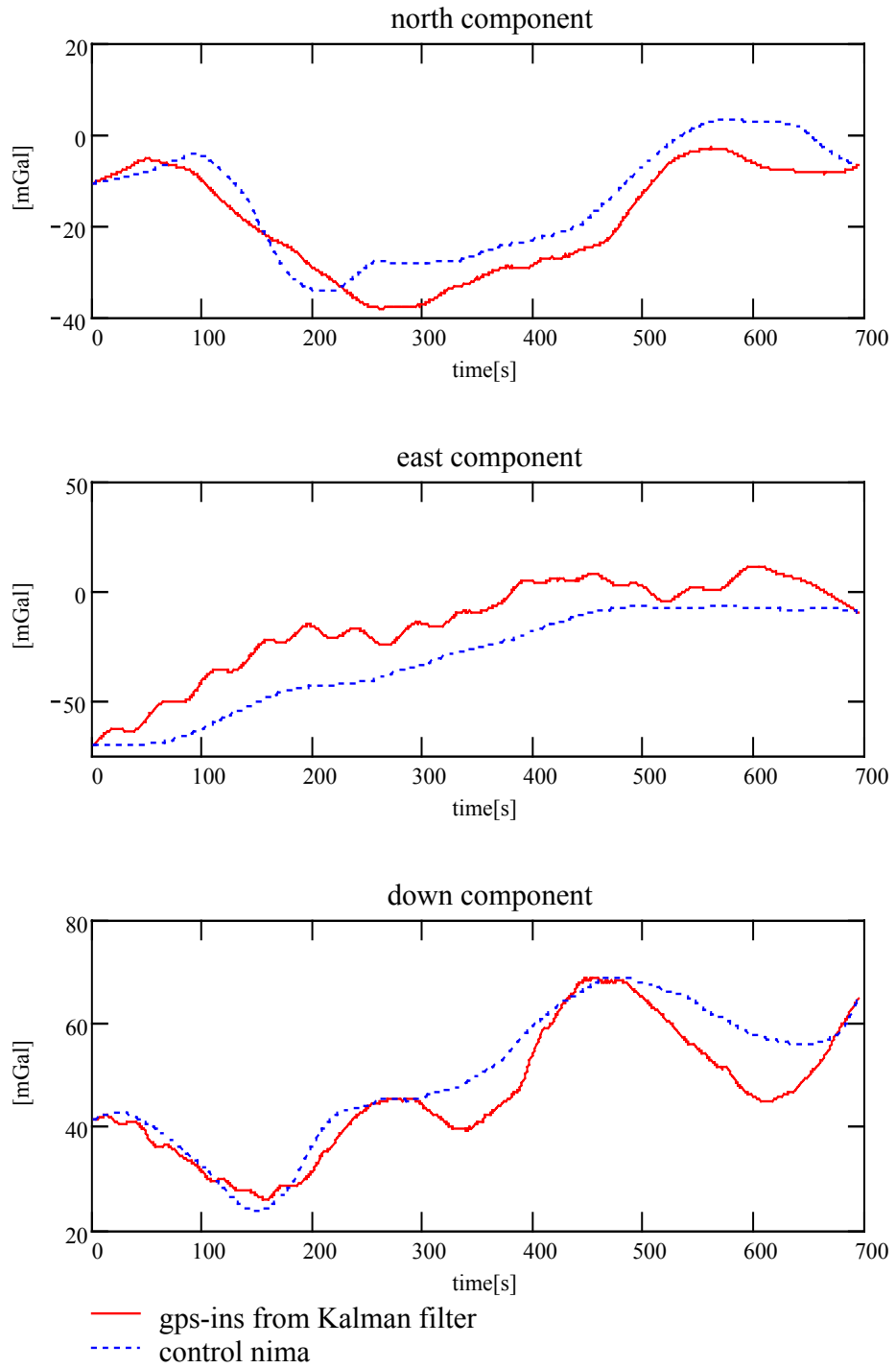


Figure 4.10: End-matched residuals vs Control (Line 2)

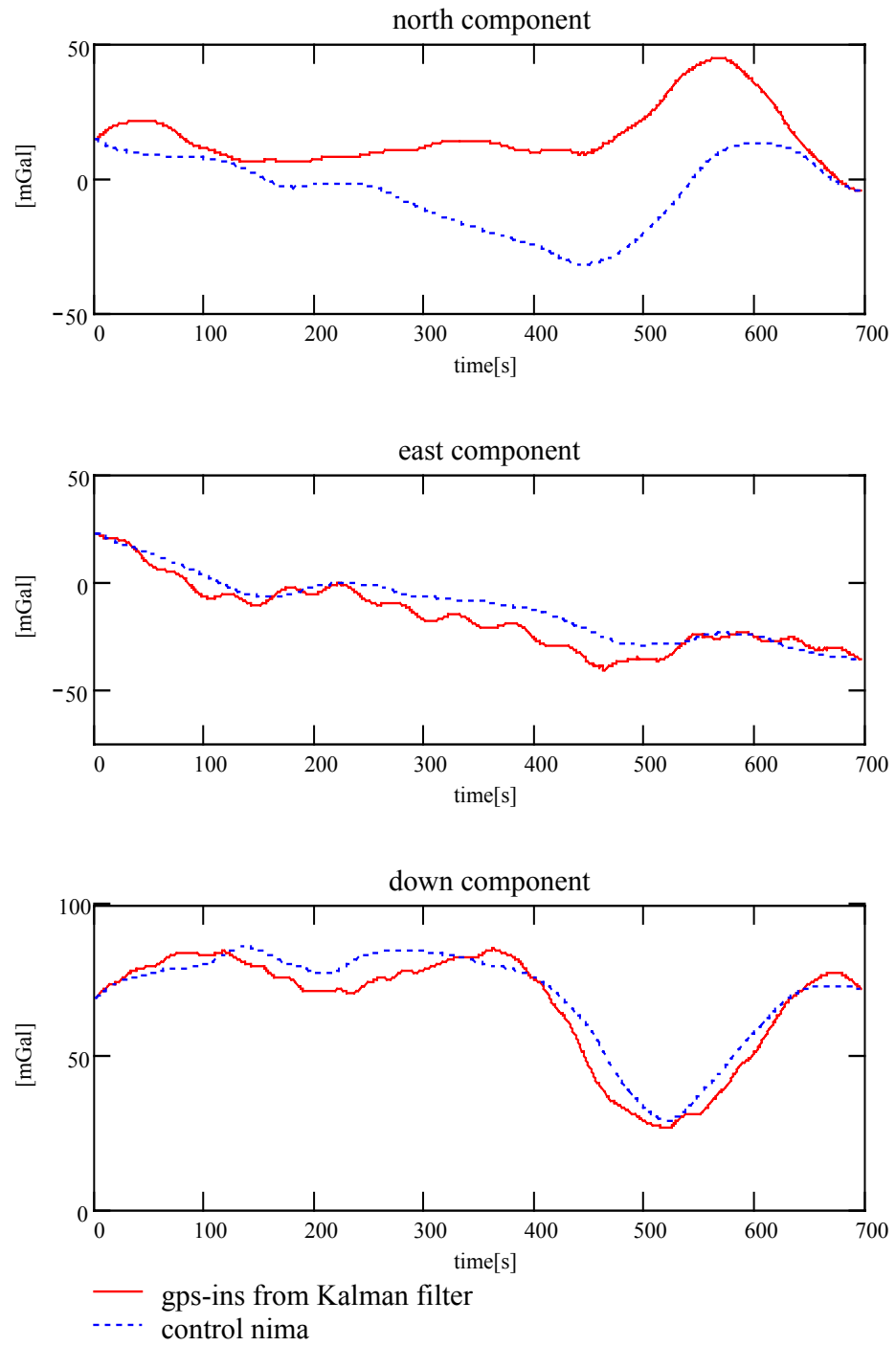


Figure 4.11: Residuals vs Control (Line 3)

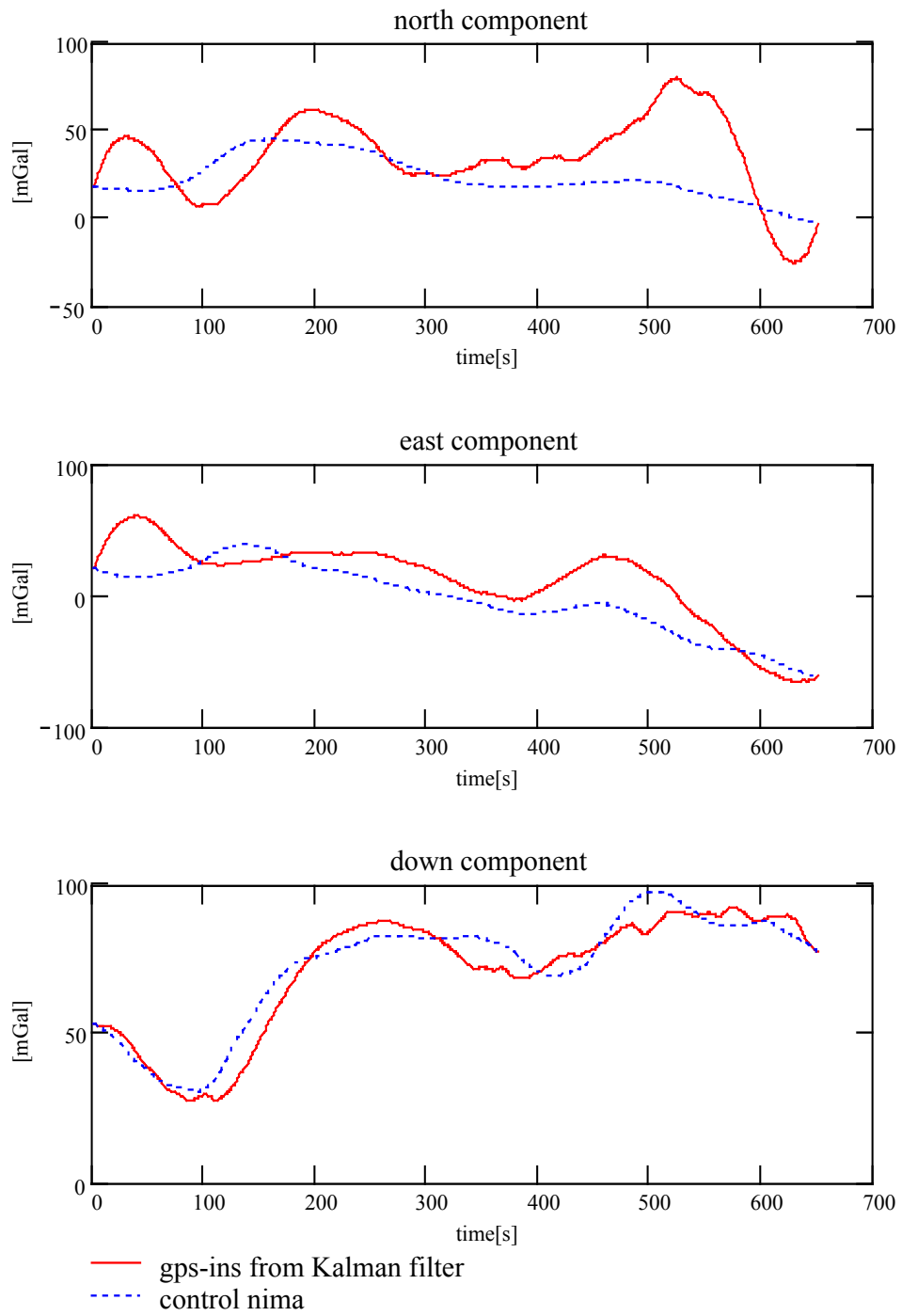


Figure 4.12: End-matched residuals vs Control (Line 12)

	Mean [mGal]	Std. Dev \pm [mGal]	Min [mGal]	Max [mGal]
Line 1	3.0	8.1	-13.6	18.2
Line 2	-4.5	4.2	-10.5	6.3
Line 3	20.7	14.9	-0.3	43.9
Line 4	-2.8	7.5	-16.2	12.9
Line 5	16.7	6.3	-0.0	26.6
Line 6	7.7	9.0	-7.8	27.5
Line 7	4.5	5.2	-3.7	15.8
Line 8	-7.7	10.4	-30.1	11.1
Line 9	17.2	10.4	0.0	37.4
Line 10	-27.1	17.4	-53.5	3.9
Line 11	3.1	16.9	-49.1	21.0

Table 4.4: Differences between end-matched north gravity disturbance and NIMA data

	Mean [mGal]	Std. Dev \pm [mGal]	Min [mGal]	Max [mGal]
Line 1	-7.5	5.1	-20.5	0.8
Line 2	15.7	6.6	-0.2	28.3
Line 3	-4.6	5.3	-15.7	5.2
Line 4	7.2	8.6	-10.6	22.9
Line 5	13.0	11.1	-5.0	42.3
Line 6	20.0	9.4	-0.9	40.5
Line 7	11.0	10.8	-4.2	33.6
Line 8	16.8	9.3	-4.8	31.4
Line 9	-4.7	11.5	-23.8	20.0
Line 10	12.7	6.9	-2.7	29.4
Line 11	0.3	10.1	-26.5	12.0

Table 4.5: Differences between end-matched east gravity disturbance and NIMA data

	Mean [mGal]	Std. Dev \pm [mGal]	Min [mGal]	Max [mGal]
Line 1	-2.5	2.2	-6.1	2.3
Line 2	-3.6	4.2	-12.5	3.6
Line 3	-2.9	4.8	-13.5	5.4
Line 4	-1.6	5.1	-13.8	5.8
Line 5	-2.3	4.3	-12.5	5.9
Line 6	0.5	5.3	-11.5	9.0
Line 7	2.3	6.5	-10.3	15.9
Line 8	-3.2	5.3	-13.0	5.8
Line 9	2.4	5.2	-5.7	12.8
Line 10	-0.5	4.8	-11.1	8.9
Line 11	-5.1	6.9	-14.8	13.1
Line 12	-1.5	5.8	-13.7	6.4
Line 14	3.8	6.6	-5.1	14.8

Table 4.6: Differences between end-matched down gravity disturbance and NIMA data

We also note that the east component for the lines in the N-S direction contains several oscillations that are not present in the other two components. It appears that these oscillations are related to the oscillations of the flight lines due to corrections by the automatic pilot of the plane trying to maintain the N-S direction. For some reason for the case of line 12, running in the east-west direction, we do not observe these oscillations (see Figure 4.14), although Kwon (2000) encountered this same behavior for lines in the east-west direction. In Figure 4.13, the trajectory of the airplane is shown for lines 1,2, and 12.

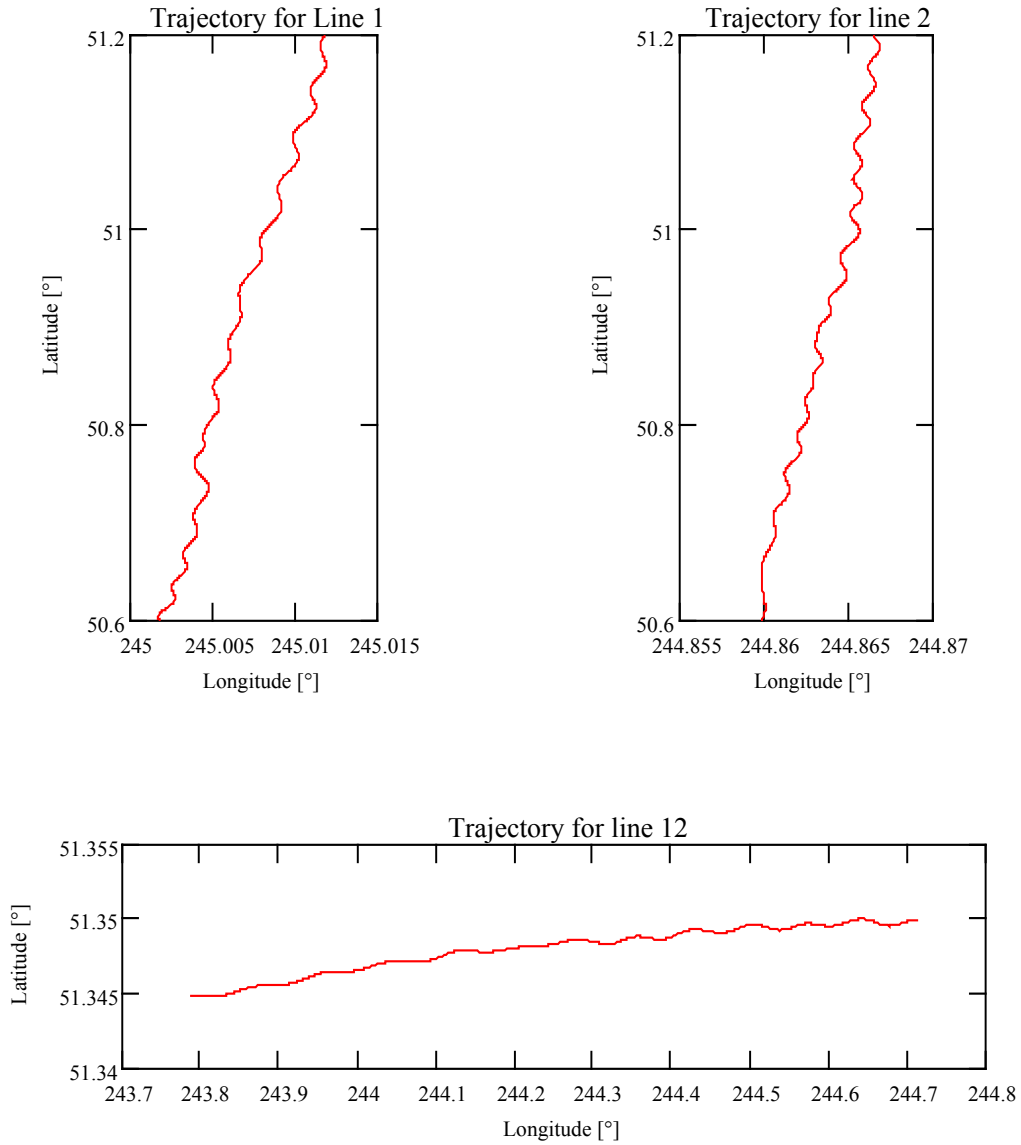


Figure 4.13: GPS trajectories for lines 1, 2 and 12

4.5.2 Crossover adjustment of the gravity disturbance vector

A crossover adjustment allows us to solve for biases and trends present in the gravity signals as it was explained in section 4.3. In this section, a crossover adjustment is performed with real data for the case of the down component, and with simulated data for the horizontal components. The latter is possible since we have control information from which we can extract the information for the crossover adjustment. Unfortunately for our set of real data it is not possible to perform an actual crossover adjustment for the

horizontal components because the crossing points occur where the estimates are affected by large errors, as explained in Section 4.4.3.

4.5.2.1 Crossover adjustment for the vertical component of the gravity disturbance vector

A crossover adjustment was performed in the vertical component of the gravity disturbance vector. In order to solve for the datum defect, the following constraints were imposed on the lines: two points in each line 1 and line 11 were taken, and the trend and constant bias for those two lines were computed using NIMA control data. These values are used as constraints in the adjustment. A comparison of the constrained crossover-adjusted lines and the original residuals with respect to the control by NIMA is presented in Table 4.7, and a graphical comparison is shown in Figures 4.14 and 4.15.

Original residuals [mGal]					Cross-over adjusted[mGal]				
	Mean	St dev[\pm]	Min	Max		Mean	St dev[\pm]	Min	Max
1	38.3	5.7	20.2	47.0	1	1.81	5.1	-24.9	7.8
2	9.0	8.0	-13.9	20.1	2	-1.4	6.1	-14.3	13.1
3	-2.5	5.7	-14.4	8.0	3	-0.5	8.6	-17.0	16.1
4	0.8	6.1	-12.4	14.3	4	-0.6	8.7	-18.3	13.9
5	-8.0	5.8	-19.0	2.2	5	4.9	10.7	-13.5	24.8
6	-9.3	4.9	-18.2	1.8	6	-0.2	4.1	-9.8	9.1
7	-20.6	6.0	-37.4	-9.0	7	-0.9	8.4	-23.8	14.8
8	-19.3	4.9	-29.4	-9.2	8	15.0	5.4	2.4	25.9
9	-31.4	6.0	-45.3	-20.8	9	5.8	5.8	-7.6	15.9
10	-32.9	5.9	-49.2	-19.4	10	9.1	4.9	-2.8	21.3
11	-42.7	6.7	-57.7	-30.9	11	6.6	8.5	-17.2	22.3

Table 4.7: Differences of the original residuals and cross-over adjusted residuals with respect to NIMA control for the vertical component

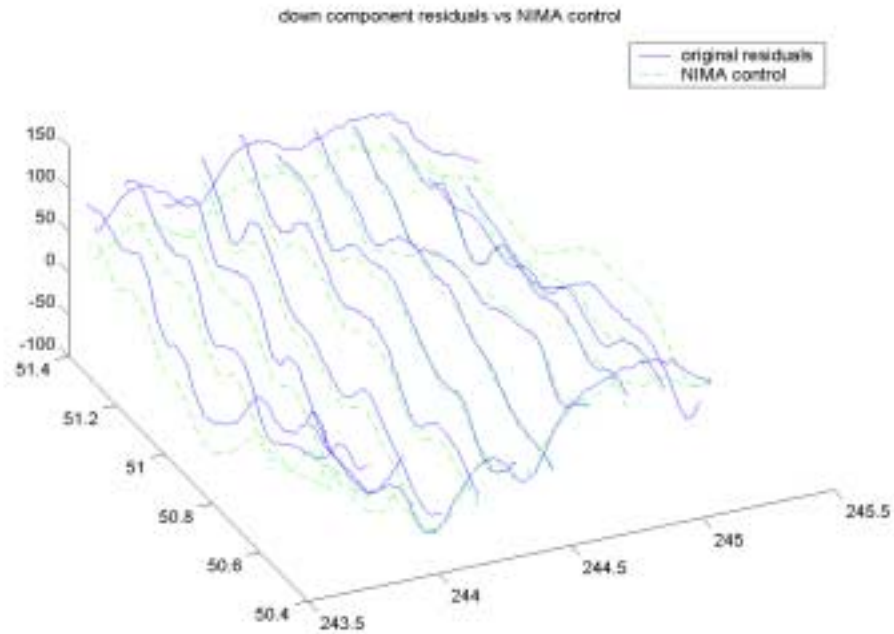


Figure 4.14: Comparison of down component residuals with respect to control by NIMA for the vertical component.

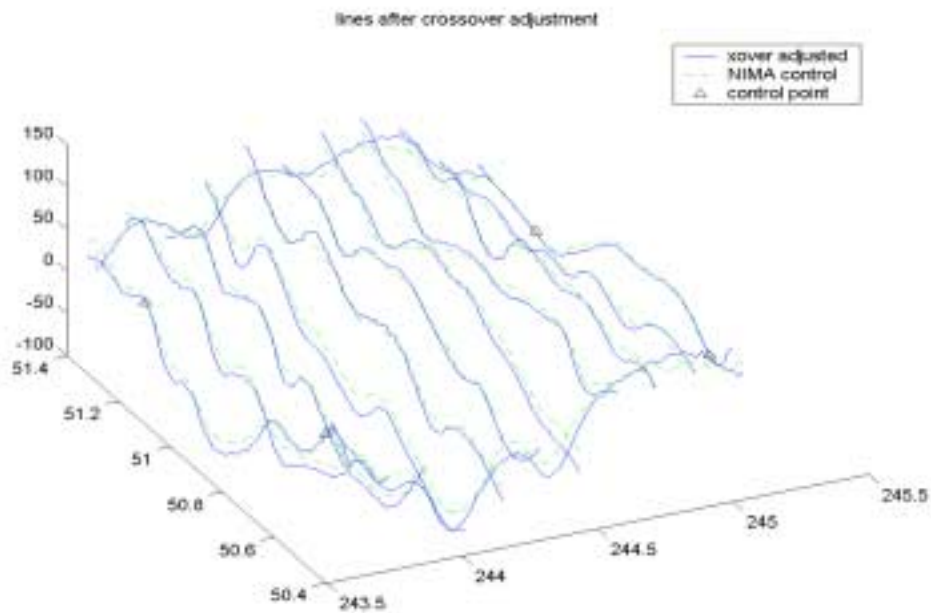


Figure 4.15: Comparison of the crossover adjusted lines with respect to control by NIMA for the vertical component.

We can observe, in Table 4.7, that the crossover adjustment provides, in general, smaller biases for all the lines than the original residuals. The deviations from the mean are similar for some lines, especially those close to the lines that served as constraints. In general, the original residuals present better standard deviations than the crossover adjusted lines. In the analysis of the statistics for the differences we have to keep in mind that the lines in the middle are adjusted to the values of the lines in the east-west direction, and these values may have larger errors at the cross-over points. A look at Figures 4.14 and 4.15 also indicates a better fit and consistency of the set of lines after crossover adjustment than of the original residuals with respect to NIMA control. The points marked as control in Figure 4.15 correspond to the points used for the constrained adjustment.

4.5.2.2 Crossover adjustment for the horizontal components of the gravity disturbance vector

In this case, a crossover adjustment was performed by the use of simulated crossing lines at the north and south ends of the horizontal components of the gravity disturbance vector. In order to do this, the values of the control data provided by NIMA at both ends of each line are extracted, and random noise is added in the order of ± 13 mGal. This value is an average of the standard deviations for the horizontal components with respect to control data (see Tables 4.1 and 4.2). The resulting crossing lines are then contaminated with a constant bias and a trend. For the bias a value of 7 mGal for the north track and a value of -8 mGal for the south track are added for both north and east components. Also a trend of 3 mGal every 10 km for the north track, and of 4 mGal every 10 km for the south track are used. The values for the constant biases and trends are included to complete the simulation procedure, and to test the crossover adjustment algorithm. However, these values are chosen arbitrarily since, for the case of the simulation, they will not affect the results if we introduce constraints and the crossover procedure is working properly. In Figures 4.16 and 4.17 the simulated crossing lines for the north and east components of the gravity vector are shown. Again, the procedure explained in section 4.3 was implemented. In order to solve for the datum defect, the trend and constant bias for line 1 and 11 are computed by using the respective end points and used in the adjustment.

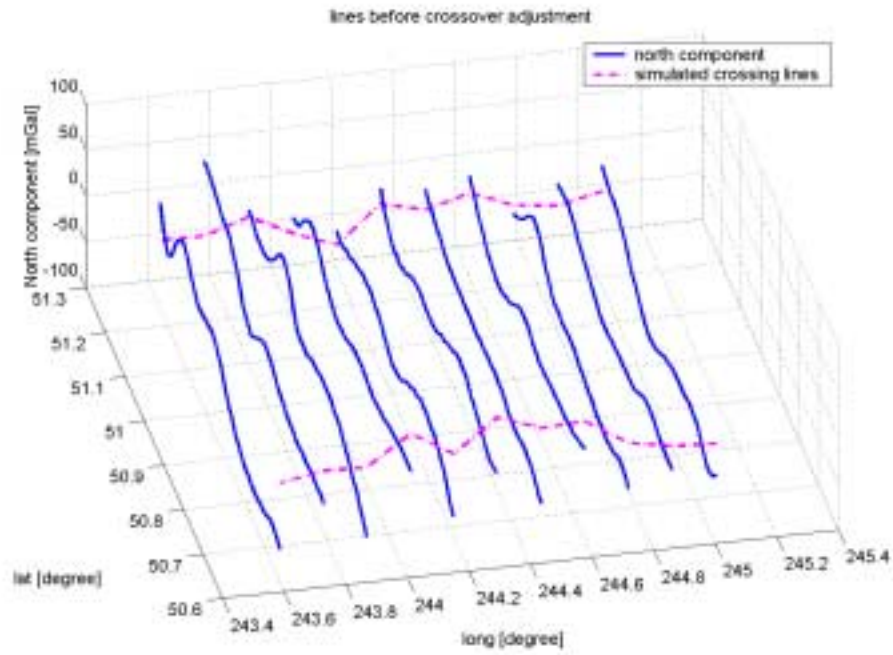


Figure 4.16: Simulated crossing tracks for the north component of the gravity disturbance vector

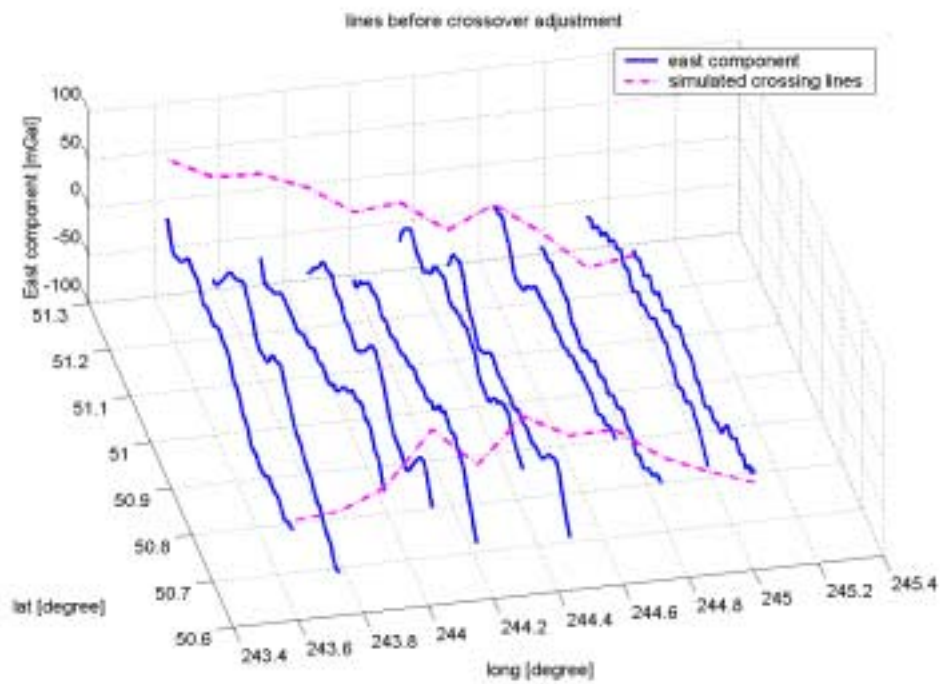


Figure 4.17: Simulated crossing tracks for the east component of the gravity disturbance vector

Statistics of the differences with respect to NIMA control for both the north and east components after the crossover adjustment are presented in Tables 4.8 and 4.9. A visual comparison is presented in Figures 4.18 and 4.19.

	Mean [mGal]	Std.Dev ± [mGal]	Min [mGal]	Max [mGal]
Line 1	3.1	8.2	-13.7	18.3
Line 2	0.3	4.4	-7.8	13.4
Line 3	20.2	15.1	-1.2	43.7
Line 4	5.0	9.5	-12.5	19.9
Line 5	8.9	6.5	-16.2	16.8
Line 6	14.7	12.1	-9.2	37.7
Line 7	-4.2	9.5	-17.8	14.6
Line 8	-2.1	11.4	-26.8	14.9
Line 9	19.1	10.4	1.6	39.3
Line 10	-18.3	19.9	-46.6	21.3
Line 11	3.0	16.9	-49.4	20.9

Table 4.8: Differences between simulated crossover-adjusted north gravity disturbances and NIMA control data.

	Mean [mGal]	Std.Dev ± [mGal]	Min [mGal]	Max [mGal]
Line 1	-7.5	5.1	-20.4	0.8
Line 2	20.5	6.6	-3.8	30.6
Line 3	-5.1	5.4	-15.9	5.4
Line 4	15.1	8.3	-0.5	30.3
Line 5	5.1	13.1	-17.0	41.3
Line 6	26.9	7.2	-2.0	40.0
Line 7	2.3	13.9	-21.8	31.8
Line 8	22.4	8.9	-2.6	43.5
Line 9	-3.1	11.8	-22.6	22.1
Line 10	21.4	6.9	-2.2	33.7
Line 11	0.4	10.1	-26.2	12.2

Table 4.9: Differences between simulated crossover-adjusted east gravity disturbances and NIMA control data.

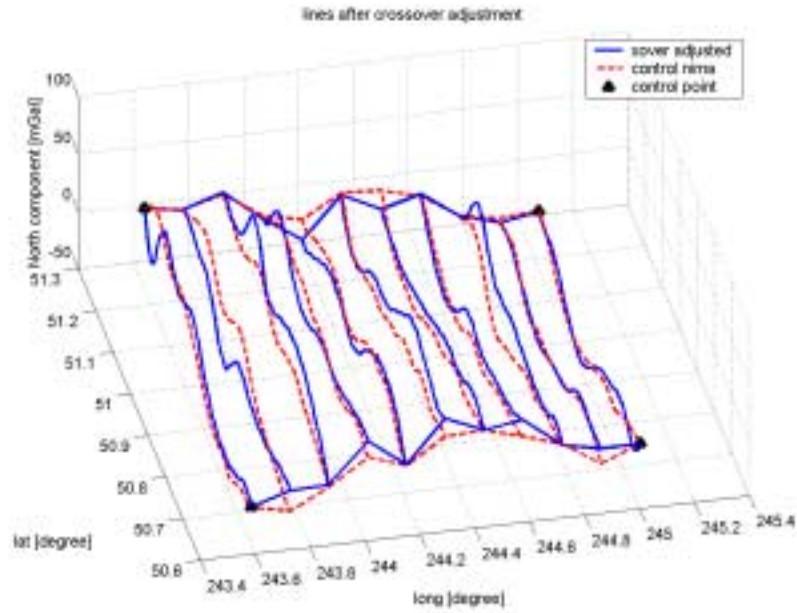


Figure 4.18: Crossover adjusted lines by using simulated cross tracks versus NIMA control for the North component of the gravity disturbance vector

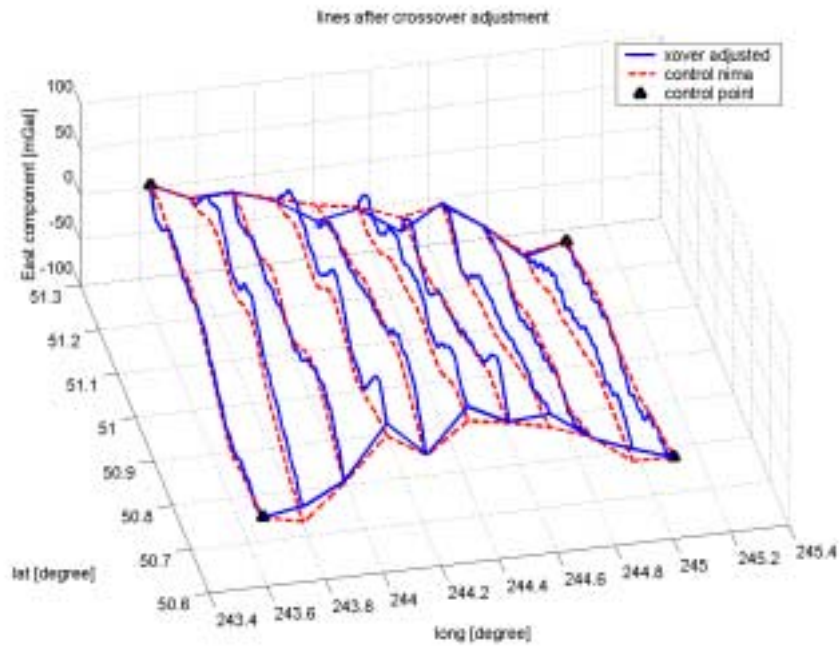


Figure 4.19: Crossover adjusted lines by using simulated cross tracks versus NIMA control for the East component of the gravity disturbance vector

We can observe that the results of the simulated adjustment for the horizontal components using minimal control are similar to those based on total control. It is difficult though, to really quantify the effect of the crossover adjustment with simulated data. At least it allows us to show the procedure to follow in the case of minimal control.

The term “full control”, in our context, refers to the case when we use control at both ends of each line; and minimal control refers to the case of introducing the minimal amount of control points.

CHAPTER 5

GEOID COMPUTATION/ESTIMATION

5.1 Introduction

Different approaches for geoid computation (resp. estimation) have been introduced in the previous chapters. In this chapter the different methodologies for computing the geoid, according to different types of data, are implemented. The geoid is computed by the use of the vertical component (VC), the horizontal components (HC), and a combination of the three components (3C) of the gravity disturbance vector. The results of these computations are presented along with a description of some additional procedures such as the determination of the parameters of the covariance function to be used in the LSC adjustment, and the application of the wave correlation filter (WCF) for the case of the 3C geoid. The resulting geoid estimation from these different methods is compared to the Canadian geoid. The Canadian geoid is computed via the GPS-H 2.1 software of the Geodetic Survey Division of the Canadian Department of Natural Resources. This geoid is based on the Canadian geoid 2000 (CGG2000) (Véronneau, 2001), adjusted to the Canadian primary vertical control (CGVD28).

5.2 The geoid from the down component of the gravity disturbance vector

The geoid is computed by using information for the down component of the gravity vector by means of Hotine's integral. Helmert's condensation method is applied by using the procedure explained in Chapter 3. Contrary to the traditional approach, where the corrections due to the compensation of the masses are applied to the gravity disturbances, Helmert's condensation method is here applied directly to the disturbing potential after downward continuation to the terrain. This is done with the idea that, having the disturbing potential from different sources, the Helmert's correction can be applied to the different and combined solutions as will be shown later on. The results at flight height, along with the reductions to the geoid, are presented to evaluate the effectiveness of the downward continuation and Helmert's condensation approaches. The computations are done first for the end-matched lines with control information provided by NIMA (that is, adjusting to the two end-points for each line). Next, the results from the cross-over adjustment with minimal control as explained in Chapter 4 are presented.

Prior to the computations a grid of points for use in Hotine's integral is generated. The estimated gravity disturbances from the original lines end-matched by NIMA control are interpolated onto a 22x11 grid, with 22 points in the North-South direction and 11 points in the East-West direction consistent with the 11 lines in the area of study. For the case of the cross-over adjusted data, a grid of 30x11 was generated. This grid contains

more points since these North-South lines are longer than the end-matched lines. The disturbing potential is computed at flight altitude and then divided by normal gravity as a first estimate of the Canadian geoid. Next the disturbing potential is downward continued and the masses are removed and restored according to Helmert's condensation as explained in section 2.7.3. Helmert's correction is applied directly to the disturbing potential. Then this final estimate of the geoid is compared to the Canadian geoid.

5.2.1 Geoid estimation using NIMA full control for the vertical component

The results coming from Hotine's integral at height flight using the end-matched lines can be observed in Table 5.1. Statistics for the differences with respect to the Canadian geoid are presented. In this table the comparison is arranged line by line, and the comparison is done for every point of each line. In this way the results can be compared to those from the HC geoid, which is computed for each line. In Figure 5.1, a graphic comparison of both surfaces and their difference is shown.

Line	Mean [m]	St dev \pm [m]	Min [m]	Max [m]
1	-0.536	0.177	-0.760	-0.235
2	-0.679	0.048	-0.758	-0.593
3	-0.841	0.028	-0.914	-0.803
4	-0.854	0.062	-0.951	-0.713
5	-0.905	0.135	-1.053	-0.592
6	-0.910	0.131	-1.07	-0.592
7	-0.905	0.133	-1.105	-0.645
8	-0.938	0.110	-1.127	-0.674
9	-0.999	0.112	-1.132	-0.694
10	-1.090	0.066	-1.219	-0.995
11	-1.183	0.225	-1.521	-0.933

Table 5.1 Results for the VC height anomaly using Hotine's integral in the 22x11 grid of the differences with respect to Canadian geoid. EGM96 up to degree 360 is used.

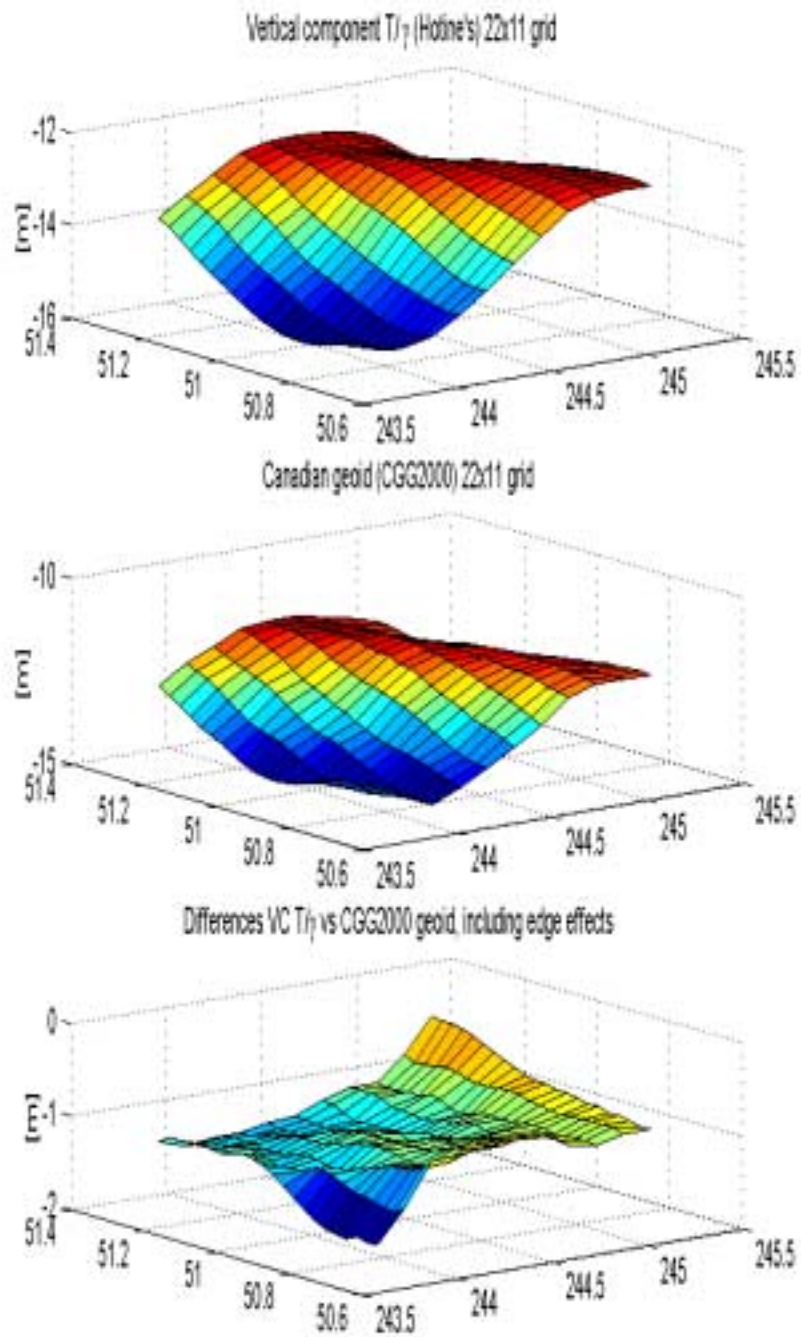


Figure 5.1: Vertical component height anomaly versus Canadian geoid and their difference for the 22x11 grid.

We can observe differences in the order of 3 cm up to 22 cm. Notice, however, that the larger differences are in line 1 and in line 11, which indicates that there are edge effects affecting the result. In order to reduce the effect of the north-south edges, 4 points are eliminated at both ends of each line and the statistics for the differences are re-calculated and given Table 5.2:

Line	Mean [m]	St dev [m]	Min [m]	Max [m]
1	-0.560	0.119	-0.720	-0.314
2	-0.680	0.044	-0.752	-0.599
3	-0.843	0.032	-0.914	-0.803
4	-0.885	0.045	-0.951	-0.812
5	-0.951	0.086	-1.046	-0.790
6	-0.925	0.084	-1.060	-0.771
7	-0.908	0.072	-1.069	-0.810
8	-0.931	0.062	-1.042	-0.845
9	-1.029	0.065	-1.099	-0.875
10	-1.053	0.046	-1.143	-0.995
11	-1.145	0.205	-1.504	-0.933

Table 5.2: Results for the VC T/γ using Hotine's integral in the 22x11 grid of the differences with respect to Canadian geoid. EGM96 up to degree 360 is used. North-south edges have been removed

We can see an improvement in all the lines. However lines 1 and 11 still show large differences that are not present in the other lines. This is due to the fact that those lines are at the east-west edges of the area; therefore they would have to be eliminated and the useful area would be reduced to the 9 internal lines, where the computed geoid shows accuracies in the range of 3-9 cm. We also observe biases in the range of -0.6 to -1.1 m for all the lines. These biases may be attributed, in part, to the fact that the Canadian geoid is not a gravimetric geoid. It has been transformed to the local Canadian datum CGVD28. Notice that the biases are different for the lines increasing in the east-west direction. This may indicate a slope between both geoids. These biases are consistent, at least in sign, with the bias found by Véronneau (2001), between the CGG2000 geoid and the GPS on benchmarks derived geoid.

The use of EGM96 contributes to the low frequency part of the estimated geoid. The difference between the final estimated geoid and EGM96 is in the order of 15 cm with deviations of ± 35 cm.

Next, the results coming from the determination of the geoid by using Helmert's condensation method as described by equation (2.45) are presented. For the downward continuation the iterative procedure in spherical approximation described in section 3.6.1

was applied. We used the spherical approximation since for the set of real data we had problems in the convergence using the planar approximation. The net effect on the disturbing potential given by equation (2.58) in planar approximation is computed, and the comparison with the Canadian geoid can be observed in Table 5.3. The north-south edges have been removed. A low pass filter was applied in order to remove high frequencies present in the net effect on the potential. The downward continuation of the effect of the topography at points on the terrain, $D(-\delta V_{\text{Topo}}(P))$ in equation (2.51), showed no improvement on the final geoid. Actually, the results were poorer than those computed without this correction. The argument used for the downward continuation was the disturbing potential at flight altitude.

Line	Mean [m]	St dev ± [m]	Min [m]	Max [m]
1	-0.412	0.104	-0.593	-0.237
2	-0.607	0.045	-0.692	-0.554
3	-0.816	0.032	-0.876	-0.749
4	-0.894	0.040	-0.947	-0.827
5	-0.963	0.068	-1.050	-0.817
6	-0.943	0.063	-1.078	-0.868
7	-0.943	0.070	-1.070	-0.854
8	-1.035	0.073	-1.146	-0.944
9	-1.144	0.045	-1.211	-1.062
10	-1.220	0.073	-1.371	-1.138
11	-1.355	0.198	-1.662	-1.135

Table 5.3 Results for the VC geoid using Hotine's integral in the 22x11 grid of the differences with respect to Canadian geoid. EGM96 up to degree 360 is used. Downward continuation and Helmert's condensation approach applied to the disturbing potential is included. North-south edges have been removed.

We can observe, from inspecting Tables 5.2 and 5.3, a small improvement in terms of standard deviations over the solution without downward continuation and compensation for the masses. The biases and the minimal and maximum differences are improved slightly. In Figure 5.2 a graphic comparison of the height anomaly at flight height and the geoid reduced by downward continuation and Helmert's condensation method is presented for some lines. We observe that the downward continued lines with Helmert's correction mostly follow more closely the shape of the Canadian geoid than without these corrections.

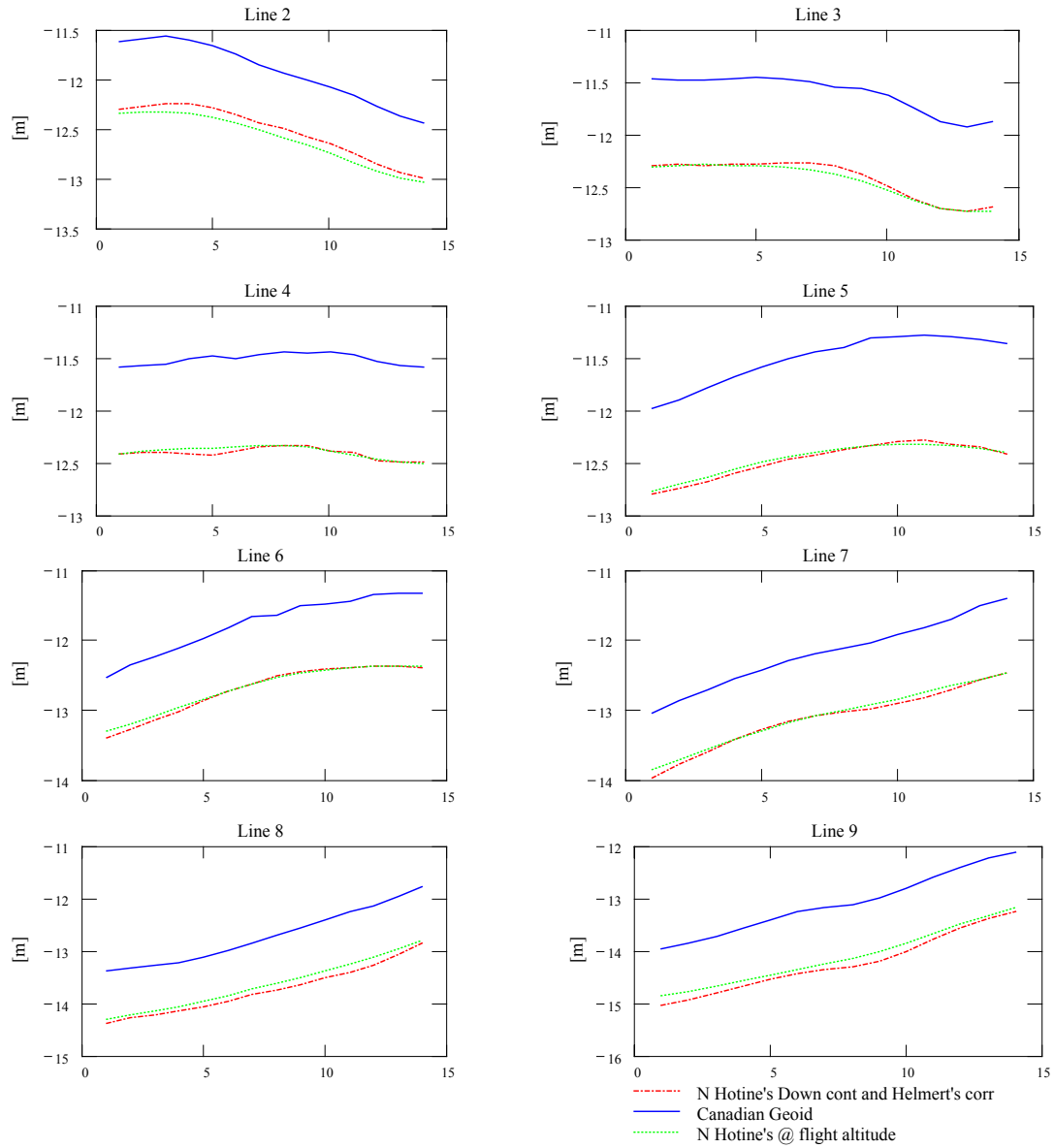


Figure 5.2: Comparison of the VC height anomaly at flight altitude and final VC geoid (corrected by downward continuation and Helmert's condensation) with the Canadian geoid 2000.

5.2.2 Helmert's condensation method applied to the vertical component of the gravity disturbance vector

The geoid was computed by using Helmert's condensation method in the traditional way. The down component of the gravity disturbance vector was corrected by

using equation (2.43). The terrain correction was applied, and the geoid was computed. In Table 5.4 statistics for the differences with respect to the Canadian geoid are presented. The differences with and without the indirect effect are presented. A low pass filter was applied to the indirect effect.

Without indirect effect					With indirect effect (low pass filtered)				
Line	Mean [m]	St dev ± [m]	Min [m]	Max [m]	line	Mean [m]	St dev ± [m]	Min [m]	Max [m]
1	-0.419	0.113	-0.580	-0.189	1	-0.612	0.158	-0.853	-0.303
2	-0.506	0.039	-0.573	-0.444	2	-0.743	0.079	-0.853	-0.594
3	-0.645	0.031	-0.710	-0.608	3	-0.894	0.041	-0.944	-0.794
4	-0.683	0.047	-0.747	-0.610	4	-0.939	0.032	-1.002	-0.888
5	-0.749	0.088	-0.852	-0.589	5	-1.019	0.099	-1.133	-0.829
6	-0.720	0.089	-0.871	-0.564	6	-0.981	0.118	-1.129	-0.732
7	-0.697	0.082	-0.880	-0.592	7	-0.920	0.096	-1.156	-0.791
8	-0.710	0.076	-0.850	-0.610	8	-0.898	0.090	-1.098	-0.786
9	-0.807	0.072	-0.898	-0.647	9	-0.968	0.114	-1.122	-0.727
10	-0.836	0.046	-0.931	-0.765	10	-0.974	0.060	-1.077	-0.862
11	-0.946	0.204	-1.309	-0.729	11	-1.092	0.221	-1.527	-0.866

Table 5.4: Results for the VC geoid using Hotine's integral in the 22x11 grid of the differences with respect to Canadian geoid. EGM96 up to degree 360 is used. Helmert's condensation approach applied to the gravity disturbances. Results with and without including the indirect effect. North-south edges have been removed.

From this table we see that the application of Helmert's correction directly to potential provides similar results to those from the traditional method. In fact, we observe a slight improvement of the results for the VC geoid using the corrections directly to disturbing potential. We can also see that with the inclusion of the indirect effect we get worse results.

5.2.3 Geoid estimation using adjusted crossovers for the vertical component.

The geoid was computed again using the VC, but this time the crossover adjusted lines are used in Hotine's integral. The results are presented in Table 5.5. A comparison with the full control VC geoid is shown to give an idea of the differences.

Full control VC					Cross-over adjusted VC				
Line	Mean [m]	St dev \pm [m]	Min [m]	Max [m]	line	Mean [m]	St dev \pm [m]	Min [m]	Max [m]
1	-0.504	0.225	-0.816	-0.177	1	-0.373	0.250	-0.716	-0.011
2	-0.658	0.142	-0.847	-0.476	2	-0.487	0.213	-0.806	-0.221
3	-0.804	0.073	-0.899	-0.681	3	-0.610	0.192	-0.872	-0.328
4	-0.830	0.053	-0.922	-0.742	4	-0.631	0.190	-0.878	-0.345
5	-0.863	0.119	-1.012	-0.573	5	-0.684	0.153	-0.851	-0.417
6	-0.917	0.124	-1.049	-0.624	6	-0.738	0.097	-0.915	-0.571
7	-0.968	0.125	-1.142	-0.629	7	-0.808	0.116	-1.054	-0.639
8	-0.979	0.121	-1.176	-0.716	8	-0.893	0.106	-1.097	-0.742
9	-1.083	0.074	-1.281	-0.947	9	-1.017	0.167	-1.387	-0.745
10	-1.166	0.172	-1.467	-0.984	10	-1.112	0.238	-1.510	-0.850
11	-1.190	0.303	-1.614	-0.587	11	-1.131	0.331	-1.584	-0.762

Table 5.5: Results of the differences (30x11 grid) with respect to Canadian geoid for the full control and crossover VC. EGM96 up to degree 360 is used. Edge effects are still included.

In Table 5.5 the same results after removing the north-south edges are presented. And as before, 4 points in the north and south ends of the lines are removed from the results.

Full control VC					Cross-over adjusted VC				
Line	Mean [m]	St dev \pm [m]	Min [m]	Max [m]	Line	Mean [m]	St dev \pm [m]	Min [m]	Max [m]
1	-0.522	0.232	-0.816	-0.177	1	-0.384	0.255	-0.716	-0.011
2	-0.658	0.126	-0.840	-0.481	2	-0.479	0.186	-0.756	-0.226
3	-0.812	0.072	-0.899	-0.681	3	-0.608	0.176	-0.864	-0.328
4	-0.839	0.056	-0.922	-0.742	4	-0.630	0.184	-0.878	-0.345
5	-0.897	0.086	-1.012	-0.693	5	-0.708	0.146	-0.851	-0.417
6	-0.945	0.088	-1.049	-0.739	6	-0.757	0.093	-0.915	-0.606
7	-0.978	0.097	-1.142	-0.837	7	-0.809	0.110	-1.054	-0.639
8	-0.998	0.09	-1.176	-0.852	8	-0.908	0.108	-1.097	-0.778
9	-1.064	0.038	-1.147	-0.988	9	-0.997	0.104	-1.223	-0.841
10	-1.140	0.149	-1.436	-0.984	10	-1.085	0.205	-1.477	-0.879
11	-1.177	0.302	-1.614	-0.871	11	-1.117	0.327	-1.584	-0.778

Table 5.6: Results in the 30x11 grid of the differences with respect to Canadian geoid. For the VC with full control, and cross-over VC. EGM96 up to degree 360 is used. Edge effects have been removed.

As in the previous section, we can observe an improvement in the quality of the lines once edges are removed. Again, lines 1 and 11 show the worst results. We can also observe that the crossover solution presents large differences in terms of standard deviations, in the order of 10 cm more than full control.

Helmert's condensation scheme is applied also to these estimates, and the final results are presented in Table 5.7 for both the full control and the cross-over solution.

Full control VC					Cross-over adjusted VC				
Line	Mean [m]	St dev ± [m]	Min [m]	Max [m]	Line	Mean [m]	St dev ± [m]	Min [m]	Max [m]
1	-0.147	0.052	-0.226	-0.064	1	-0.547	0.090	-0.664	-0.370
2	-0.266	0.061	-0.366	-0.178	2	-0.524	0.103	-0.669	-0.373
3	-0.274	0.083	-0.413	-0.137	3	-0.618	0.116	-0.804	-0.414
4	-0.391	0.046	-0.464	-0.295	4	-0.643	0.109	-0.818	-0.483
5	-0.488	0.028	-0.532	-0.440	5	-0.726	0.107	-0.882	-0.551
6	-0.604	0.054	-0.678	-0.496	6	-0.761	0.158	-0.981	-0.517
7	-0.709	0.069	-0.801	-0.600	7	-0.866	0.191	-1.142	-0.624
8	-0.853	0.033	-0.916	-0.809	8	-1.066	0.149	-1.285	-0.808
9	-1.045	0.057	-1.160	-0.930	9	-1.234	0.130	-1.468	-1.018
10	-1.208	0.159	-1.422	-0.981	10	-1.359	0.186	-1.621	-1.088
11	-1.313	0.202	-1.522	-0.910	11	-1.396	0.218	-1.600	-0.983

Table 5.7: Results in the 30x11 grid of the differences with respect to Canadian geoid. For the VC with full control, and cross-over VC. EGM96 up to degree 360 is used. Downward continuation and Helmert's condensation approach applied to the disturbing potential is included. Edge effects have been removed.

The same situation as before is observed here. The results show some improvement when the downward continuation and Helmert's condensation approach is used.

5.3 The geoid from the horizontal components of the gravity disturbance vector

In this section the geoid is computed by the use of the line integral method described in section 2.4. Two sets of results are presented. First, the geoid is computed by the use of the fully controlled lines with NIMA control for the case of the horizontal components (HC), and with full end-point control on the disturbing potential obtained from the Canadian geoid. This solution provides the geoid for the case of having full control in the area of study. Recognizing that this is not always possible, or not possible at all depending on the area of the world where we are implementing this methodology, a

second computation is performed with the simulated crossover results for the HC and the use of minimal control from the Canadian geoid as will be explained later.

5.3.1 The geoid from the horizontal components using total control

The geoid is computed using the end-matched horizontal components of the gravity disturbance vector. The data on the lines are again interpolated onto a 22x11 grid and the disturbing potential is computed at flight altitude. These results, being differences in potential, are then end-matched to the Canadian geoid for all the lines. Since we already match the resulting geoid with the real geoid, we observe that the downward continuation does not produce any improvement on the geoid and it is not applied to the results. The differences with respect to the Canadian geoid are computed and the results are shown in Table 5.8:

Line	Mean [m]	St.dev±[m]	Min [m]	Max [m]
1	-0.012	0.045	-0.088	0.066
2	0.006	0.027	-0.037	0.069
3	-0.126	0.169	-0.351	0.172
4	0.038	0.054	-0.049	0.138
5	-0.129	0.084	-0.237	0.033
6	0.021	0.055	-0.105	0.082
7	0.064	0.064	-0.032	0.157
8	0.026	0.112	-0.165	0.200
9	0.058	0.046	-0.027	0.146
10	0.195	0.247	-0.172	0.577
11	0.279	0.196	-0.006	0.576

Table 5.8: Differences of HC T/γ with the Canadian geoid at flight altitude. Lines are end- matched with the Canadian geoid.

Next, 4 points at the north and south edges are removed from each line. This is done not because we expect edge effect in the computations as it happens with the VC geoid, but because of the fact that we can expect the end of each line to be still affected by residual errors as introduced at each 180° turn of the plane. The results of the comparison to the Canadian geoid can be observed in Table 5.9.

Line	Mean [m]	St dev \pm [m]	Min [m]	Max [m]
1	-0.013	0.038	-0.088	0.045
2	0.005	0.032	-0.037	0.069
3	-0.202	0.149	-0.351	0.107
4	0.045	0.061	-0.049	0.138
5	-0.181	0.044	-0.237	-0.074
6	0.039	0.044	-0.061	0.082
7	0.088	0.058	-0.025	0.157
8	0.048	0.129	-0.165	0.200
9	0.081	0.031	0.033	0.146
10	0.291	0.231	-0.115	0.577
11	0.372	0.160	0.070	0.576

Table 5.9: Differences of HC T/γ with the Canadian geoid at flight altitude. Lines are end-matched with the Canadian geoid. North and south edges have been removed.

A comparison with the results coming from the VC geoid (see Table 5.3) shows that the relative HC geoid is accurate to the same order of magnitude, with improvement over the VC geoid for some lines. However, the HC geoid is highly dependent on control for each line, but does not suffer from edge effects as the VC geoid. In the next section the use of minimal control for the HC geoid is introduced.

In Figure No. 5.3, the differences of disturbing potential from HC divided by normal gravity compared to the Canadian geoid for both cases, with and without north and south edges, is presented.

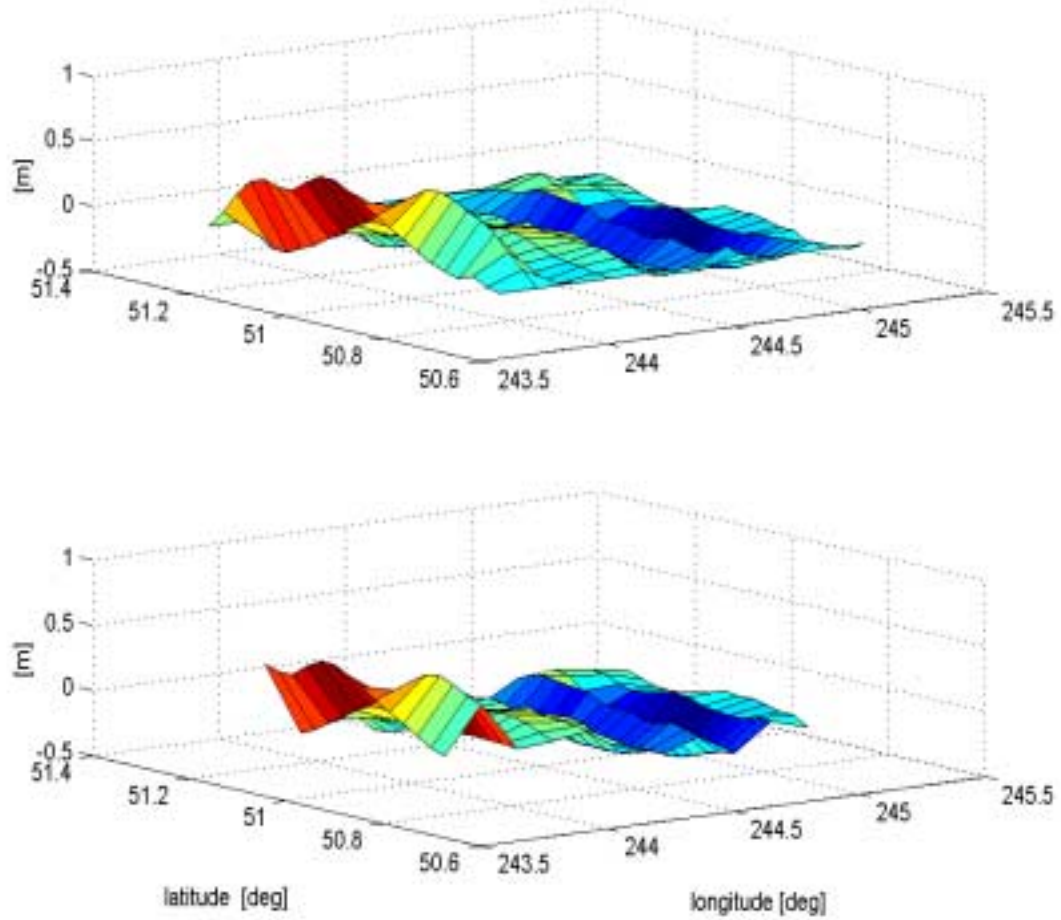


Figure 5.3: Differences in height anomaly from HC and Canadian geoid with (top) and without (bottom) north and south edges.

5.3.2 The geoid from the horizontal components using minimal control

The HC geoid is computed by the use of the simulated crossover-adjusted lines with only 4 points as control as explained in the previous chapter. In addition to computing the disturbing potential from the north-south lines as done in 5.3.1, the disturbing potential was also computed in the east-west directions with the simulated crossover-adjusted north and south crossing tracks. Once the disturbing potential is computed from the two crossing lines, they are end-matched to the Canadian geoid. All

the remaining north-south lines are now end matched to the two crossing lines, in this way referring the whole geoid to the four points used as control for the crossing lines. A comparison to the Canadian geoid is made and the results can be observed in Table 5.10. In Table 5.11 the result with the north-south edges removed are presented.

Line	Mean [m]	St dev \pm [m]	Min [m]	Max [m]
1	-0.013	0.045	-0.087	0.065
2	0.079	0.070	-0.117	0.159
3	-0.200	0.143	-0.395	0.070
4	-0.005	0.079	-0.237	0.085
5	-0.035	0.114	-0.205	0.214
6	0.094	0.106	-0.202	0.236
7	0.178	0.163	-0.142	0.361
8	0.166	0.198	-0.124	0.425
9	0.173	0.086	-0.036	0.266
10	0.316	0.294	-0.135	0.748
11	0.276	0.199	-0.015	0.574

Table 5.10: Differences of HC T/ γ with the Canadian geoid at flight altitude. Lines were end-matched with the Canadian geoid.

Line	Mean [m]	St dev \pm [m]	Min [m]	Max [m]
1	-0.013	0.038	-0.087	0.046
2	0.106	0.032	0.052	0.159
3	-0.273	0.112	-0.395	-0.072
4	0.022	0.030	-0.046	0.063
5	-0.057	0.078	-0.144	0.085
6	0.145	0.055	0.044	0.236
7	0.237	0.121	-0.003	0.361
8	0.218	0.190	-0.124	0.425
9	0.194	0.063	0.090	0.266
10	0.444	0.252	-0.027	0.748
11	0.369	0.162	0.063	0.574

Table 5.11: Differences of HC T/ γ with the Canadian geoid at flight altitude. Lines are end-matched with the Canadian geoid. North and south edges have been removed.

These results are similar in behavior for all the lines to the case of full control. Some of the lines present larger errors, but we have to keep in mind that, in addition to errors coming from the north-south lines we now introduce errors coming from the crossing lines that are used to refer all the lines to the Canadian geoid. The standard deviations in this case are in the order of 3 cm to 12 cm for most of the lines. The worst case is line 10 with a standard deviation of 25 cm, but this line also shows standard deviation of 23 cm for the case of full control. In view of these results, we think we have succeeded in showing the procedure to follow when only minimal control exists in the area.

5.4 The geoid from both the horizontal components and the downward component of the gravity disturbance vector

It might be anticipated that utilization of the full information contained in the gravity vector could improve the determination of the geoid. In a first attempt least squares collocation is applied which is known to be a useful tool for combining data coming from different sources. A local homeogram is determined and used for the adjustment. A second approach is also attempted and combines the VC and the HC geoids by the use of a wave correlation filter (WCF). The results of these estimation experiments are presented next.

5.4.1 The geoid by the use of least squares collocation (LSC)

The disturbing potential at altitude is computed by combining the three components of the gravity disturbance vector. In order to do so, Least Squares Collocation (LSC) is implemented, in this case, by the use of the homeogram instead of the covariance function as explained at the end of section (3.5). First, a local homeogram, by the use of the increments of the disturbing potential according to Geoid99 by NGS (on a grid of 2'x2') with respect to EGM96 was computed in the area of interest. Then an isotropic homeogram was obtained by the use of equation (3.20). The value for the parameters σ^2 and α were empirically determined by visual inspection of the isotropic homeogram. The resulting homeogram function to be used in LSC is shown in Figure No. 5.4 and equation (5.1):

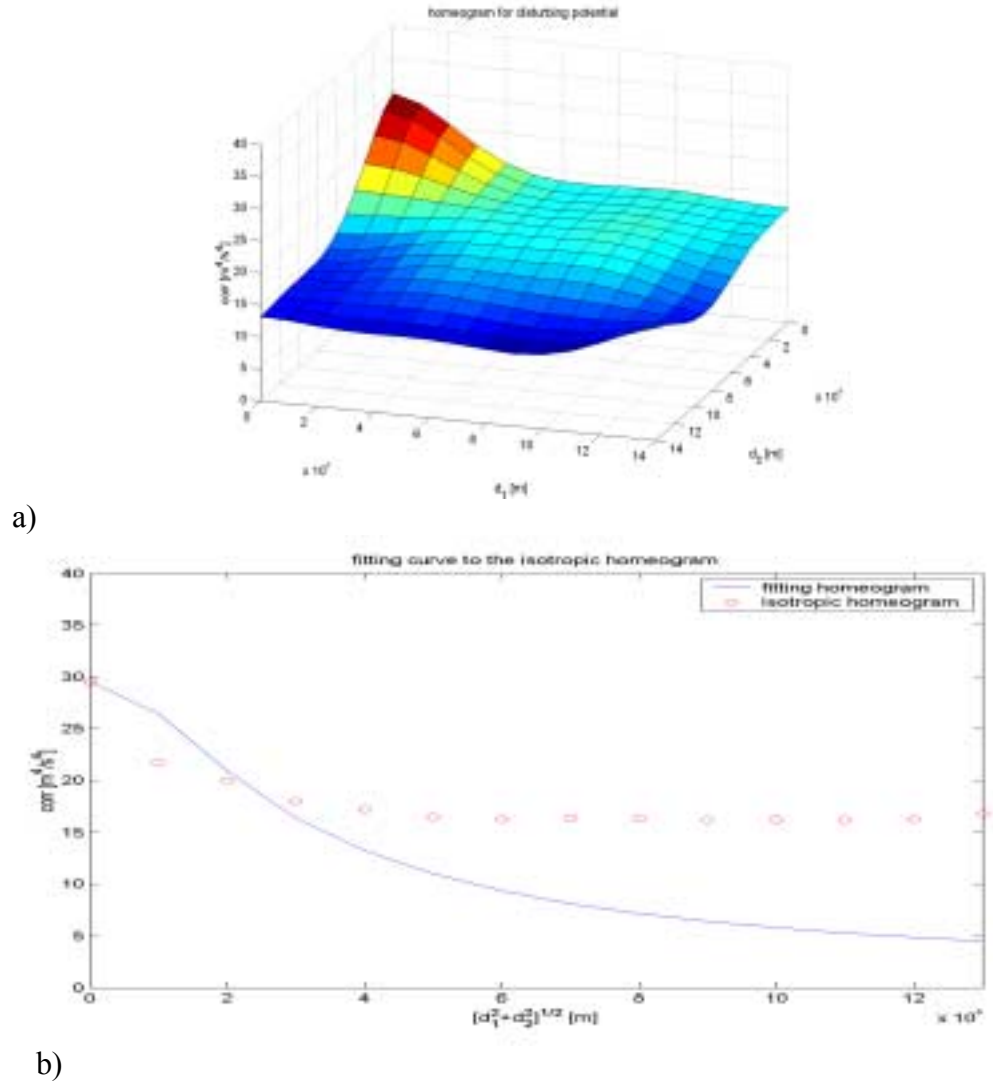


Figure 5.4: a) Homeogram, and b) fitting curve to the isotropic homeogram

$$C(d_1, d_2, d_3) = \frac{29.559}{\sqrt{(1 + 0.5 \times 10^{-4} d_3)^2 + 0.5^2 \times 10^{-10} (d_1^2 + d_2^2)}} \quad [\text{m}^4/\text{s}^4]. \quad (5.1)$$

with $d_3 = z_1 + z_2$, in our case $d_3 = 0$.

The apparent poor fit to the isotropic homeogram is necessary because the homeogram for the disturbing potential does not de-correlate fast enough within the area considered for its determination, and, anyway, the homeogram for the larger shift distance is not well estimated from the limited data.

The data used for LSC are the NIMA end-matched vertical and horizontal components of the gravity disturbance vector on the 22x11 grid. For the computations we first removed modeled components of the gravity disturbances according to EGM96 from the observed components. Then the incremental disturbing potential was computed, and the modeled disturbing potential according to EGM96 was restored as follows (See equation (3.21)):

$$\tilde{\mathbf{s}} = s_{\text{EGM96}} + \tilde{\chi}^T (\mathbf{y} - \mathbf{y}_{\text{EGM96}}), \quad (5.2)$$

where s_{EGM96} and $\mathbf{y}_{\text{EGM96}}$ are the modeled disturbing potential and components of the gravity vector respectively, for the area of interest.

The data were arranged according to the procedure explained at the beginning of section 3.5. The respective homeograms were computed by a subroutine, provided by C. Jekeli, which computes the elements of the homeogram according to equations (5.1) and those given in section 2.5.2.2. For the variances of the noise we assumed the vertical component to have a variance of $(4 \text{ mGal})^2$ and the horizontal components one of $(20 \text{ mGal})^2$, without correlations. These values were assigned according to the observed accuracies with respect to NIMA control see Tables (4.4 to 4.6).

The results of the predicted disturbing potential at flight altitude scaled by $1/\gamma$ are compared to the Canadian geoid. Statistics for these differences, with the north-south edges removed, are shown in Table 5.12:

Line	Mean [m]	St dev \pm [m]	Min [m]	Max [m]
1	-0.632	0.185	-0.918	-0.289
2	-0.843	0.147	-1.048	-0.583
3	-0.998	0.082	-1.111	-0.842
4	-1.095	0.064	-1.174	-0.977
5	-1.192	0.030	-1.233	-1.120
6	-1.216	0.032	-1.279	-1.150
7	-1.230	0.039	-1.273	-1.133
8	-1.249	0.036	-1.302	-1.181
9	-1.261	0.036	-1.313	-1.165
10	-1.248	0.038	-1.316	-1.199
11	-1.259	0.232	-1.657	-1.023

Table 5.12: Differences of the LSC 3C T/ γ with respect to the Canadian geoid, at flight height. North-south edges have been removed

If we compare these results to those coming from the VC computations (see Table 5.2), they show an improvement for some lines, in terms of standard deviations. Compare lines 5 to 10 where the results from LSC are better than those from the Hotine's integral.

We also computed the disturbing potential by LSC but using only the vertical component, and in Table 5.13 statistics are given for the differences with respect to the Canadian geoid, with the same noise as before (4 mGal)².

Line	Mean [m]	St dev ± [m]	Min [m]	Max [m]
1	-0.408	0.060	-0.504	-0.277
2	-0.530	0.058	-0.614	0.422
3	-0.634	0.024	-0.674	-0.580
4	-0.699	0.019	-0.733	-0.670
5	-0.787	0.031	-0.829	-0.731
6	-0.814	0.038	-0.871	-0.730
7	-0.843	0.056	-0.935	-0.739
8	-0.889	0.059	-0.975	-0.804
9	-0.921	0.054	-0.994	-0.799
10	-0.952	0.038	-1.009	-0.884
11	-1.036	0.097	-1.194	-0.912

Table 5.13: Differences of the LSC VC T/γ with respect to the Canadian geoid, at flight height. North-south edges have been removed.

We can observe that the estimates coming from only the vertical component are better than when including the three components for almost all lines, in terms of standard deviations. Exceptions are lines 7,8, and 9 where the results coming from the combination of the three components are better, and lines 5 and 10 with similar results for both cases. These results can be attributed to the fact that the horizontal components of the gravity disturbance vector are not as well determined as the vertical component. By improving the quality of the horizontal components we may expect for better results when combining the three components.

On the other hand, the results from LSC with the vertical component are better than those coming from the use of VC by Hotine's integral (compare Table 5.13 to 5.2). This suggests that the homeogram model reflects appropriately the correlation between the disturbing potential and the vertical component.

5.4.2 The geoid by the use of a wave correlation filter (WCF)

In an attempt to improve the geoid determination, the HC geoid is combined with the VC geoid by wave-correlating the estimates of both. The WCF compares two signals

of the same object in the frequency domain. Those spectral components that are highly correlated at a particular frequency are retained, while those that are not correlated are eliminated. For the estimated geoids at hand, the result is the removal of low frequency trends of the signals. The wave correlation coefficient for two signals x and y is computed as (Von Frese et al., 1997):

$$CC_k = \cos(\Delta\theta_k) = \frac{X_k \bullet Y_k}{|X_k||Y_k|} \quad (5.2)$$

where X_k and Y_k are the corresponding spectral components for x and y at a particular wave number k . These components at a particular wavenumber are regarded as vectors in the complex plane. CC_k is the wave correlation coefficient at a particular wave number k , and $\Delta\theta_k$ is the phase difference between the spectral components X_k and Y_k .

The practical computation of the phase difference can also be done according to:

$$\Delta\theta_k = \theta_x - \theta_y = \arctan\left(\frac{\text{Im}(X_k)}{\text{Re}(X_k)}\right) - \arctan\left(\frac{\text{Im}(Y_k)}{\text{Re}(Y_k)}\right) \quad (5.3)$$

where $\text{Im}(\)$ stands for the imaginary part of the argument inside the brackets, and $\text{Re}(\)$ for the real part.

In order to combine the geoid estimates coming from VC and the HC, the procedure described above was implemented. For this experiment, the crossover-adjusted geoid for the VC was interpolated into a 22x11 grid. This geoid estimate was wave correlated to the minimal control HC geoid (see section 5.3.2) as follows: Every line on each geoid estimate was wave correlated, and at those frequencies showing negative spectral correlation the spectral components were forced to be zero. New geoid estimates are computed in the space domain from the revised spectra, and the final geoid is computed by averaging both wave-correlated geoids. A special case was line 3. The final geoid was a constant centered at the averaged mean of both VC and HC geoid estimates. This means that for line 3 there was no positive correlation at any frequency. In this case, a weighted average of both lines was computed by assigning a larger weight to the VC geoid. This was done since the vertical components of the gravity disturbance vector are better determined than the horizontal components. The results of the comparison with respect to the Canadian geoid can be observed in Tables 5.14 and 5.15. In Figure 5.5 a graphical comparison with the Canadian geoid is shown for some lines.

Line	Mean [m]	St dev \pm [m]	Min [m]	Max [m]
1	-0.204	0.134	-0.394	0.025
2	-0.201	0.065	-0.308	-0.088
3	-0.507	0.120	-0.638	-0.305
4	-0.322	0.065	-0.428	-0.224
5	-0.379	0.046	-0.445	-0.279
6	-0.333	0.043	-0.414	-0.262
7	-0.311	0.073	-0.424	-0.224
8	-0.369	0.092	-0.491	-0.211
9	-0.407	0.026	-0.452	-0.358
10	-0.373	0.145	-0.675	-0.129
11	-0.414	0.242	-0.791	-0.121

Table 5.14: Differences of the 3C WCF correlated T/ γ with the Canadian geoid.

Line	Mean [m]	St dev \pm [m]	Min [m]	Max [m]
1	-0.213	0.088	-0.371	-0.032
2	-0.186	0.060	-0.276	-0.088
3	-0.523	0.103	-0.638	-0.315
4	-0.322	0.076	-0.428	-0.224
5	-0.407	0.023	-0.445	-0.357
6	-0.309	0.029	-0.368	-0.262
7	-0.273	0.050	-0.388	-0.224
8	-0.325	0.084	-0.474	-0.211
9	-0.397	0.023	-0.439	-0.358
10	-0.287	0.095	-0.460	-0.129
11	-0.345	0.212	-0.739	-0.121

Table 5.15: Differences of the 3C WCF T/ γ with the Canadian geoid. North-south effects removed.

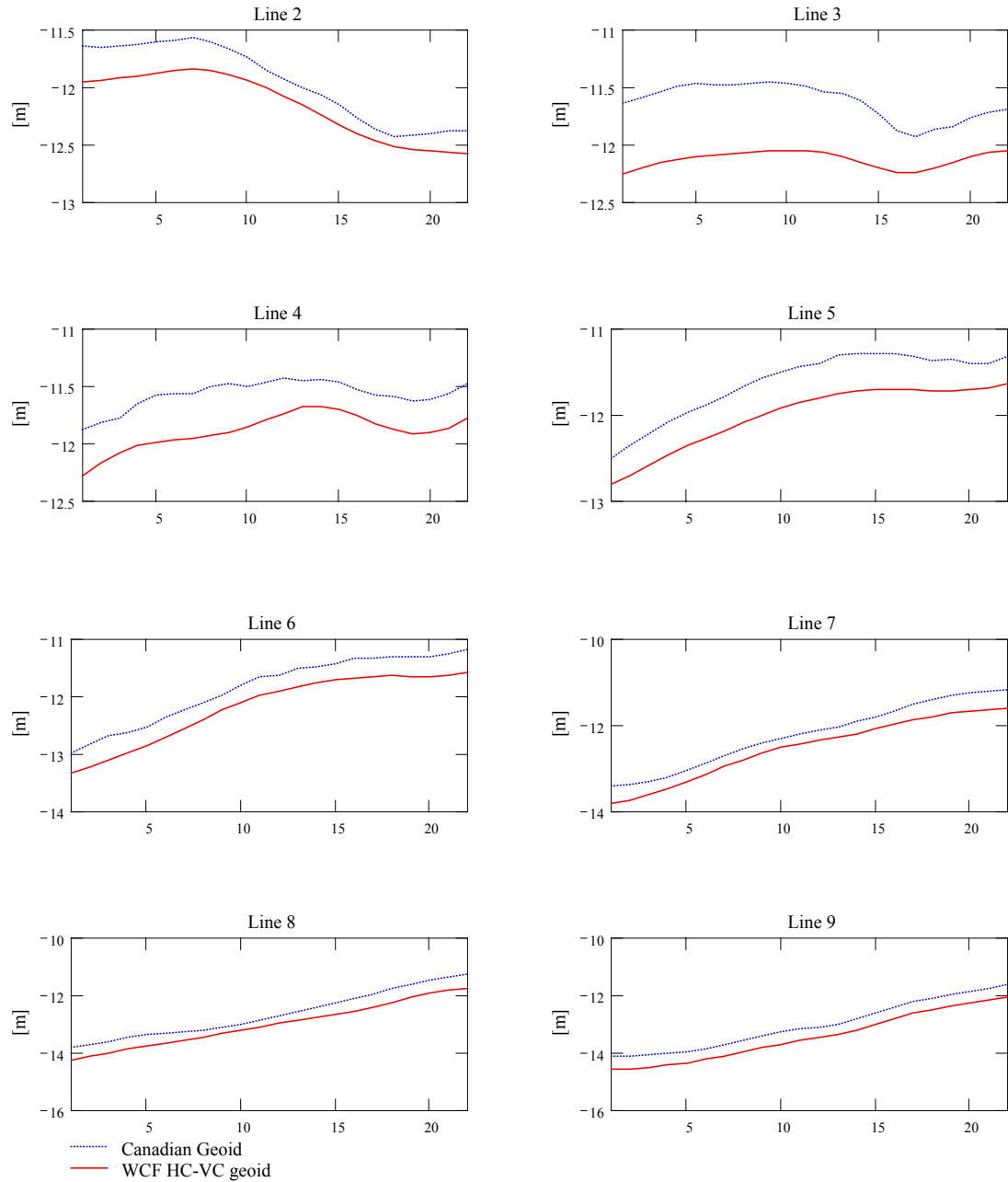


Figure 5.5: Comparison of the WCF 3C geoid to the Canadian geoid

These results show improvement for almost all lines when compared to the resulting geoid from crossover VC on a 22x11 grid. For the case of the HC some lines show improvement, mainly those lines in the central area, implying that edge effects coming from the computations of the VC affect the results. A comparison of the

accuracies of the WCF, the crossover VC geoid, and the HC with minimal control with respect to the Canadian geoid are shown in Table 5.16. The north and south edges have been removed before the comparison.

Line	WCF		crossover Hotine's 22x11		Line integral min control	
	St dev ± [m]	Extrema [m]	St dev ± [m]	Extrema [m]	St dev ± [m]	Extrema [m]
1	0.088	-0.371	0.170	-0.655	0.038	-0.087
2	0.060	-0.276	0.133	-0.660	0.032	-0.117
3	0.103	-0.638	0.116	-0.791	0.112	-0.395
4	0.076	-0.428	0.105	-0.844	0.030	-0.237
5	0.023	-0.445	0.070	-0.848	0.078	0.214
6	0.029	-0.368	0.050	-8.480	0.055	0.236
7	0.050	-0.388	0.059	-0.878	0.121	0.361
8	0.084	-0.474	0.075	-1.054	0.190	0.425
9	0.023	-0.439	0.055	-1.076	0.063	0.266
10	0.095	-0.460	0.104	-1.233	0.252	0.748
11	0.212	-0.739	0.267	-1.540	0.162	0.574

Table 5.16: Accuracies of the 3C WCF, VC and HC geoids with respect to the Canadian geoid. North-south effects have been removed.

CHAPTER 6

CONCLUSION AND RECOMMENDATIONS

In this study the use of the different components of the gravity disturbance vector has been implemented for the determination of the geoid. For obtaining the three components, the method developed by Jekeli and Kwon (2001) has been used. The application of this method provides directly the three components of the gravity vector in an inertial frame; and by rotating these components to a local frame, we are able to use it for geoid computation with a variety of methods. In addition to the computed disturbing potential at flight height, the downward continuation to the terrain by the use of Poisson's iterative formula was implemented. Furthermore, Helmert's condensation method, following the traditional approach (Wang and Rapp, 1990), for the computation of the direct and indirect effects on the potential, due to the removal and restoration of the topography is applied. The respective relation for the computation of the net effect on the potential is derived.

The down component of the gravity disturbance vector, as well as the horizontal components were determined from airborne test data provided by the University of Calgary. The accuracy of the down components when compared to control data provided by NIMA is, in general, twice as good as for the horizontal components. Moreover the components are noticeably affected by the dynamics of the airplane, exhibiting large oscillations when it turns 180° to begin a new track. In this study we were not able to find a solution to this problem, and more research is needed in this direction. The down component, on the other hand, is not affected drastically by the turns and in general, the accuracy is in the 4 mGal range.

One problem we face when working with real data is the lack of control. What should we do if in an area of interest there is a lack of benchmarks and no information about the deflections of the vertical? At least, every country has a vertical reference network, even when the degree of densification is poor, some control can be established. Scarce information about deflections of the vertical is also available, kept by national cartographic or geographic institutes. This information can be valuable for controlling the data collected by airborne gravimetry. This is why it is important to study the crossover adjustment of the observations by the use of minimal control. Before an airborne campaign is carried out, good planning considering the location of the existing control has to be done. We performed crossover adjustment for the down component, keeping in mind the necessity of minimal control. Even when the results are not better than those coming from fully controlled lines, the results are encouraging and within the expected accuracies for this type of observation. We feel that, the better the observations are determined, the better the results from the crossover adjustment will be. The use of a crossover adjustment for the horizontal components has to be envisioned in the future, and efforts should be made to improve the accuracies for these components and to eliminate the large oscillations at the turns of the airplane.

For the downward continuation of the disturbing potential we observe that Poisson's integral iterative solution performs better than the gradient method in terms of

standard deviations. Mean differences on the order of 1 cm with standard deviations of 2 cm in terms of geoid undulations can be observed in the simulations when using this method. Therefore, the iterative solution was used and it is recommended for the determination of the disturbing potential at terrain and boundary surface level.

An improvement in the local geoid determination was noticed when the downward continuation was performed, but complemented by the application of Helmert's condensation approach directly to the disturbing potential. The downward continuation of the effect of the topography on the potential, $D(-\delta V_{\text{Topo}}(P))$ in equation (2.51), was neglected since its application did not improve the results of the final geoid. The results of applying Helmert's correction directly to the disturbing potential are comparable with those of the traditional method, where Helmert's correction is applied to the down component of the gravity disturbance vector.

Regarding the method of computing the geoid by the use of different gravity components, the VC geoid by using Hotine's integral appears to provide the best results, with accuracies on the order of 4 to 12 cm. These are good results if we consider the accuracy of the down component of the gravity disturbance vector. The geoid from crossover-adjusted data shows accuracies on the order of 10 to 15 cm. These results can be enhanced by improving the determination of the gravity disturbance components, especially for the crossing lines. On the other hand the HC geoid provides similar results to those coming from the VC geoid, the former relies on control points for the final geoid, but is not affected by edge effects as much as the VC geoid. If we turn now to the determination of the geoid by the integration of the three components via LSC, we notice improved results for about half of the lines when compared to the results from the vertical component by the use of Hotine's integral. Comparing the 3C-LSC to the results for the line integral, LSC provides in general better results than those from the HC results. On the other hand, the results from LSC using only the vertical component are better than those coming from the use of Hotine's integral. Applying LSC to all three components of the gravity disturbance vector should be superior to all other methods provided the quality of the estimates for the horizontal components is improved, and the covariance model is adequate. Alternatively, for the available data, the combination of the VC and HC geoid estimates by the use of a wave correlation filter shows some promising results for improving the geoid. The accuracies are comparable to those from the VC geoid, but are improved for some of the lines. We think that the determination of the geoid by the use of this methodology could be further improved if we are able to measure the horizontal components of the gravity vector at least as accurately as the vertical component.

Bibliography

- Bayoud, F. and Sideris, G. (2001) Geoid determination from airborne gravity data using different filtering frequencies and DTM resolutions. **Proceeding of IAG 2001**, Budapest, September 2001.
- Bruton, A. B. (2000) Improving the accuracy and resolution of SINS/DGPS Airborne Gravimetry., Doctoral Dissertation, Dept. of Geomatics Engineering. The University of Calgary, Calgary, Alberta, Canada.
- Forsberg, R., Olesen A., Bastos, L., Gidskehaug, A., Meyer, U., and Timmen, L. (2000) Airborne geoid determination. **Earth Planes Space**, 52, 863-866.
- Garcia, R (2000) Local geoid determination from GRACE mission. Doctoral Dissertation, Dept. of Geodetic Science and Surveying, The Ohio State University, Columbus Ohio, USA.
- Haagmans, R., de Min, E., and von Gelderen, M. (1993) Fast evaluation of convolution integrals on the sphere using 1D FFT, and a comparison with existing methods for Stokes' integral. **Manuscripta Geodaetica**, 18, 227-241.
- Heiskanen, W. and Moritz, H. (1967) **Physical geodesy**; (reprint 1987). Institute of Physical Geodesy; Technical University; Graz, Austria.
- Hotine, M. (1969) **Mathematical Geodesy**. ESSA Monograph No.2, US Dept. of Commerce, Washington, DC.
- Jekeli, C. (1998a) Error analysis of padding schemes for DFT's of convolutions and derivatives. **Report # 446 of the Department of Geodetic Science**. The Ohio State University, Columbus, Ohio.
- Jekeli, C. (1998b) Algorithms and preliminary experiences with the LN93 and LN100 for airborne vector gravimetry. **Report # 447 of the Department of Geodetic Science**. The Ohio State University, Columbus, Ohio.
- Jekeli, C. (2000) **Inertial Navigation Systems with geodetic applications**. New York: Walter De Gruyter.
- Jekeli, C. (2001) **Fourier geodesy**. Class notes for the GS875 course. Department of Civil and Environmental Engineering and Geodetic Science. Ohio State University, Columbus, Ohio, USA.

- Jekeli, C. (2003) Statistical analysis of moving-base gravimetry and gravity gradiometry. **Report No. 466, Lab for Space Geodesy and Remote Sensing**, Geodetic Science, OSU, Columbus, Ohio. (In preparation) complete by the end of September, 2003.
- Jekeli C. and Kwon J (1999) Results of airborne vector (3-D) gravimetry. **Geophysical Research letters**. Vol. 26, No. 23, pp. 3533-3536.
- Jekeli C. and Kwon J (2001) Geoid profile determination by direct integration of GPS/INS vector gravimetry. Submitted to **JGR-Solid Earth**.
- Jekeli, C. and Serpas J. (2003) Review and numerical assessment of the direct topographical reduction in geoid determination. **Journal of Geodesy**. Vol 77, 3-4, pp. 226-239.
- Koch, K-R. and Kusche, J. (2002) Regularization of geopotential determination from satellite data by variance components. **Journal of Geodesy**, 76:259-268.
- Kwon J. (2000). Airborne Vector Gravimetry using GPS/INS, Doctoral Dissertation, Dept. of Geodetic Science and Surveying, The Ohio State University, Columbus Ohio, USA.
- Kwon, J. and Jekeli C. (2001). A new approach for airborne vector gravimetry using GPS/INS. **Journal of Geodesy**. Vol 74, pp. 690-700.
- Lemoine, F.G., Kenyon, S.C., Factor, J.K., Trimmer, R.G., Pavlis, N. K., Chinn, D. S., Cox, C. M., Klosko, S. M., Luthcke, S. B., Torrence, M. H., Wang, Y. M., Williamson, R. G., Pavlis, E. C., Rapp, R. H., and Olson, T. R. (1998). **The development of the joint NASA GSFC and NIMA geopotential model EGM96**. NASA Goddard Space Flight Center, Greenbelt, Maryland, USA, July 1998.
- Moritz, H. (1968) On the use of the terrain correction in solving Molodensky's problem. **Report # 108, Department of Geodetic Science**. The Ohio State University, Columbus, Ohio.
- Moritz, H (1970) A generalized least-squares model. **Studia geoph. et geod.** 4,.353-362.
- Moritz, H. (1989) **Advanced Physical Geodesy**; Herbert Wichmann Verlag, Karlsruhe, Federal Republic of Germany.
- Novák, P., and Heck, B. (2002) Downward continuation and geoid determination based on band-limited airborne gravity data. **Journal of Geodesy**, 76, 269-278.

- Novák, P.; Kern, M.; Schwarz, K.-P.; Sideris, M.G.; Heck, B.; Ferguson, S.; Hammada, Y. (2003a) On geoid determination from airborne gravity. **Journal of Geodesy**, 76, 510-522
- Novák, P.; Kern M.; Schwarz, K.P.; Heck, B (2003b) Evaluation of band-limited. topographical effects in airborne gravimetry. **Journal of Geodesy**, 76, 597-604
- Pellinen, L. P. (1962) Accounting for topography in the calculation of quasi-geoidal heights and plumb-line deflections from gravity anomalies. **Bulletin Géodésique**, 63,57-65.
- Schaffrin, B. (1981) Best invariant variance component estimation and its application to the generalized multivariate adjustment of heterogeneous deformation observations. **Bulletin Géodésique**, 55,73-85.
- Schaffrin, B. (2001) Equivalent systems for various forms of kriging, including least squares collocation. **Zeitschrift für Vermessungswesen**, 126,87-94.
- Schaffrin, B. and Kwon, J. (2002) A Bayes filter in Friedland form for INS/GPS vector gravimetry. **Geophys. J. Int** , 149, 64-79.
- Schaffrin, B., Cai, J.Q., Grafarend, E. (2003) Minimum MSE adjustment and the optimal Tkhnov-Phillips regularization parameter. Part 1: α -weighted S-homBLE via repro-BIQUE. Submitted to the **Journal of Geodesy**.
- Schwarz K.P., Sideris M.G and Forsberg, R. (1990) The use of FFT techniques in physical geodesy. **Geophys. J. Int.**, 100, 485-514.
- Smith, D.A. and Roman, D. R. (2001) GEOID99 and G99SSS: 1-arc minute geoid models for the United States, **Journal of Geodesy** 75: 469-490.
- Vaniček, P. and Kleusberg (1987) The Canadian geoid – Stokesian approach. **Manuscripta geodaetica**, vol 12, 86-98.
- Vaniček, P. and Z. MartinecZ (1994): Stokes-Helmert scheme for the evaluation of a precise geoid. *Manuscripta Geodaetica*, 19, 119-128.
- Vaniček, P., W. Sun, P. Ong, Z. Martinec, P. Vajda, B. Horst (1996): Downward continuation of Helmert's gravity anomalies. **Journal of Geodesy**, 71, 21-34.
- Véronneau, M. (2001). The Canadian gravimetric geoid model of 2000 (CGG2000). http://www.geod.emr.ca/index_e/products_e/publications_e/papers_e/CGG2000a.pdf.

- von Frese, R.B., Hones, M.B., Kim, J.W., and Kim, JH (1997) Analysis of anomaly correlations. **Geophysics**, 62, No.1, pp.342-351.
- Wang, Y.M., (1988). Downward continuation of the free air gravity anomalies to the ellipsoid using gradient solution, Poisson's integral and terrain correction. Numerical comparison and the computations. **Report 393 of the Department of Geodetic Science and Surveying**, The Ohio State University. Columbus, Ohio.
- Wang Y. and Rapp R. (1990) Terrain effects on geoid undulation computation. **Manuscripta geodaetica**, vol 15, 23-29.
- Wichiencharoen, C (1982) The indirect effect on the computation of geoid undulations. . **Report # 336 of the Department of Geodetic Science**. The Ohio State University. Columbus, Ohio.